

GLIOMA GROWTH MODELING

Μοντελοποίηση Ανάπτυξης Γλοιοβλαστώματος

PhD Thesis | Διδακτορική Διατριβή

Alexandros E. Roniotis | Αλέξανδρος Ε. Ρονιώτης

TECHNICAL UNIVERSITY OF CRETE | ΠΟΛΥΤΕΧΝΕΙΟ ΚΡΗΤΗΣ

ELECTRONIC & COMPUTER ENGINEERING DEPT | ΤΜΗΜΑ ΗΛΕΚΤΡΟΝΙΚΩΝ ΜΗΧΑΝΙΚΩΝ & ΜΗΧΑΝΙΚΩΝ ΗΛΕΚΤΡΟΝΙΚΩΝ ΥΠΟΛΟΓΙΣΤΩΝ

Συμβουλευτική Επιτροπή | **Advisory Committee**

Καθ. Μιχάλης Ζερβάκης | Prof. Michalis Zervakis
Δρ. Κωνσταντίνος Μαριάς | Dr Kostas Marias
Δρ. Ευάγγελος Σακκαλής | Dr Vangelis Sakkalis

Εξεταστική Επιτροπή | **Examining Committee**

Καθ. Μιχάλης Ζερβάκης | Prof. Michalis Zervakis
Καθ. Αθανάσιος Λιάβας | Prof. Athanasios Liavas
Αναπλ. Καθ. Ευριπίδης Πετράκης | Assoc. Prof. Euripides Petrakis
Αναπλ. Καθ. Κωνσταντίνος Μπάλας | Assoc. Prof. Costas Balas
Επικ. Καθ. Αικατερίνη Μανιά | Assist. Prof. Katerina Mania
Δρ. Κωνσταντίνος Μαριάς | Dr. Kostas Marias
Δρ. Ευάγγελος Σακκαλής | Dr. Vangelis Sakkalis

Alexandros Roniotis

Computational Medicine Lab
Institute of Computer Science
Foundation for Research & Technology – Hellas (FORTH)
Nikolaou Plastira Street, 100
Vasilika Vouton, Heraklion, Crete, Greece
P.O Box 1385
GR-70013

tel: (+30) 2810 391 395

fax: (+30) 2810 391 428

email: alex@roniotis.gr

site: www.roniotis.gr

Chania, Crete
2013

Acknowledgments

Special thanks to Dr Kostas Marias and Dr Vangelis Sakkalis from Computational Medicine Laboratory, FORTH, without the support of who this thesis wouldn't be true.

Thanks to my colleagues in FORTH, namely Georgios Manikis, Ioannis Karatzanis, Eleftheria Tzamali, Georgios Tzedakis, Georgios Grekas, Giannis Zacharakis, Christina Farmaki, Georgios Tsibidis and Manolis Tsiknakis, for contributing to this work.

Thanks to Dr Georgios Stamatakos from in Silico Oncology Group, National Technical University of Athens, for guiding me during several stages of this work.

Thanks to my supervisor Prof Michalis Zervakis from the Electronic & Computer Engineering Dept, Technical University of Crete, for supporting me throughout these years.

Thanks to Dr Toersten Rohlfing for guiding me on the use of the SRI24 atlas.

Thanks to Prof Norbert Graf and his radiologists from the University Clinic in Saarland, Germany, for providing clinical data and helping with the delineation of tumors.

Abstract

4th-grade glioma (Glioblastoma multiforme) is the most aggressive type of brain cancer. Several mathematical models have been developed towards identifying the mechanism of tumor growth. In this thesis we try to figure out the main mathematic and implementation issues concerning a 3-dimensional (3D) model for appropriately simulating glioma growth in brain. A brief review on the models that have been proposed during the last decades for simulating glioma growth is initially provided. Afterwards a deep study is carried in the mathematical body of a 3D diffusive model, which exploits local tissue anisotropy and heterogeneity in brain with differentiated cancer cell proliferation schemes. Therefore, a virtual controllable case is presented for evaluating the accuracy, simulation time and storage & computational consistency of the various numerical schemes that have been implemented. Continuing, radiotherapy is introduced into the model and some first experimental results are presented. Concluding, we show a model for exploiting statistical tissue information and diffusion tensors extracted from atlases of healthy brain tissue. Lastly, after introducing the gross tumor volume, we present the proliferation – invasion – hypoxia – necrotic – angiogenesis (PIHNA) model and some *in vivo* experiments in mice.

Περίληψη

Το γλοίωμα 4ου βαθμού (πολύμορφο γλοιοβλάστωμα) είναι η πιο επιθετική μορφή εγκεφαλικού όγκου. Διάφορα μαθηματικά μοντέλα έχουν αναπτυχθεί προς τον εντοπισμό του μηχανισμού της ανάπτυξης του καρκίνου. Σε αυτή τη διατριβή προσπαθούμε να παρουσιάσουμε το μαθηματικό υπόβαθρο για ένα τρισδιάστατο μοντέλο που προσομοιώνει ικανοποιητικά την ανάπτυξη γλοιοβλαστώματος στον εγκέφαλο. Αφού κάνουμε μια ανασκόπηση των διαφόρων μοντέλων που έχουν προταθεί τις τελευταίες δεκαετίες για την ανάπτυξη του γλοιώματος, παραθέτουμε μια εις βάθος μελέτη των μαθηματικών στοιχείων ενός τρισδιάστατου μοντέλου διάχυσης, που εκμεταλλεύεται πληροφορία για την ανισοτροπική και ετερογενή διάχυση. Προς την κατεύθυνση αυτή, ένας εικονικός όγκος χρησιμοποιείται για την αξιολόγηση της ακρίβειας, του χρόνου εκτέλεσης και της υπολογιστικής πολυπλοκότητας που εμπεριέχουν διαφορετικές τεχνικές προσομοίωσης. Στη συνέχεια το μοντέλο προσαρμόζεται ώστε να μπορεί να προσομοιώσει ακτινοθεραπεία και παρουσιάζονται κάποια πειράματα σε αληθινά δεδομένα ασθενών. Στη συνέχεια παρουσιάζουμε ένα μοντέλο που εκμεταλλεύεται άτλαντες από υγιή εγκέφαλο προς τον εντοπισμό των περιοχών της φαιάς και της λευκής ουσίας (δεδομένα που χρειάζεται το μοντέλο). Τέλος, παρουσιάζεται το μοντέλο ΡΙΗΝΑ και κάποια αποτελέσματα in vivo πειραμάτων σε ποντίκια.

Contents

Thesis Outline	15
Thesis Contribution	17
Timetable.....	18
1. Introduction.....	19
1.1. Brain tumors.....	19
1.1.1. Tumor classification.....	20
1.1.2. Glioma	21
1.1.3. Glioblastoma multiforme	23
1.2. Medical imaging for identifying brain tumors.....	24
1.2.1. Radiography (X-ray).....	24
1.2.2. X-ray computed tomography (CT).....	25
1.2.3. Computed tomography angiography (CTA).....	26
1.2.4. Magnetic resonance imaging (MRI).....	26
1.2.4.1. T1-weighted MRI	26
1.2.4.2. T ₂ -weighted MRI.....	27
1.2.4.3. Fluid attenuated inversion recovery (FLAIR)	27
1.2.4.4. Diffusion Tensor Imaging (DTI).....	27
1.2.5. Magnetic resonance spectroscopy (MRS)	28
1.2.6. Perfusion weighted imaging (PWI).....	28
1.2.7. Positron emission tomography (PET)	29
1.2.8. Chest radiograph (CXR).....	29
1.3. Diagnosing glioblastoma multiforme	30
1.4. Mathematical Modeling of biological processes.....	31
2. Background.....	33
2.1. General Cancer Modeling.....	33
2.2. Glioma Modeling	33
2.3. The Diffusion – Reaction Equation model	34
<i>Net proliferation rates for untreated glioma</i>	35
<i>Estimation of parameters</i>	36
<i>Resection modeling</i>	37
<i>Low Grade Gliomas</i>	37
<i>Brain Tissue Heterogeneity</i>	37

	<i>Anisotropic Cell Migration</i>	39
	<i>Mass Deformation</i>	39
	<i>Chemotherapy Modeling</i>	39
3.	Mathematical analysis on glioma model.....	41
3.1.	Deriving the Equation with Fick's Law.....	41
3.2.	Numerical Solving.....	43
3.2.1.	The Forward Euler Method	43
	Deriving the Linear System.....	44
	The sparse matrix of the system	45
	Incorporating growth rate in the linear system	46
	The final linear system.....	48
3.2.2.	The Backward Euler Method	48
	Linear System Derivation.....	49
	The final linear system.....	49
3.2.3.	The θ -Methods	49
	Linear System Derivation.....	50
	The final linear system.....	50
	Choice of θ	50
3.2.4.	The Crank Nikolson Method	51
	Summary.....	51
4.	Implementation.....	53
4.1.	Grid Initialization	53
4.2.	Structures	54
4.4.	Solving the Linear system	59
4.4.1.	Forward Euler	59
4.4.2.	Backward Euler.....	60
4.4.3.	θ -methods	63
5.	Qualitative and Quantitative Analysis	65
5.1.	Pure diffusion modeling	65
5.2.	Testing and Simulation Description.....	66
5.3.	Analysis on Finite Differences	68
	Normalized mean absolute error	68
	Effect of grid resolution.....	69
	Effect of time step	72

5.4.	Comparison with Finite Elements	74
	Accuracy	75
	Simulation Time.....	76
	Storage and Computational Consistency	76
	Summary.....	77
6.	Application on real tumors.....	79
6.1.	Initial Patient Dataset	79
6.2.	Simulation Parameters	81
6.3.	Simulation Results	82
6.4.	Final Patient Dataset	83
6.5.	Cross validation	84
	Summary.....	85
7.	Merging model with brain atlases.....	87
7.1.	Methods	87
	7.1.1. Tissue heterogeneity and anisotropic diffusion model.....	88
	7.1.2. Using proportional local diffusion coefficients.....	89
	7.1.3. The SRI24 atlas.....	89
	7.1.4. The local diffusion weighting factor	91
7.2.	Data and Simulation	91
	7.2.1. Data Preprocessing	91
	7.2.2. Model Parameters.....	94
7.3.	Results	94
7.4.	Cross Validation.....	95
	Summary.....	96
8.	Radiotherapy	99
8.1.	Methods	99
	8.1.1. The Linear Quadratic model	99
	8.1.2. Clinical Datasets and Model Settings	100
	8.1.3. Radiotherapy Settings	100
8.2.	Results	102
	8.2.1. Cross validation	103
	Summary.....	104
9.	Introducing Gross Tumor Volume	105
9.1.	Methods	105

9.1.1.	Real Initial and Final Dataset	105
9.1.2.	Annotation of GTV1 and GTV2	107
9.1.3.	Simulation.....	107
9.2.	Results	108
9.3.	Cross validation	110
10.	Proliferation–Invasion–Hypoxia– Necrosis–Angiogenesis model	111
10.1.	Introducing the PIHNA model	111
10.2.	In vivo tumor growth.....	112
10.2.1.	Animal preparation.....	113
10.2.2.	Experimental Procedure.....	113
10.3.	Tomographic Imaging	114
10.4.	Results	114
10.4.1.	In vivo tumor growth.....	114
10.4.2.	In silico tumor growth	115
	Summary.....	116
	General Conclusions	119
	Publications	133

Thesis Outline

Up to now, the various implementations of Diffusive models, introduced in **chapter 1 and 2**, lack a firm mathematical background on the derivation of the system, with concrete assumptions on the approximation scheme.

The main objective of the **3rd and 4th chapters** is to provide the direct formalisms of the derived linear system and implementation hints, for the widely used Finite Difference schemes, namely forward Euler, backward Euler, Crank Nikolson and θ -methods for the mathematical solving of the anisotropic, heterogeneous and 3D diffusion-reaction equation simulating either the growth of glioma or other phenomena where diffusive models are applicable. These formalisms are designed for 3D, heterogeneous and anisotropic brain tissue and entail the general form of proliferation rate $f(c)$, so that one could use any net proliferation rate.

The **5th chapter** of this thesis stresses the limitations and advantages of each modeling scheme and provides quantitative proof. Hence, engineers and bioinformaticians working with glioma models (or any model with similar diffusion – reaction behavior) could assess the limitations of the model that they are about to develop, especially for real clinical models.

The **6th chapter** presents some initial results applied on real MRIs taken from patient with diagnosed GBM. By comparing the results of the simulation, with these of the real data, there seems to be a good agreement. Moreover, for evaluation we adopt a scheme that uses solid metrics and provides objective comparison (JC, DS, VS metrics).

The **7th chapter** presents an extended methodology for modeling GBM and predicting the progress of glioblastoma multiforme in space and in time. The diffusion – reaction equation was used for simulating the spatiotemporal change of tumor cell concentration, taking into consideration partial gray and white matter concentration in each voxel, extracted from the SRI24 open brain atlas.

Continuing, the **8th chapter** presents the application of the proportional model of chapter 7 for including radiotherapy. Despite the limited number of datasets, the evaluation results indicate that there might be a slight improvement in using the proposed model on glioblastoma multiforme. This is expected due to the several improvements introduced.

By using anisotropy only on the portions of white matter, instead of all type of tissue, we better approximate the glioma migration along white fibers. Moreover, radiotherapy is usually applied in fractions and the linear quadratic model has been adjusted to this, contrary to previous diffusive models which use the quadratic model for a single dose.

By incorporating the Gross Tumor Volumes in the model of **Chapter 9** we utilize the information hidden in the several modalities of MRI, namely T1-contrast, T1 and T2. The results of applying the model on real clinical datasets indicate that there is improvement in model prognostics.

The last Chapter (**Chapter 10**) extends the diffusive model to the PIHNA model, for accounting proliferation – invasion – hypoxia- necrosis and angiogenesis. We incorporate information provided by fluorescence molecular tomography data performed in-vivo into the PIHNA model. The outcome is validated against tumor evolution snapshots captured in vivo using advanced molecular probes in laboratory animals. The simulations are in line with in-vivo growth and the resected tumor morphology and suggest that space competition plays a dominant role in the evolution of the tumor under study.

Thesis Contribution

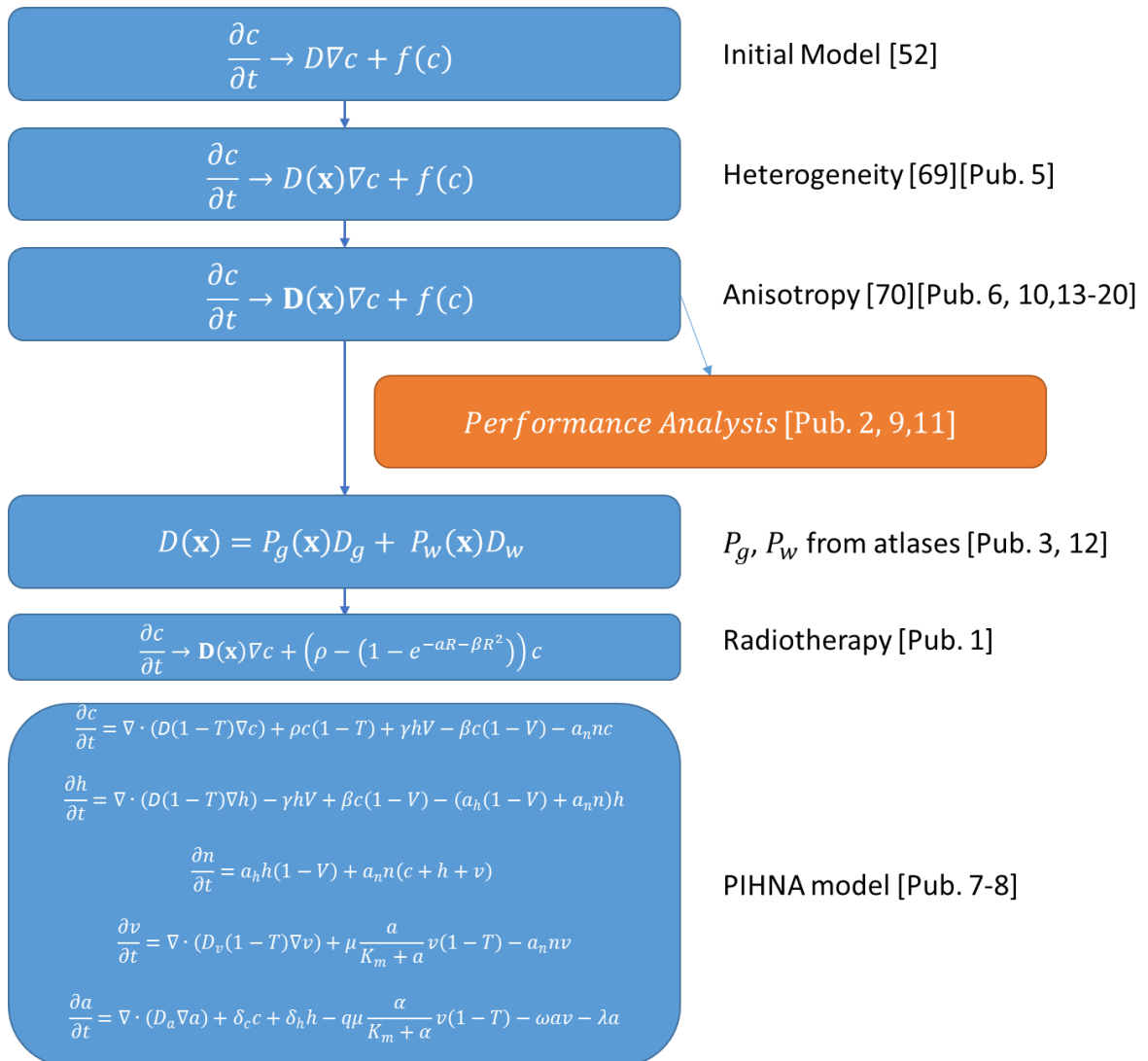
This thesis:

- Shares the mathematical formalism of the anisotropic, heterogeneous and 3-dimensional diffusion-reaction equation solution simulating glioma growth.
 - *Engineers and bioinformaticians who want to develop their diffusive model can use this as a manual.*
- Introduces the vectorization operator F for all three major cell proliferation rates (Gompertzian, Verhulst and Exponential).
 - *F can be used for switching from one proliferation rate to another.*
- Presents a detailed cross- performance analysis for the different numerical schemes used for model development in terms of accuracy, data imaging resolution, simulation time, storage and computational needs.
 - *One can assess the limitations of the model he/she is about to develop and which implementation meets his/her needs.*
- Introduces solid metrics for the evaluation of the modeling result (Jaccard, Dice and Volume Similarity).
 - *One can use the final brain imaging session of a patient as a ground truth for evaluating the results of modeling.*
- Introduces the use of continuous diffusion coefficients extracted from open-access normal brain atlases, instead of discrete values.
 - *The model fully exploits the information about the white and gray matter from atlases*
- Uses atlases for identifying the matter type underlying the tumor.
 - *The diffusion coefficients in the tumor region can be approximated.*
- Introduces non-zero diffusion coefficients for the Cerebrospinal fluid (CSF)
 - *The model simulates cancer diffusion in CSF for large cancers.*
- Uses Diffusion Tensor MRI from atlases for computing 3x3 diffusion tensors, i.e. can model anisotropic growth of tumor.
 - *The virtual tumor can grow anisotropically, as the migration of glioma cells is facilitated along white matter tracts.*
- Introduces the Linear Quadratic (LQ) model for simulating radiotherapy
 - *The model can simulate radiotherapy*
- Introduces a method for approximating the radiobiology parameters α and β (used in LQ), personalized for any patient.
 - *There is no need to have a-priori knowledge of the radiobiology parameters.*
- Introduces radiotherapy in multiple fractions.
 - *Radiotherapy is usually applied in multiple fractions, but existing models use one single dose.*
- Introduces the LQ model in the proliferation – invasion – hypoxia- necrosis and angiogenesis (PIHNA) model
 - *Radiotherapy can be modeled with PIHNA model.*

- Compares in-vivo experiments of the HeLa cancer cells in mice with in-silico experiments of the PIHNA model.
 - *In vivo experiments are held for first time for the PIHNA model.*

Timetable

As depicted in the graph below, my initial work was to extend the model proposed by Swanson et al. so as to include more terms and intrinsic details related to the cancer phenomenon. My first milestone was to develop the mathematical framework regarding the diffusion reaction equation for simulating glioma evolution and proliferation [Pub. 6, 10, 13-20] and then to make a performance analysis of the implemented model [Pub. 2,9,11]. Later an open access atlas was used to add heterogeneity and anisotropy to the model by using continuous diffusion coefficients for first time [Pub. 3, 12]. Continuing, radiotherapy was simulated by introducing the Linear Quadratic Model [Pub. 1]. Lastly, the cancer cell populations were differentiated by separating them to normoxic, hypoxic and necrotic cells, and by simulating vasculature and angiogenesis evolution [Pub. 7-8].



1. Introduction

Cancer, known medically as a malignant neoplasm, is a broad group of various diseases, all involving unregulated cell growth. In cancer, cells divide and grow uncontrollably, forming malignant tumors, and invade nearby parts of the body. The cancer may also spread to more distant parts of the body through the lymphatic system or bloodstream. Not all tumors are cancerous. Benign tumors do not grow uncontrollably, do not invade neighboring tissues, and do not spread throughout the body. There are over 200 different known cancers that afflict humans [1].

Determining what causes cancer is complex. Many things are known to increase the risk of cancer, including tobacco use, certain infections, radiation, lack of physical activity, obesity, and environmental pollutants [2]. These can directly damage genes or combine with existing genetic faults within cells to cause the disease [3]. Approximately five to ten percent of cancers are entirely hereditary.

Cancer can be detected in a number of ways, including the presence of certain signs and symptoms, screening tests, or medical imaging. Once a possible cancer is detected it is diagnosed by microscopic examination of a tissue sample. Cancer is usually treated with chemotherapy, radiation therapy and surgery. The chances of surviving the disease vary greatly by the type and location of the cancer and the extent of disease at the start of treatment. While cancer can affect people of all ages, and a few types of cancer are more common in children, the risk of developing cancer generally increases with age [4]. Figure 1 depicts an example of a lung cancer case [5].

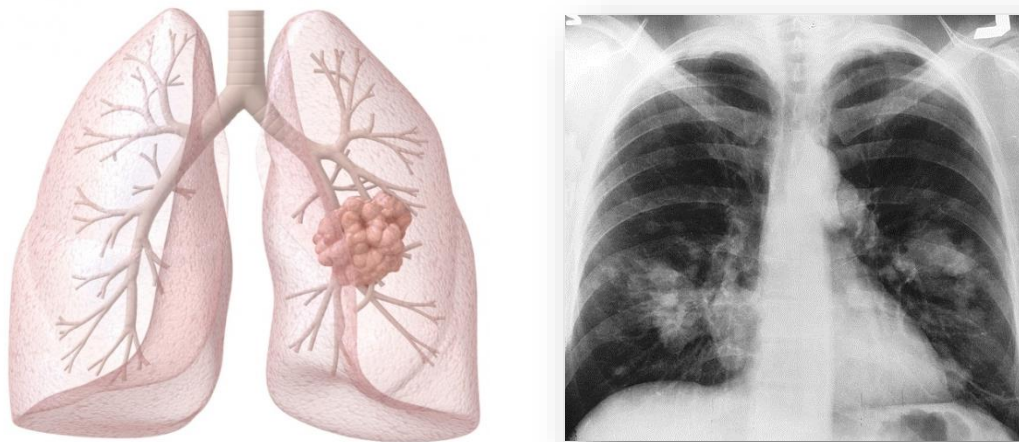


Figure 1 - Example of a lung tumor case. Left; A drawing of lung cancer; Right: a Magnetic Resonance Image of a lung cancer. The cancer is visible on the right-down part of the image [5].

1.1. Brain tumors

Cancer causes more than 13% of all deaths worldwide with an estimation of 12 million deaths in 2030 [6][7]. In United States, 2.5% of cancer deaths are caused by brain tumors [8]. A brain tumor, or tumor, is an intracranial solid neoplasm, a tumor (defined as an abnormal growth of cells) within the brain or the central spinal canal.

Brain tumors include all tumors inside the cranium or in the central spinal canal. Figure 3 presents a drawn representation of a brain tumor in cranium. Brain tumors are created by an abnormal and uncontrolled cell division, usually in the brain itself, but also in lymphatic tissue, in blood vessels, in the cranial nerves, in the brain envelopes (meninges), skull, pituitary gland, or pineal gland. Within the brain itself, the involved cells may be neurons or glial cells (which include astrocytes, oligodendrocytes, and ependymal cells). Brain tumors may also spread from cancers primarily located in other organs (metastatic tumors) [9]. An example of a metastatic tumor in brain from lung cancer is presented in Figure 2, shown on Magnetic Resonance Imaging (MRI), as the black arrow shows.

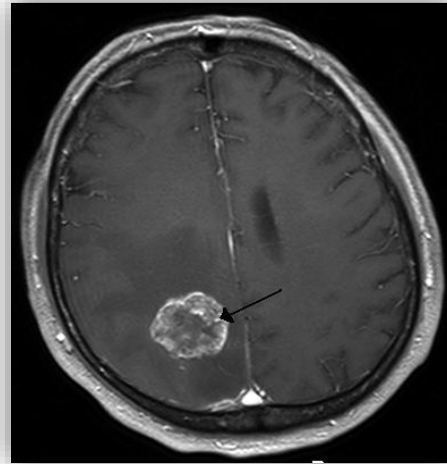


Figure 2 -Brain metastasis in the left cerebral hemisphere from lung cancer shown on T1-weighted magnetic resonance imaging with intravenous contrast

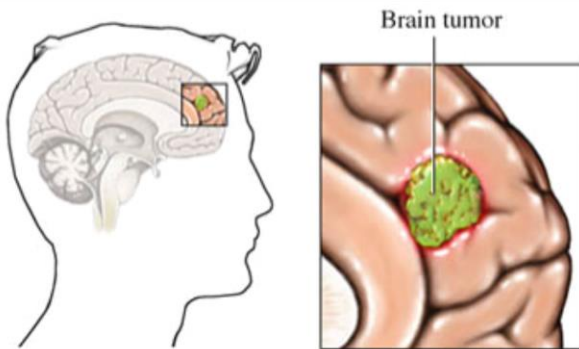


Figure 3 - Example of brain tumor representation

Any brain tumor is inherently serious and life-threatening because of its invasive and infiltrative character in the limited space of the intracranial cavity. However, brain tumors (even malignant ones) are not invariably fatal, especially lipomas which are inherently benign. Brain tumors or intracranial neoplasms can be cancerous (malignant) or non-

cancerous (benign); however, the definitions of malignant or benign neoplasms differs from those commonly used in other types of cancerous or non-cancerous neoplasms in the body. Its threat level depends on the combination of factors like the type of tumor, its location, its size and its state of development. Because the brain is well protected by the skull, the early detection of a brain tumor occurs only when diagnostic tools are directed at the intracranial cavity. Usually detection occurs in advanced stages when the presence of the tumor has caused unexplained symptoms.

1.1.1. Tumor classification

In order to comprehend the fundamental expanding behavior of tumor cells, it is essential to study the invasive behavior of cancer by classifying tumors, considering a broad ground ranging from benign, to pre-malignant or malignant tumors. To begin with benign tumors, cells appear essentially normal and are grouped like normal tissues. Moreover, benign tumors are localized, mostly encapsulated and do not invade adjacent tissue. On the opposite, malignant-tumor cells grow in an unlimited and aggressive manner. Additionally, not only the grouped cells do not resemble normal tissues, but also they are arranged in a

disorganized structure. In other words, these cells infest the adjacent tissue, resulting in its limited or complete tenancy. Thus, infection is either massive, causing tissue hardening and deformation, or tentacular, infiltrating cells into structures of the adjacent normal tissue. The latter one is more important for prognosis, since it is commonly associated with metastasizing.

Continuing, it is challenging to study how cell proliferation and tissue building determine the spatiotemporal development of tumor growth. It is noteworthy to mention that solid tumors are not only expanded by grouping of neoplastic cells, but also by normal tissues. More specifically, tumor growth takes place in pace with the growth of a cancer stroma, built from normal tissue. For this reason, normal tissue is actually determining the final tumor structure.

Thereupon, three levels of viewing tumor development are introduced [10]. To summarize these levels are: the sub-cellular level, the cellular level and the tissue level. At first, the subcellular level where normal cells acquire a cancerous phenotype, due to gene modifications. Secondly, the cellular level is connected to cell shape, movement, etc. and, lastly, the tissue level is connected to the structure of tumors. To make things clear, the point of view for each level is presented in Figure 4.



Figure 4 - The three different levels of studying tumour growth. (Left) The subcellular or gene level, (Center) the cellular level, studying cell properties and (Right) the tissue level, where the tissue morphology is studied.

1.1.2. Glioma

A glioma is a type of tumor that starts in the brain or spine. It is called a glioma because it arises from glial cells. The most common site of gliomas is the brain [11]. Gliomas make up ~40-50% of all brain and central nervous system tumors and 80% of all malignant brain tumors [12][13]. Gliomas are categorized by cell type, by grade and by location.

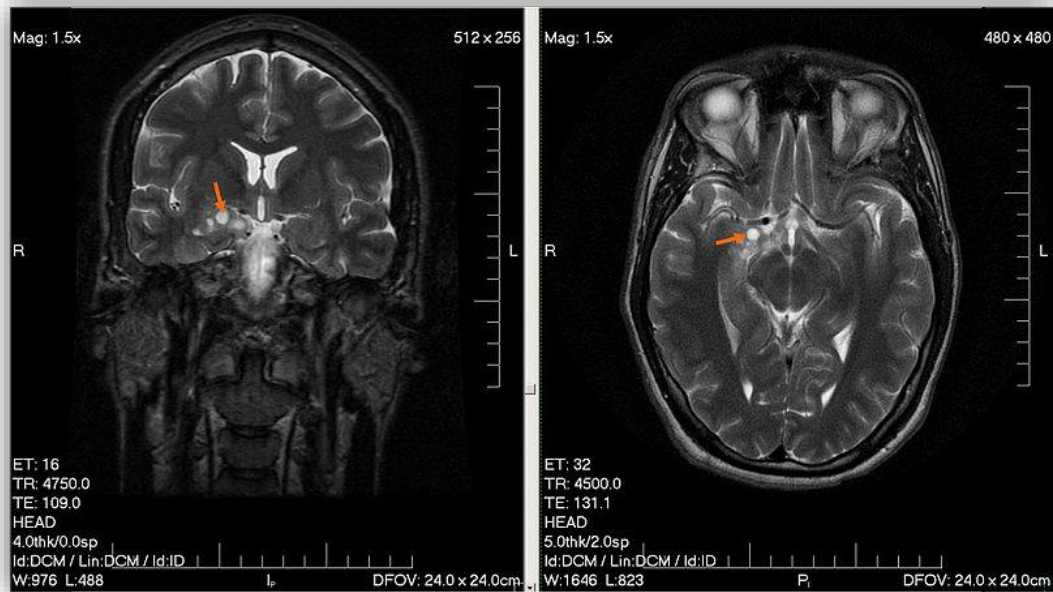


Figure 5 - Low grade glioma in a 28 year old male (July 2007)

Gliomas are classified according to the specific type of cell they share histological features with, but not necessarily originate from. The main types of gliomas are ependymomas (ependymal cells), astrocytomas (astrocytes), oligodendrogliomas (oligodendrocytes) and mixed gliomas (cells from different types of glia).

Gliomas are further categorized according to their grade, which is determined by pathologic evaluation of the tumor. Of numerous grading systems in use, the most common is the World Health Organization (WHO) grading system for astrocytoma, under which tumors are graded from I (least aggressive tumor) to IV (most aggressive tumor). Low-grade gliomas [WHO grade II] are well-differentiated, are not benign but still portend a better prognosis for the patient. On the other hand high-grade [WHO grade III-IV] gliomas are undifferentiated or anaplastic, are malignant and carry a worse prognosis for the patient. An example of a low grade brain encapsulated cyst-like glioma in a 28 year old male is presented in Figure 5 (rear view on left, top view on right) [14].

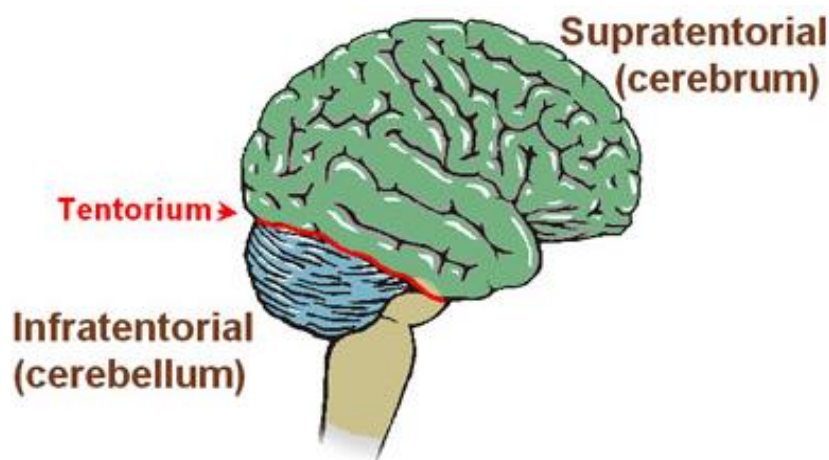


Figure 6 - Representation of Tentorium cerebelli, which determines the classification of supratentorial and infratentorial gliomas.

Lastly, gliomas can be classified according to whether they are above or below a membrane in the brain called the Tentorium cerebelli. The tentorium separates the cerebrum (above) from the cerebellum (below), as Figure 7 depicts. Supratentorial gliomas are located above the tentorium, in the cerebrum and are mostly found in adults (70%). Infratentorial gliomas are found below the tentorium, in the cerebellum, and are mostly found in children (70%). Pontine gliomas are located in the pons of the brainstem.

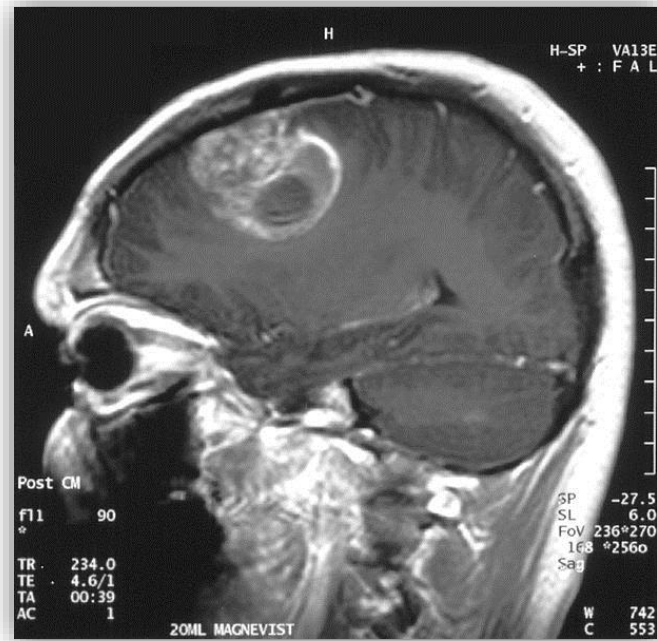


Figure 7 - Glioblastoma of a 15 year old boy shown on MRI sagittal view.

Out of these, classification according to grade is the most commonly used. High-grade gliomas are highly-vascular tumors and have a tendency to infiltrate. They have extensive areas of necrosis and hypoxia. Often tumor growth causes a breakdown of the blood-brain barrier in the vicinity of the tumor. As a rule, high-grade gliomas almost always grow back even after complete surgical excision. On the other hand, low-grade gliomas grow slowly, often over many years, and can be followed without treatment unless they grow and cause symptoms.

1.1.3. Glioblastoma multiforme

WHO grade IV astrocytoma, namely glioblastoma multiforme (GBM) accounts for 23.1% of brain tumors [13][15][16]. Despite extensive research on GBM during the last decades, mortality hasn't changed significantly over the last years, with average life expectancy ranging at 12-14 months after diagnosis and only 4% of treated patients being alive after 5 years [17][18][19][20][21]. Death is usually due to cerebral edema or increased intracranial pressure [22]. Figure 7 presents a sagittal MRI slice of GBM in a 15 year old boy [23].

Unfortunately, the causes of GBM are still undefined. It has been observed that GBM occurs more commonly in males, in aged people and to patients of low-grade astrocytoma that develop into a higher degree [24]. Alcohol consumption may also be a possible risk factor [25]. Moreover, GBM has been associated with the viruses SV40 [26], cytomegalovirus [27] and lead [28].

The diagnosis of GBM can be done by clinical imaging techniques, with MRI being the most common technique. When viewed with traditional imaging techniques, GBM often appears as ring-enhancing lesions with non-specific boundaries: due to very high cell invasiveness,

unlike solid tumors, GBM does not form a solid and compact mass with cells dispersed around the lesion [29]. Figure 8 presents a representation of typical massif cancers (left) which appear as a bulk tumor with MRI and two types of GBM (center and right), where there are many individual cells dispersed around the lesion [30]. Therefore, this work studies how GBM boundaries can be predicted using a mathematical model.



Figure 8 - Structural types of cancers. Left: solid tumor tissue only; Center: tumor tissue and peripheral isolated tumor cells; Right: isolated tumor cells only. A typical GBM follows one of the two last types [30].

1.2. Medical imaging for identifying brain tumors

Medical imaging is the technique and process used to create images of the human body in order either to reveal, diagnose, or examine disease or to study normal anatomy and physiology. Brain tumor therapy is highly dependent on diagnosis, which must be as close as possible at the early stages of disease. Since the asymptomatic period can last for a long period (months or ages), this is crucial to diagnose the disease before local expansion or metastatic invasion. Every indication should motivate every person to ask medical assistance, since the recognition of a symptom (e.g. persistent headaches, cough, swelling or hardening of the breast) may be the first step for early diagnosis of malignant neoplasia. Diagnosis is critical for identifying the type and the characteristics of a tumor. Misdiagnosis can often lead to an erroneous prognosis and treatment.

Current diagnostic techniques provide the option to observe morphology, size and stage of the tumor and to indicate the proper treatment. The latest diagnostic approaches depend principally on non-surgical imaging techniques which use X-rays, powerful magnets or radioactive materials for producing images of the tumorous brain areas. These images are then processed, studied and analyzed by radiologists, expertise in diagnostic imaging techniques [31][32]. The latest commonly used imaging techniques are listed below.

1.2.1. Radiography (X-ray)

Skull radiograph (X-rays) was a standard diagnostic tool in the past, but today it is used only when advanced techniques, such as magnetic resonance imaging, are not



Figure 9 - First radiography by Wilhelm Röntgen of his wife Anna Bertha Ludwig's hand

available. Occasionally it may be useful to indicate calcification usually observed slow-growing brain tumors. Astrocytoma is the most common calcified tumor, while 50-60% of oligodendroglioma, 70-80% of craniopharyngioma, 50% of ependymomas, 35% of ganglioglioma and 10% of meningiomas appear calcified. Figure 9 presents the first X-ray in history, taken by the inventor of X-rays (Wilhem Röntgen) on his wife's hand [33].

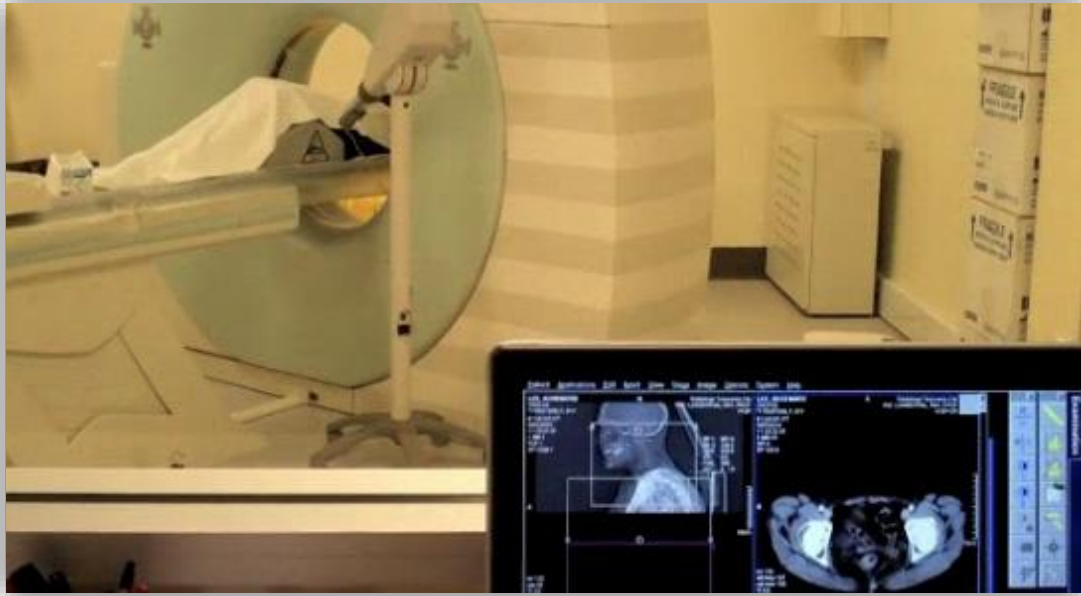


Figure 10 - A patient is receiving a CT scan for cancer treatment planning. Outside the scanning room are the imaging computers that compile 2D axial slices of the patient which can give the physician a 3D understanding of the anatomy [34].

1.2.2. X-ray computed tomography (CT)

The X-ray Computed Tomography (CT) is an X-ray examination which produces detailed cross-sectional images of the brain tissue. Instead of taking one picture, like in radiography, CT scanner produces several scans of brain tissue as it rotates around the patient's head. A computer then synthesizes these images and produces a sequential sequence of slices depicting the brain tissue. Unlike radiography, a CT scan has the potential to create detailed images of soft body tissue, such as brain tissue. CT scans tend to be better tolerated than MRI, due to short scan time, and is more sensitive to detecting acute hemorrhage, calcifications and osseous involvement. An example of CT scanner in action is presented in Figure 10 [34].

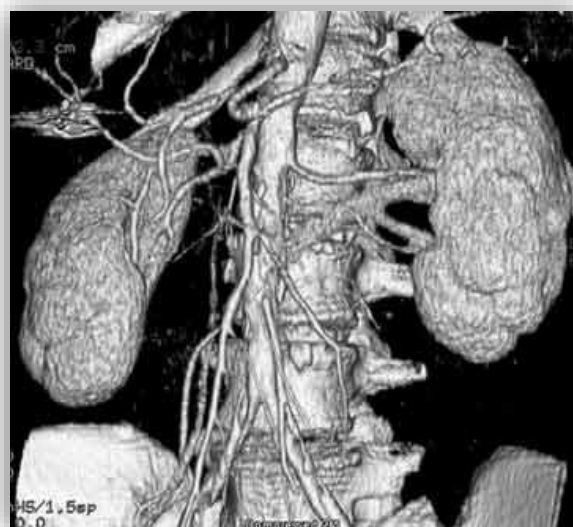


Figure 11- CT Angiography of abdominal aorta and arteries to the kidneys and intestines [35].

1.2.3. Computed tomography angiography (CTA)

Computed tomography angiography (CTA) is a computed tomography technique used to visualize arterial and venous vessels throughout the body. During this examination a contrast agent is injected intravenously into the patient. Then, the CTA scanner produces detailed images of blood vessels in the brain, which may help clinicians to plan surgery. Figure 11 presents as an example of a CTA of abdominal aorta and surrounding arteries [35].

1.2.4. Magnetic resonance imaging (MRI)

Magnetic Resonance Imaging (MRI) is particularly useful for examining brain and spinal cord, considered the best technique to detect tumors in these locations. Therefore MRI is used for the studies of this work. The MRI images are usually more precise than those obtained by CT. One major drawback however is that MRI, as shown in Figure 12 [36] does not show the bones of the skull, like CT scans, making it difficult for the radiologist to discern the effects of tumors in skull. The MRI scans use radio waves and strong magnets instead of X-rays. The energy from the radio waves is absorbed and then released in a pattern linked to the tissue and certain diseases. Special computer software translates the pattern into a very detailed image which can be represented in 3 dimensions. In most cases the patient receives a contrast agent, called gadolinium (Gd), by intravenous injection prior to scanning in order to obtain clearer images [37]. Similarly to CTA, there is MR Angiography (MRA) [38] which usually produces lower details in blood vessels than CTA. Lastly, some different modalities of MRI used in this work are reviewed separately in later paragraphs.



Figure 12 - Example of a MRI taken on a normal brain. The skull is not very well indicated, but soft matter is [36].

1.2.4.1. T₁-weighted MRI

T₁ weighted MRI refer to a set of standard scans that depict differences in the spin lattice relaxation time (known as T₁) of various tissues within the brain. T₁ weighted images can be acquired using either spin-echo or gradient-echo sequences. T₁ weighted contrast can be increased with the application of an inversion recovery radiofrequency pulse. Gradient-echo based T₁-weighted sequences can be acquired very rapidly because of their ability to use short inter-pulse repetition times. T₁-weighted sequences are often collected before and after infusion of T₁-shortening MRI contrast agents [39]. In the brain T₁-weighted scans provide appreciable contrast between gray and white matter, which is very important in our work. The right part of Figure 13 depicts an example of a T₁ weighted MRI slice.

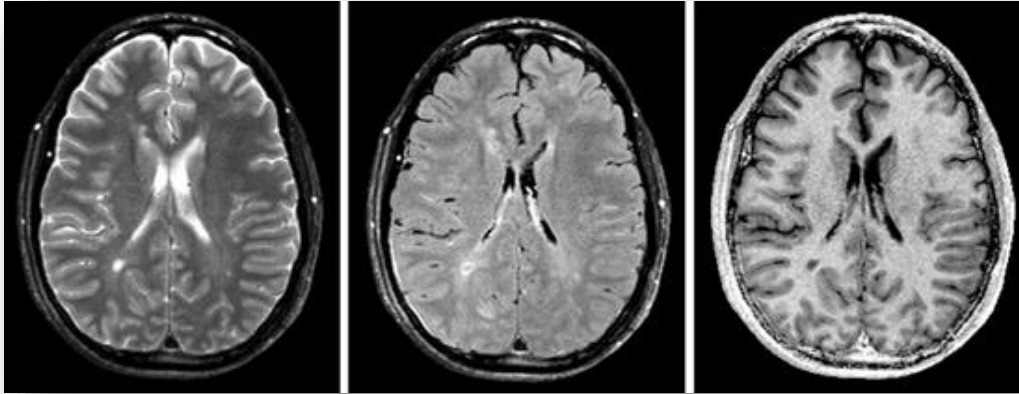


Figure 13- Different MRI modalities on the same patient; left: T_2 weighted MRI; center: FLAIR; right: T_2 weighted MRI [40].

1.2.4.2. T_2 -weighted MRI

T_2 weighted MRI is another basic type of MRI [41]. Like the T_1 weighted MRI, fat is differentiated from water, but in this case fat shows darker and water lighter. For example, in the case of cerebral and spinal study, the cerebrospinal fluid (CSF) will be lighter in T_2 weighted images. These scans are therefore particularly well suited to imaging edema with long echo time and repetition time. Because the spin echo sequence is less susceptible to inhomogeneities in the magnetic field, they are widely used in clinical praxis. The left part of Figure 13 depicts an example of a T_2 weighted MRI slice.

1.2.4.3. Fluid attenuated inversion recovery (FLAIR)

Fluid Attenuated Inversion Recovery (FLAIR) is an inversion-recovery pulse sequence used to null signal from fluids. It can be used in brain imaging to suppress cerebrospinal fluid (CSF) so as to bring out the periventricular hyperintense lesions, such as multiple sclerosis plaques. By carefully choosing the inversion time (the time between the inversion and excitation pulses), the signal from any particular tissue can be suppressed [42]. The central part of Figure 13 depicts an example of a FLAIR slice.

1.2.4.4. Diffusion Tensor Imaging (DTI)

Diffusion tensor imaging (DTI) is an application of Diffusion MRI (DMRI). DMRI measures the diffusion of water molecules in biological tissues [43]. DTI enables diffusion to be measured in multiple directions and the fractional anisotropy in each direction to be calculated for each voxel [44]. This enables researchers to make brain maps of fiber directions to examine the connectivity of different regions in the brain (using tractography). Indeed, DTI has been used in some experiments of this work for tracking the direction of white matter fibers in brain. Figure 14 presents the reconstruction of tracts in brain, projected on one MRI slice. The information used for this representation has been extracted from DTI data.

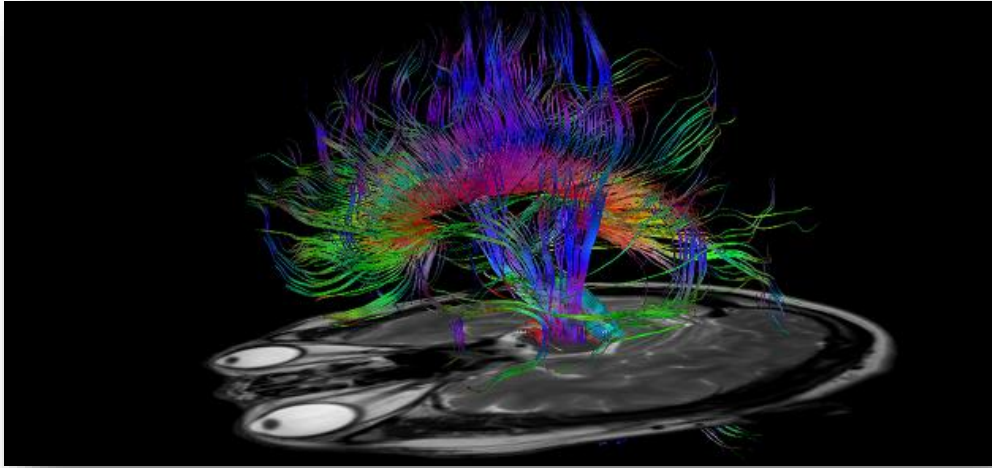


Figure 14 - Reconstruction of brain tracts by using DTI data, projected on a MRI slice [45].

1.2.5. Magnetic resonance spectroscopy (MRS)

Magnetic Resonance Spectroscopy (MRS) or commonly mentioned as Nuclear Magnetic Resonance Spectroscopy (NMR), is similar to MRI, except that it enables the measurement of the interactions of radio waves with different atoms, such as hydrogen. The MRS images highlight some substances of brain tumors, called metabolites (such as choline, NAA, lactate), which are not clearly visible in MRI. The study of these metabolic substances in brain tumors provides the metabolic profile of the tumor, called metabolism, which is a powerful tool for helping the clinicians decide which treatment plans to provide. MRS can also be used after treatment in order to identify an abnormal range, i.e. if this area is a remaining tumor or it is more likely to be injured normal tissue [46]. An example of an MRS image of brain is presented in Figure 15a, with spectra of metabolites (b, c) and a metabolite map (d).

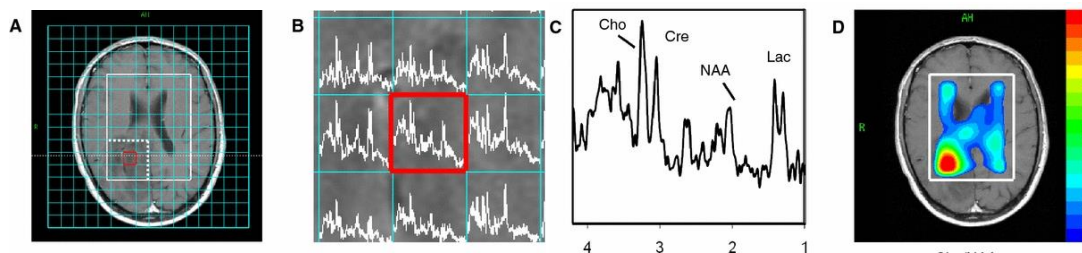


Figure 15 - Magnetic resonance spectroscopic imaging (MRS) data obtained from a patient with low-grade oligodendroglioma; a. MR image with volume of interest selected in white and two-dimensional MRS grid in blue. Spectra are only acquired from the MRS voxels inside the volume of interest. The dotted line in a indicates the MRS voxels shown in b; b. Part of the spectral image showing MRS voxels with their corresponding spectra; c. Enlargement of the spectrum obtained from the voxel indicated in red in b and c. The spectrum shows a typical pattern for a low-grade brain tumor with increased choline, decreased NAA, and the doublet of lactate; d. Metabolite map showing the intensity distribution of the ratio of choline to NAA over the volume of interest with the highest intensity indicated in red at the position of the tumor [46].

1.2.6. Perfusion weighted imaging (PWI)

Magnetic resonance perfusion or Perfusion Weighted Imaging (PWI) is another important imaging examination that uses an injected contrast agent (gadolinium) in order to discern

blood flow through brain tissues. This technique is based on the observation that brain tumors require more blood supply than normal brain areas. This means that the faster a tumor grows the more blood it requires. Therefore, PWI can provide clinicians with an insight into how fast a tumor is growing or help them by indicating the best position for biopsy resection [47].

1.2.7. Positron emission tomography (PET)

Positron emission tomography (PET) is a special examination based on the property of brain tumors to absorb greater amounts of glucose with respect to the healthy tissue. Therefore, glucose injected with a radioactive atom is administered through injection into the patient's blood. Afterwards, a special camera can generate an image of areas with high radioactivity inside the body. This image is not as detailed as a CT or MRI, but it can provide useful information on whether the abnormal areas that have been portrayed in other exams (such as MRIs) are either cancerous or non-cancerous. PET is also useful after treatment, as it can provide information for necrotic tumor cells, since dead cells do not consume glucose. It is very common to see abnormal areas on MRI, after treatment: PET scans can help the clinicians determine whether the abnormal region is an unresected tumor or possibly injured tissue [48]. Figure 16 presents a PET scan on a 56 year old male taken with PET. Red areas show more accumulated tracer substance (called 18F-FDG) and blue areas are regions where low to no tracer have been accumulated [49].

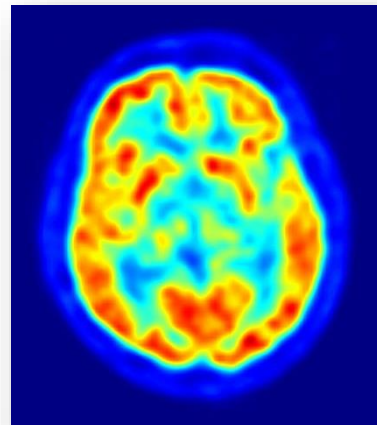


Figure 16 - PET scan of the human brain. Red areas show more accumulated tracer substance (18F-FDG) and blue areas are regions where low to no tracer have been accumulated.

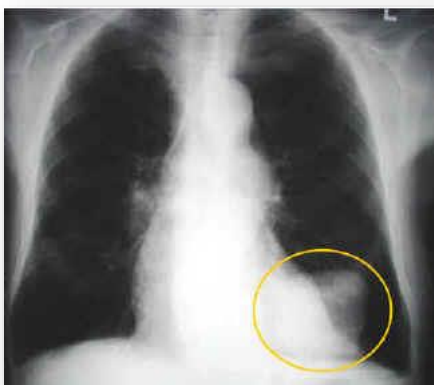


Figure 17 - Chest X-ray that shows a white area (yellow circle) that represents a solid area in the lung. This is a lung cancer [43].

1.2.8. Chest radiograph (CXR)

A chest radiograph, commonly called a chest X-ray (CXR), is a radiograph of the chest used to diagnose conditions affecting the chest, its contents, and nearby structures. The purpose of this examination is to identify potential tumors in other organs of the body that have metastasized to the brain. Such an organ could be the lung, which in most cases gives brain metastases. Figure 17 presents an example of chest radiograph that shows a white area delineated with a yellow line. This represents a solid area in the lung, being a lung cancer [50].

1.3. Diagnosing glioblastoma multiforme

The most common problem with diagnosis and treatment of GBMs is that they are characterized by very high motility and invasiveness. They exhibit highly diffusive behavior, meaning that cells are diffused within a large area. As you can see in the schematic example of Figure 18, there are GBM cells that are diffused within the brain space. Thus, this means that there are cells beyond this area that cannot be visualized by the commonly imaging techniques, as the example of Figure 18 (right) shows.

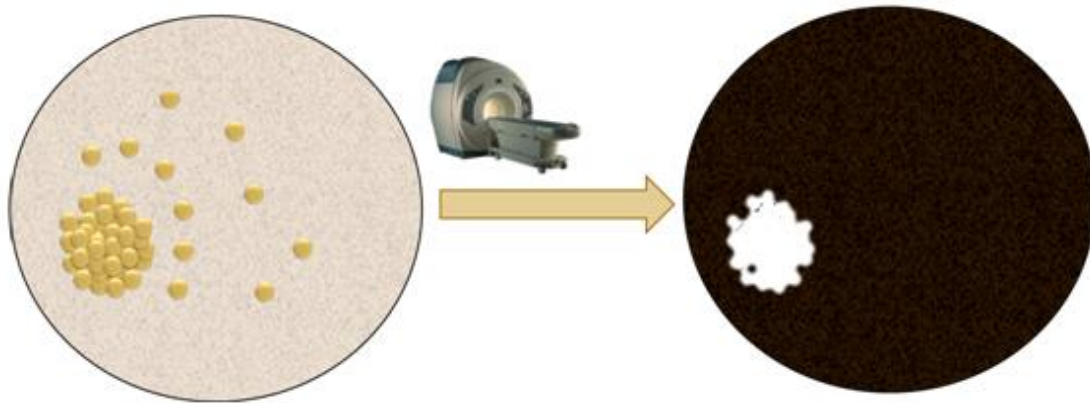


Figure 18- left: The cells of GBM do not constitute a bulk tumor. Oppositely, there are dispersed cells inside brain; Right: MRI cannot visualize all GBM cells, but only areas of high GBM cell density.

This can be more clearly understood by studying treatment results in glioblastoma: Even if the clinician treats 2cm beyond the imaged bulk tumor, GBM is very possible to recur due to dispersed cells. As a schematic example, consider the case of Figure 19: Let the clinician take the MRI scan into account and allow some safety margin during treatment, as in Figure 19 (left). As seen in Figure 19 (center), it is very possible to leave GBM cells back. These untreated cells may recur and cause death, as shown in Figure 19 (right).

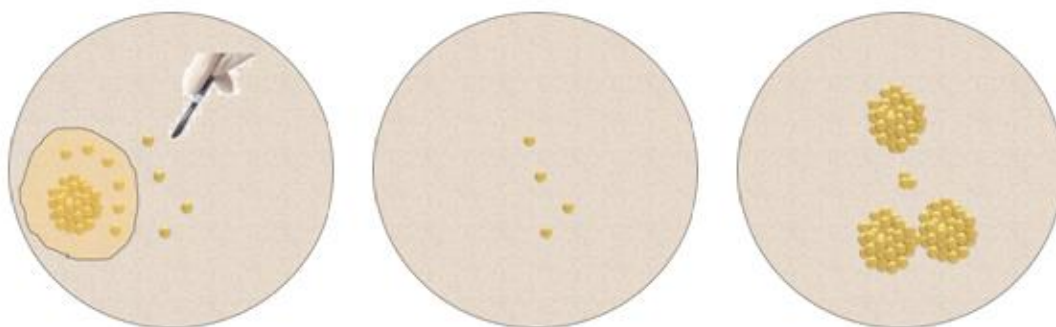


Figure 19 - left: The clinician defines a safety margin around the MRI scanned area; center: After treatment, there are GBM cells left; right: GBM recurs

1.4. Mathematical Modeling of biological processes

A mathematical model uses mathematical language to describe a system. In this work, we try to address a mathematical description for GBM growth. At first we have to bear in mind the basic features that any typical mathematical model in biology must possess [51]. These are schematically described in Figure 20. Firstly, the model should be initiated within a realistic biological state. Additionally, the modeled biological processes should be understood and discretized as much as possible, meaning that steps and real biological parameters should be isolated. Continuing, it is essential to allocate a mechanism that could simulate these steps and incorporates these parameters. Specifically, this mechanism could be described by a mathematical set of equations, like in our case. Going further, the next step is to study the model mathematically and come up with solutions that include realistic boundary and initial conditions. Lastly, after having acquired the theoretical results it is of great importance to go back in biological process with predictions, comments and suggestions for experiments that will either ascertain or disprove the developed model. At this level, model success is highly dependent on combining

experimentation and theory together. Because, even if the experimental results indicate that the model is incorrect, this is the right way to reach a successful conclusion. In final consideration, mathematics is very important in biology, however this must be treated with seriousness. If mathematics is used for solving any biological process, without thoroughly studying the biological background, it is very possible to come up with solutions that not only do not contribute to corroborated conclusions, but also do harm. The theoretical literature abounds with many such articles [51].

Modeling the glioma case

A lot of research is currently taking place on the mathematical modeling of the glioma growth procedure, especially glioblastoma multiforme. An efficient mathematical model for gliomas could help researchers and clinicians to get a better understanding of tumor growth pathology, to predict the aggressiveness of a patient's tumor and to better define the margins of a tumor, so as to use them when applying resection, chemotherapy or

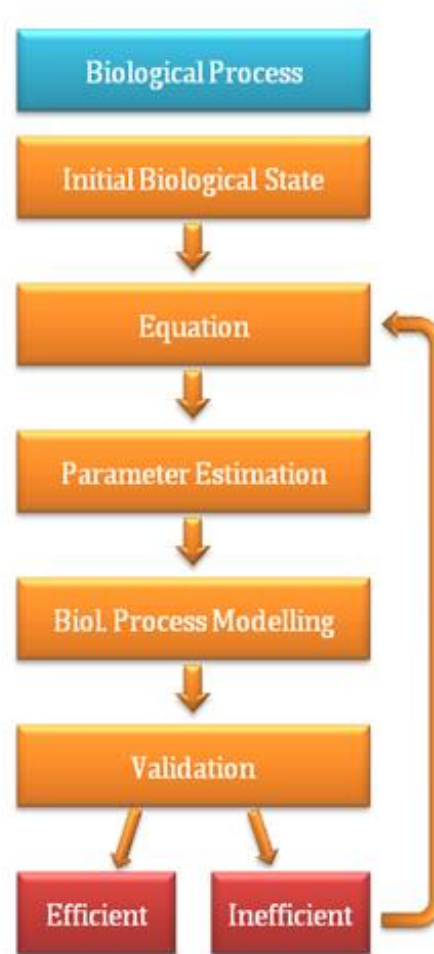


Figure 20 - Mathematical modeling for a general biological process.

radiotherapy. Moreover, by importing therapy parameters into the model, the clinician can predict which therapy scheme is expected to yield better results for the patient.

2. Background

In silico modeling is a modern application of computers for simulating biological processes. Especially, during the last decades, *in silico* modeling has been spread to all biology fields. Apart from mathematical modeling of human anatomy (e.g. heart modeling), pathological modeling has been widely studied in research institutes globally. Before studying the specific case of GBM, it is required to get a deeper insight into the general pathology models for tumor growth.

2.1. General Cancer Modeling

Studying tumor expansion and simulating this according to mathematical models, has been

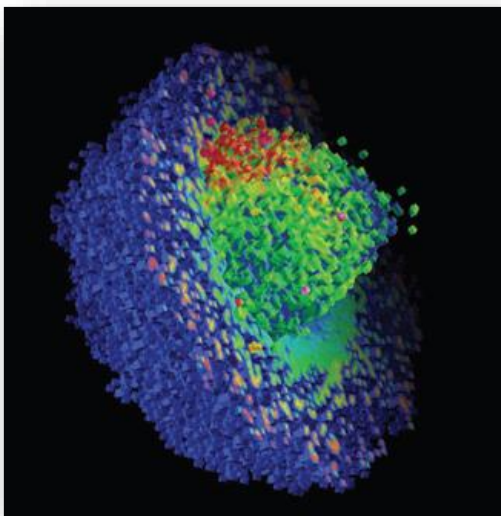


Figure 21 - Virtual Tumor. A simulation of one half of the whole living tumor cell population (outer half sphere) and the complete necrotic (dead) tumor cell population (inner sphere). Coloration relates to cell-adhesion value—cells on the outer surface of the tumor all have zero cell to cell adhesion [56].

an area of studies in cancer since late 90s' [52][53][54][55]. Tumor growth has been studied by a series of models. The first models focused on tumor behavior in time. More specifically, the first proposed temporal models were based on either exponential, logistic or Gompertz laws [56] (Figure 21). As expected, these models were followed by spatial growth models in later years. Thus, one such deterministic model has been used to simulate cancer growth as a wave phenomenon, taking into account mitosis and nutrient depletion [55]. Moreover, deterministic models taking into account immune response [57] or mitotic rates changes [58] have been proposed.

2.2. Glioma Modeling

Unfortunately, the detection rates of the exact boundaries of GBM with common imaging techniques, such as magnetic resonance imaging (MRI), X-ray computed tomography (CT) and positron emission tomography (PET) are still poor [59][60][61]. Unlike solid tumors, for which simple exponential or geometric expansion could represent expansion of tumor volume, the GBM growth rate cannot be determined as the classical doubling rate [62], because GBM does not form a solid and compact mass with cells invading the surrounding lesion.

Clearly, new mathematical formulations were necessary for studying this specific glioma case. Since early 90s, there has been a vast amount of research towards simulating and formulating the mechanisms of GBM development, both in macroscopic and microscopic levels. Microscopic models [63][64][65][66][67] study the intracellular biological interactions in cell level.

Mathematical modeling of glioma at the macroscopic level has represented the traditional framework in predicting glioma diffusion. Macroscopic models [68][52][69][70][71][72][73][74] study the tumor behavior, velocity and mass deformation with using anatomical information derived from medical images. Kansal et al. [75] viewed the tumor as a Gompertzian population of cells and its growth as a dynamic process where proliferating and inactive classes of cells interact, without taking invasion into neighboring tissues into account. Moreover, Zizzari's volumetric model [76] describes the proliferation of GBMs using tensor product splines and differential equations, the solutions of which give the spatiotemporal distribution of tumor cells. Finally, Tabatabai et al. [77] simulate real tumor asymmetric growth by accommodating the concept of increasing versus decreasing tumor radii, without incorporating the interactions between healthy and cancer cells at the tumor border and the competition of cells inside the tumor. However, even if these macroscopic models used growth and proliferation parameters, they don't produce realistic clinical cancer growth representation as they lack taking invasion of tumor cells into account.

2.3. The Diffusion – Reaction Equation model

The trend in glioma research is to study biological and clinical factors involved in cancer diffusion through healthy tissue. Unlike solid tumors, for which simple exponential or geometric expansion represents expansion of tumor volume, the glioma growth rate cannot be determined as the classical doubling rate [10], because gliomas can migrate and proliferate.

The class of macroscopic models that has been widely used for simulating this diffusive behavior is diffusive modeling [53]. Diffusive models simulate the change of glioma cell concentration in time and in space, by using two main terms of the Diffusion – Reaction Equation. The first that proposed a diffusive model for glioma growth was Murray in 1989 [78]. Murray proposed the diffusion-reaction formalism as:

$$\frac{\partial c}{\partial t} \rightarrow -div(\underline{J}) + \underbrace{S(c) - T(c)}_{f(c)} \quad 1$$

where

- $c(\mathbf{x}, t)$ denotes the tumor cell concentration at position \mathbf{x} at time t
- \underline{J} is the diffusion flux of cell that follows Flick's law; $\underline{J} = -D\nabla c$ where ∇ and div are the gradient and divergence operators respectively. This term expresses the diffusive behavior of tumor cells and the way they are dispersed in brain
- $S(c)$ denotes the source factor, representing the GBM cell proliferation
- $T(c)$ denotes the treatment, representing the GBM cell loss due to treatment. This is zero, when no treatment is applied.
- The initial state of the model, $c(x, 0)$, is defined as the initial distribution of the cancerous cells.
- The term $f(c) = S(c) - T(c)$ denotes the net proliferation rate.

This equation is the “ancestor” of most important works for glioma modeling. The general procedure for glioma modeling, as derived by Murray’s diffusive model, is presented in Figure 22. The initial concentration of tumor cells is estimated by using medical imaging techniques, like MRI, and tumor boundaries are delineated by a clinician. Afterwards the DRE model is applied on this initial state after the estimation of parameters of diffusion (diffusion coefficient) and invasion (cell proliferation rate and cell dead rate). Continuing, a validation algorithm is used to score the results and indicate whether the model should be reapplied with different parameters or not.

The solution of the diffusion-reaction equation requires the application of numerical schemes, since there is no direct formula of its solution. The solution has to be approximated iteratively till time point of interest is reached.

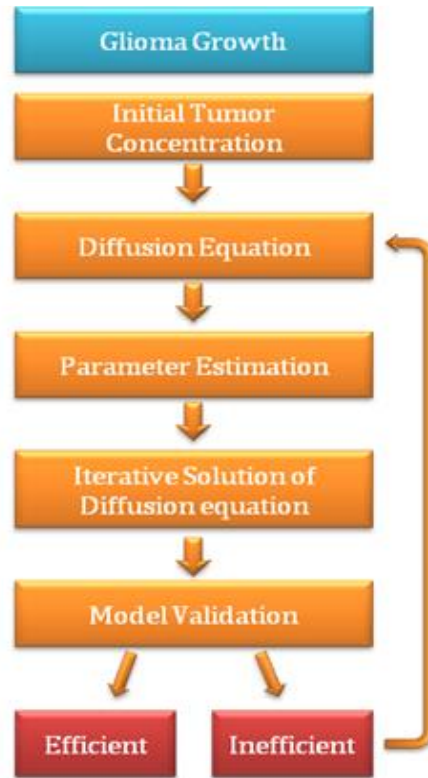


Figure 22 - Generalized mathematical modeling of glioma growth

Net proliferation rates for untreated glioma

In 1995 Tracqui [52] used the formulation of Equation 1 for simulating evolution of cell concentration by using two characteristic of tumor growth: proliferation and invasion. Tracqui proposed that the cells proliferate at exponential rate ρ , that is:

$$f(c) = \rho c \tag{2}$$

Thus, Tracqui specified Equation 2 as:

$$\frac{\partial c}{\partial t} \rightarrow \nabla \cdot (D\nabla c) + \rho c \tag{3}$$

where ρ denotes the proliferation rate of cells. Other proposed models [79], instead of geometrical rate, used either Verhulst law

$$f(c) = \rho c \frac{c_m - c}{c_m} \tag{4}$$

or Gompertz law

$$f(c) = \rho c \ln \frac{c_m}{c} \tag{5}$$

where c_m is the maximum value that concentration can reach (cell-space saturation). Equation 2 has been mainly used for simulating untreated gliomas, since no death term is included.

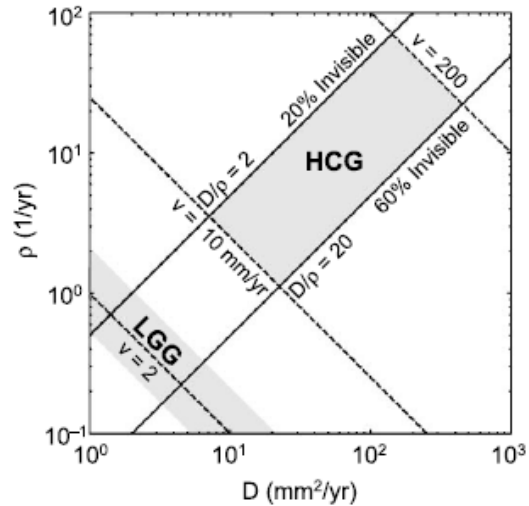
Estimation of parameters

From the very beginning of diffusive models, one of the key issues was the estimation of parameters that are being used. The diffusion coefficient D and the proliferation rate ρ are the basic parameters for the diffusive models. The first estimation of them took place in 1991, when Silbergeld [21] studied biological data and introduced two groups of glioma cells: the common ones and the resistant-to-first-chemotherapy ones. Parameter D was firstly defined either at $D = 10^{-2} \text{ cm}^2/\text{day}$, with the percentage of cells resistant to chemotherapy being at 8%, or at $D = 10^{-3} \text{ cm}^2/\text{day}$ without resistant cells, while ρ was defined at $\rho = 10^{-2}/\text{day}$.

Modern models use guiding indexes for defining parameters D and ρ according to glioma grade, velocities of growth and ratio D/ρ [80]. This log to log graph shown in Figure 23 includes all parameter values found up to Jan. 2007 for both low- and high- grade gliomas. Low- grade gliomas are sited in bottom left rectangle (LGG), for 2mm/yr average velocities. Respectively, high grade gliomas (HCG) are positioned in the large rectangle, defined by D/ρ of 2 to 20 cm^2 and average velocities from 10mm/year to 200mm/year. On the left part gliomas with detectable mass, which can be cured with surgery, are placed.

Continuing, for the heterogeneous brain matter for high- grade gliomas, it is suggested in [69] that a typical value for the proliferation rate is $\rho=0.0012$ (1/day). This value for low- grade gliomas can be defined at $\rho=0.00012$ (1/day).

It is interesting to use the following table, reproduced from [81], where there is a list of the proposed values of each parameter that the latest glioma models use. Many of these parameters have been used in many experiments of the current work.



D and rho, for high- and low- grade gliomas

Parameter (namely)	Parameter Symbol	Value	Reference
Growth Rate	ρ	0.012 (1/day)	[82]
Diffusion Coefficient (Gray matter)	D_G	0.0013 ($\text{ cm}^2/\text{ day}$)	[52]
Diffusion Coefficient (White matter)	D_W	5 D_G ($\text{ cm}^2/\text{ day}$)	[69]
Initial number of tumor cells	N_0	10^5 cells	[83][84]
CT/MRI threshold density		400 (cells / mm^2)	[69]
CT/MRI threshold radius		1.5 cm	[82]
Cell death rate (chemotherapy)	k	0.0196 (1/day)	[85]
Number of fractions/ day	n	1-conventional 2-hyperfractionated	[86] [87]

Table 1 - The parameters of the diffusion model as proposed in the last 2 decades [81]

Resection modeling

Getting this further, one of the crucial steps of glioma modeling was to model cancer evolution after ectomy. This was firstly simulated in 1993 by setting the concentration of the ectomized area equal to zero and, then, allowing the surrounding malignant cells proliferate and diffuse until the sphere reaches 6cm diameter [52]. An example of ectomy, reproduced from, is given in Figure 24. The left part indicates the estimation of the initial tumor, the central part depicts the brain directly after resection and the right part indicates the recurred tumor after resection.

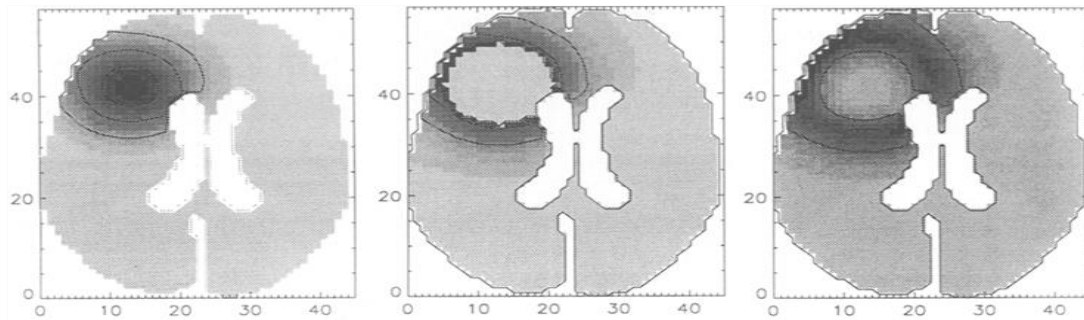


Figure 24 - Tracqui's simulation of a tumor resection. The parameter values of the model are $\rho = 0.012$ /day, $D = 10^{-7}$ cm²/s [52]

Low Grade Gliomas

Up to 1996, diffusive models studied high-grade gliomas due to their remarkably fast invasion. However, studying low-grade gliomas was important as well. Hence, in 1996, Woodward [83] suggested that speed of growth in low-grade tumors should be 10% of the respective one in high-grade gliomas, yielding satisfactory results.

Later in 2003, Mandonnet et al. [88] proposed that low-grade gliomas grew slowly, but linearly. This is mathematically derivable by Eq. 3, because the expanding velocity of a population, which follows only the diffusion and growth laws of this equation can be calculated as $2\sqrt{\rho D}$. Mandonnet et al. used clinical data reproduced from 27 patients to estimate that the average tumor velocity was 2mm per year.

Brain Tissue Heterogeneity

Up to 2000, researchers didn't take brain tissue anatomy into account. However, taking into account brain matter is of foremost importance, since the clinical observations of Giese indicate that migration of cancerous cells in myelin sheaths (white matter) is faster than the gray matter areas [89][90]. Thus, modeling of gliomas should take brain heterogeneity into account.

Indeed, Swanson first introduced the problem of brain heterogeneity by setting different diffusion coefficient in white and gray matter [69]. Simulations of this proliferation – diffusion equation were performed on a 3D MR structural image of the brain, with segmentation of white and gray matter. More specifically, Eq. 3 continued to hold, but for spatially variable D :

$$\frac{\partial c}{\partial t} \rightarrow \nabla \cdot (D(\mathbf{x})\nabla c) + \rho c$$

where $D(\mathbf{x})$ is the local diffusion coefficient, being either D_g or D_w for \mathbf{x} being in gray or white matter respectively. Figure 25 presents an example of simulation of tumor invasion of a high-grade glioma in the superior cerebral hemisphere using Swanson’s model. The first two images are taken at diagnosis time and the last two at death. The first diagnosis and death images (a and c) are slices as seen by Swanson’s standard threshold of detection. The rest ones (b and d) have been calculated out to 1.25% of the threshold (boundary) cell concentration defining the sensitive threshold of detection.

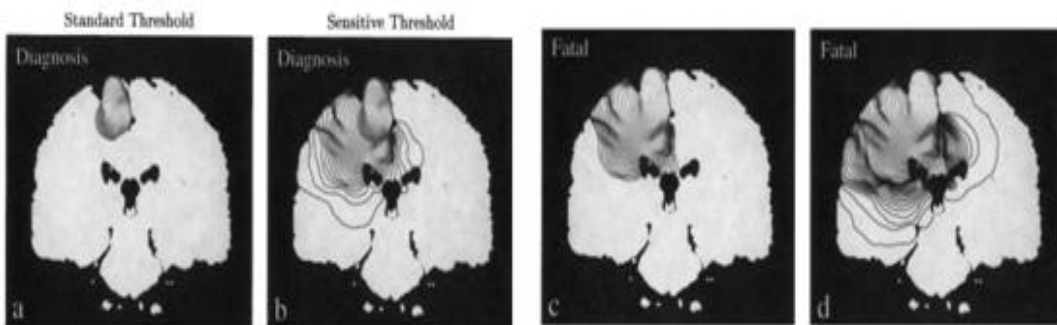


Figure 25 - Simulation of tumor invasion of a high-grade glioma in the superior cerebral hemisphere using Swanson’s model: (a) (b) at diagnosis; (c) (d) at death; (a) (c) as seen by Swanson’s standard threshold of detection; (b) (d) as calculated out to 1.25% of the threshold (boundary) cell concentration defining the sensitive threshold of detection [69].

Moreover, in order to have knowledge on the tissue type underlying the tumor, a brain atlas of normal brain was used. BrainWeb database [91] was available for extracting this information. Figure 26 shows an example of three different brain matter tissue types, taken from the BrainWeb atlas [92].

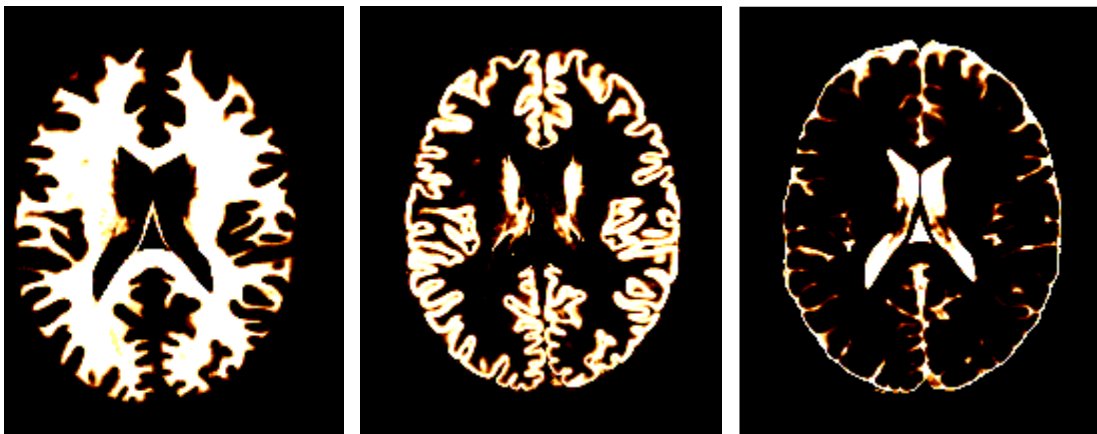


Figure 26- Example of tissue classes from Brainweb atlas brain (phantom). Left to Right: White matter, gray matter, CSF [92].

Anisotropic Cell Migration

In 2003 Price et al. opened the way for simulating the anisotropic growth of tumor along white matter fibers [16], in conjunction with the tracked fiber pathways [93]. Price et al. used T2- and Diffusion Tensor Imaging MRIs scans to determine whether DTI can identify abnormalities that appeared normal on T2. In order to incorporate the experimental findings supporting that the migration of glioma cells is facilitated along white fibers, in 2005, Jbabdi et al. and Clatz et al. [70][72] extended the model of Eq. 6 by introducing the local diffusion tensors derived from water diffusion, instead of gradient diffusion coefficients. Both models are based on MRIs and DTI-MRIs to take into account local geometry and directionality of white matter tracks, using the following advanced version of equation:

$$\frac{\partial c}{\partial t} \rightarrow \nabla \cdot (\mathbf{D}(\mathbf{x})\nabla c) + \rho c \quad 7$$

where $\mathbf{D}(\mathbf{x})$ is the local diffusion tensor which describes the directional tumor cell diffusion, i.e. a 3-by-3 symmetric positive definite matrix.

Mass Deformation

Apart from invasion directionality, Clatz et al. [72] used biomechanics to simulate the deformation of the surrounding area, due to tumor growth and pressure. This model uses a predictor of the mass effect induced by both the tumor proliferation and infiltration. Figure 27 shows an example of a simulation with that model, with the deformation of tissues presented. In 2007, Hogeia et al. [74] extended the anisotropic model by introducing an advection term in Eq. 6, with a two-way coupling with the underlying tissue elastic deformation.

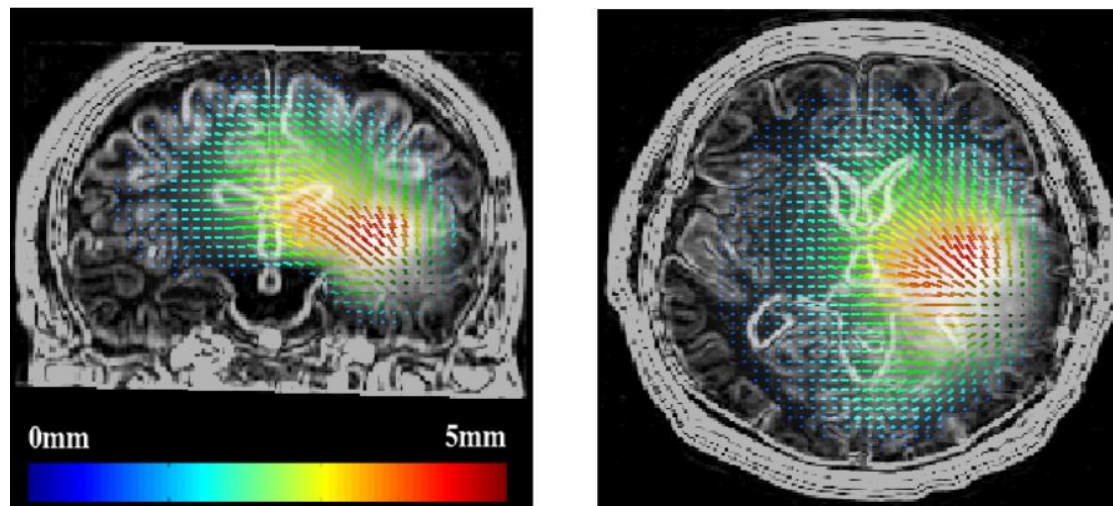


Figure 27 - Simulation of displacement of the tissues induced by the tumor mass effect, using Clatz's model [72]

Chemotherapy Modeling

Chemotherapy modeling is a quite blurred part of glioma models, which is mostly studied currently by researchers. Parameters that have to be taken into consideration should be extracted by histopathological and biostatistical data of specific patients [62]. Swanson has introduced a generalized net proliferation rate of chemotherapy as:

$$f(c) = \rho c - G(t)c$$

8

where $G(t)$ is the temporal profile of the chemotherapy treatments, assuming a loss proportional to the strength or amount of therapy at a given time. Swanson sets $G(t) = k$ when the chemotherapy is being administered and $G(t) = 0$ otherwise. k is actually a measure of effectiveness of chemotherapy. Thus, in order therapy to be effective and size of tumor to decrease, k should be larger than ρ , so that the net proliferation rate $f(c)$ is negative. This means the number of the dying cells is larger than the new born cells.

An example of chemotherapy application on real clinical MRI data, using Eq. 8 has been reproduced from [94]. In this example, k was intentionally set to the high value of $G(t) = 0.024$, so as the cancer to have shrinking effect. The data (18 MRI slices) has been acquired by Universität des Saarlandes Klinikum (Germany) within the scope of the Contracancrum project [95]. Some modeling results are given in Figure 28. The 3-dimensional representation of the initial and after-chemotherapy states are presented, accompanied by a sampled series of four MRI slices.

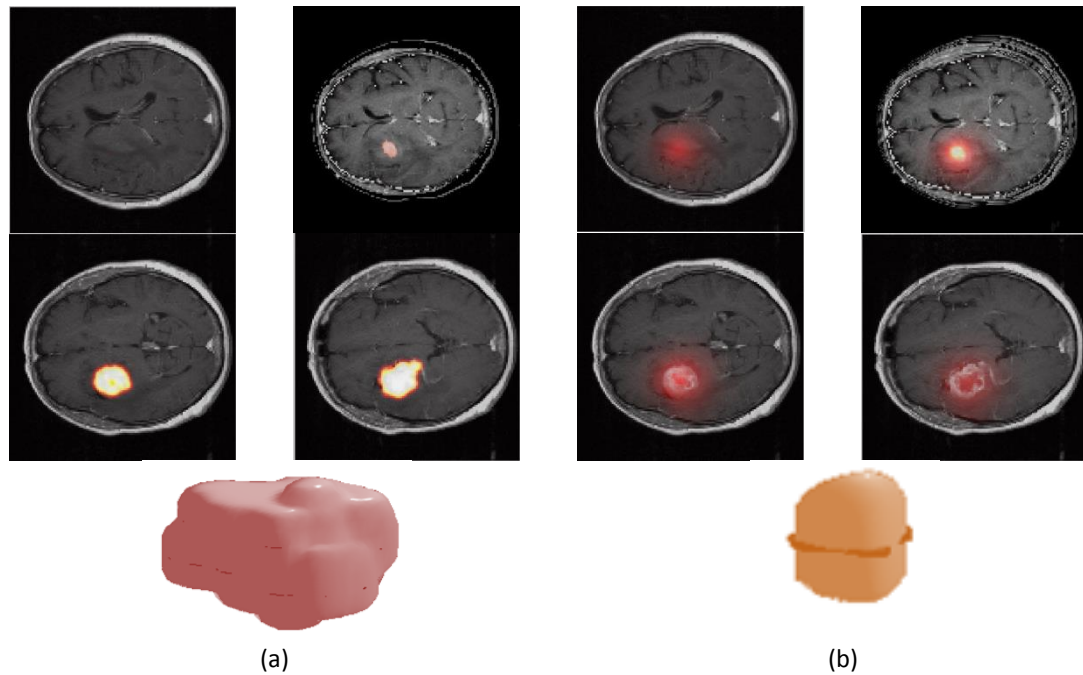


Figure 28- MRI and 3D representation of glioma in (a) initial state and (b) after chemotherapy simulation. 4 slices out of 18 slices are presented

3. Mathematical analysis on glioma model

The most common diffusive models use the diffusion-reaction equation (DRE) for simulating the spatiotemporal variation of tumor cell concentration. Nevertheless, despite the applications presented, there has been little work on studying the details of the mathematical solution and implementation of the 3 dimensional (3D) diffusion model and presenting a qualitative analysis of the algorithmic results. This work presents a complete mathematical framework on the solution of the DRE using different numerical schemes. This framework takes into account all characteristics of the latest models, such as brain tissue heterogeneity, anisotropic tumor cell migration, chemotherapy and resection modeling.

3.1. Deriving the Equation with Fick's Law

Suppose that we have a 3 dimensional space $\Omega \subset \mathbb{R}^3$, in which some matter is diffused. Let also $c: \Omega \times [0, T] \rightarrow \mathbb{R}$ be a function called *concentration* of the matter that is diffused in that medium.

We also assume open $R \subset \Omega$ with smooth boundary $\partial R = B$. The mass balance of the studied matter in R for a time interval $(t, t+\Delta t)$ is:

mass created by internal source = mass growth + mass flux rate through ∂R

We assume that mass flux obeys Fick's law [96]. According to this law, the flux goes from regions of high concentration to regions of low concentration, with a magnitude that is proportional to the concentration gradient. Thus, if $J: \Omega \times [0, T] \rightarrow \mathbb{R}^3$ is the mass flux function, then according to Fick's law:

$$J(\mathbf{x}, t) = -\mathbf{D}(\mathbf{x})\nabla c(\mathbf{x}, t), \mathbf{x} \in \Omega, t \in [0, T] \quad 9$$

where $\mathbf{D}(\mathbf{x})$ is known as the diffusion coefficient tensor.

If $P_R(t)$ is the rate in which the internal sources produce the diffused matter within R , then the law of mass conservation can be expressed as

$$P_R(t) = \int_R \frac{\partial c(\mathbf{x}, t)}{\partial t} d\mathbf{x} + \int_{\partial R} \frac{J(\mathbf{x}, t)}{\partial t} \mathbf{n} dS \quad 10$$

where \mathbf{n} is the normal vector, with $\mathbf{n} \perp \partial R$. If we assume that rate $P_R(t)$ can be expressed by the density $p(\mathbf{x}, t)$ of internal matter production then

$$P_R(t) = \int_R p(\mathbf{x}, t) d\mathbf{x} \quad 11$$

Then, by substituting Eq. 9 and Eq. 11 in Eq. 10, we get

$$\int_R p(\mathbf{x}, t) d\mathbf{x} = \int_R \frac{\partial c(\mathbf{x}, t)}{\partial t} d\mathbf{x} - \int_{\partial R} D(\mathbf{x}) \frac{\partial c(\mathbf{x}, t)}{\partial n} dS \quad 12$$

Where $\frac{\partial c(\mathbf{x}, t)}{\partial n} \equiv \nabla c(\mathbf{x}, t) \cdot \mathbf{n}$ is the directional derivative along the normal vector \mathbf{n} .

By using the divergence theorem, we can expressed the flux integral as

$$\int_{\partial R} D(\mathbf{x}) \frac{\partial c(\mathbf{x}, t)}{\partial n} dS = \int_R \operatorname{div}(\mathbf{D}(\mathbf{x}) \operatorname{grad}(c(\mathbf{x}, t))) d\mathbf{x} \quad 13$$

Thus, Eq. 12 can be now written as

$$\int_R p(\mathbf{x}, t) d\mathbf{x} = \int_R \frac{\partial c(\mathbf{x}, t)}{\partial t} d\mathbf{x} - \int_R \operatorname{div}(\mathbf{D}(\mathbf{x}) \operatorname{grad}(c(\mathbf{x}, t))) d\mathbf{x} \quad 14$$

or, equivalently:

$$\int_R \left(\frac{\partial c(\mathbf{x}, t)}{\partial t} - \operatorname{div}(\mathbf{D}(\mathbf{x}) \operatorname{grad}(c(\mathbf{x}, t))) - p(\mathbf{x}, t) \right) d\mathbf{x} = 0, \forall R \subset \Omega \quad 15$$

However, since Eq. 15 holds, $\forall R \subset \Omega$, if $\frac{\partial c(\mathbf{x}, t)}{\partial t} - \operatorname{div}(\mathbf{D}(\mathbf{x}) \operatorname{grad}(c(\mathbf{x}, t))) - p(\mathbf{x}, t)$ is constant, then it must be zero in R . Then

$$\frac{\partial c(\mathbf{x}, t)}{\partial t} - \operatorname{div}(\mathbf{D}(\mathbf{x}) \operatorname{grad}(c(\mathbf{x}, t))) = p(\mathbf{x}, t), \mathbf{x} \in \Omega, t > 0 \quad 16$$

Equation 16 constitutes the mathematical expression of mass conservation law and is a local equation (i.e. holds at any point of Ω at any time).

Continuing, $p(\mathbf{x}, t)$ can either be expressed as a function of \mathbf{x} and t , or depend on concentration $c(\mathbf{x}, t)$. In an absorbing medium we usually assume that the absorbed matter is proportional to matter concentration, i.e.

$$p(\mathbf{x}, t) = q(\mathbf{x}, t)c(\mathbf{x}, t) + n(\mathbf{x}, t) \quad 17$$

where $q(\mathbf{x}, t)$ expresses the absorbing identities, that generally change from point to point and $n(\mathbf{x}, t)$ expresses the density of the internal sources of matter production.

Thus, Eq. 16 can now be expressed as:

$$\frac{\partial c(\mathbf{x}, t)}{\partial t} - \operatorname{div}(\mathbf{D}(\mathbf{x}) \operatorname{grad}(c(\mathbf{x}, t))) = q(\mathbf{x}, t)c(\mathbf{x}, t) + n(\mathbf{x}, t) \quad 18$$

Especially for the case of cancer growth, this source term is proposed to depend on concentration, thus $p(\mathbf{x}, t) = f(c(\mathbf{x}, t))$. More specifically, exponential source term is mainly used, i.e. $f(c(\mathbf{x}, t)) = \rho c(\mathbf{x}, t)$. If we set this value to 18, then

$$\frac{\partial c(\mathbf{x}, t)}{\partial t} = \text{div}(\mathbf{D}(\mathbf{x})\text{grad}(c(\mathbf{x}, t))) + f(c(\mathbf{x}, t)) \quad 19$$

Equation 19 is a partial 2nd order differential equation. Before studying its solution, we must expand it in 3 dimensions. Assuming that the diffusion tensor at a point $\mathbf{x}=(x_1, x_2, x_3)$ is $\mathbf{D}(\mathbf{x})$ and is

$$\mathbf{D}(\mathbf{x}) = \begin{vmatrix} D_{11}(\mathbf{x}) & D_{12}(\mathbf{x}) & D_{13}(\mathbf{x}) \\ D_{12}(\mathbf{x}) & D_{22}(\mathbf{x}) & D_{23}(\mathbf{x}) \\ D_{13}(\mathbf{x}) & D_{23}(\mathbf{x}) & D_{33}(\mathbf{x}) \end{vmatrix} \quad 20$$

Eq. 19 can be expanded in 3 dimensions using the definitions of divergence (*div*) and gradient (*grad*) operators as

$$\frac{\partial c}{\partial t} = \sum_{i=1}^3 \sum_{j=1}^3 \frac{\partial^2 c}{\partial x_i \partial x_j} D_{ij} + \sum_{j=1}^3 \frac{\partial c}{\partial x_j} \left(\sum_{i=1}^3 \frac{\partial D_{ij}}{\partial x_i} \right) + f(c) \quad 21$$

3.2. Numerical Solving

The equation 21 is a 2nd order partial differential equation. Such an equation can be solved using numerical methods. Some of the most commonly used numerical methods are 1) the Finite Differences Method, 2) the Finite Element method and the 3) Finite Volumes Method. In order to be able to find an approximation of the equation or its solution, we must ensure that we have set

- The boundary conditions, i.e. either the value of concentration or its derivative at points that are on the boundary of our volume of interest.
- The initial concentration $c(\mathbf{x}, 0)$

For this model, we have used finite differences to study the solution of Eq. 21, since this method is mainly used in the most important models of glioma growth simulation. Later, we'll see a solver with Finite Elements.

The finite differences method is trying to approximate the solutions to differential equations using finite difference equations to approximate derivative. There are several ways for approximating the local derivatives. Some of the most popular are the forward Euler method, the backward Euler method, the Crank Nikolson method and the θ -methods.

3.2.1. The Forward Euler Method

Let's study how the Forward Euler method approximates the solution of Eq. 21. If we quantify concentration c as $c(n\Delta T, i\Delta X, j\Delta Y, k\Delta Z) \equiv C_{i,j,k}^n$ and diffusion tensor as $D_{pq}(i\Delta X, j\Delta Y, k\Delta Z) \equiv D_{pq,i,j,k}^n$ for $i \in \{0, \dots, N_X - 1\}, j \in \{0, \dots, N_Y - 1\}, k \in \{0, \dots, N_Z -$

1} and $p, q \in \{1,2,3\}$ then the partial derivatives of Eq. 21 at point $(i\Delta X, j\Delta Y, k\Delta Z)$ for Forward Euler method are approximated as:

$$\begin{aligned} \frac{\partial c}{\partial t} &\rightarrow \frac{C_{i,j,k}^{n+1} - C_{i,j,k}^n}{\Delta T} \\ \frac{\partial c}{\partial x} &\rightarrow \frac{C_{i+1,j,k}^n - C_{i-1,j,k}^n}{2\Delta X} \\ \frac{\partial^2 c}{\partial x^2} &\rightarrow \frac{C_{i+1,j,k}^n - 2C_{i,j,k}^n + C_{i-1,j,k}^n}{\Delta X^2} \\ \frac{\partial^2 c}{\partial x \partial y} &\rightarrow \frac{C_{i+1,j+1,k}^n + C_{i-1,j-1,k}^n - C_{i+1,j-1,k}^n - C_{i-1,j+1,k}^n}{4\Delta X \Delta Y} \\ \frac{D_{pq}}{\partial x} &\rightarrow \frac{D_{pq,i+1,j,k} - D_{pq,i-1,j,k}}{2\Delta X} \end{aligned} \quad 22$$

and similarly for $\frac{\partial c}{\partial y}$, $\frac{\partial c}{\partial z}$, $\frac{\partial^2 c}{\partial y^2}$, $\frac{\partial^2 c}{\partial z^2}$, $\frac{\partial^2 c}{\partial x \partial z}$, $\frac{\partial^2 c}{\partial y \partial z}$, $\frac{D_{pq}}{\partial y}$ and $\frac{D_{pq}}{\partial z}$.

If any of the neighboring $C_{i,j,k}^n$ is a boundary point, then its according value will be as defined during setting the boundary conditions (generally zero gradient). Before, continuing it is noteworthy to mention that, in order forward Euler method to be stable, we must choose $\Delta T, \Delta X, \Delta Y$ and ΔZ that satisfy the following stability condition, which is derived from Courant–Friedrichs–Lewy condition [97]:

$$\Delta T \leq \min_{x,y,z} \left(\frac{1}{2 \frac{D_{11}(x,y,z)}{\Delta X^2} + \frac{D_{22}(x,y,z)}{\Delta Y^2} + \frac{D_{33}(x,y,z)}{\Delta Z^2}} \right) \quad 23$$

Deriving the Linear System

Assuming that the previous condition holds, we carry on with substituting the approximations of local derivatives in Eq. 21. Thus, we derive

$$\frac{C_{i,j,k}^{n+1} - C_{i,j,k}^n}{\Delta T} = [A(i,j,k)_0 \quad A(i,j,k)_2 \quad \dots \quad A(i,j,k)_{18}] \begin{bmatrix} C_{i-1,j-1,k}^n \\ C_{i-1,j,k-1}^n \\ \dots \\ C_{i+1,j+1,k}^n \end{bmatrix} + f(C_{i,j,k}^n) \quad 24$$

where

$$\begin{aligned} A(i,j,k)_2 &= \frac{D_{11,i,j,k}}{\Delta X^2} - \frac{D_{11,i+1,j,k} - D_{11,i-1,j,k}}{4\Delta X^2} - \frac{D_{21,i,j+1,k} - D_{21,i,j-1,k}}{4\Delta X \Delta Y} - \frac{D_{31,i,j,k+1} - D_{31,i,j,k-1}}{4\Delta X \Delta Z} \\ A(i,j,k)_6 &= \frac{D_{22,i,j,k}}{\Delta Y^2} - \frac{D_{12,i+1,j,k} - D_{12,i-1,j,k}}{4\Delta X \Delta Y} - \frac{D_{22,i,j+1,k} - D_{22,i,j-1,k}}{4\Delta Y^2} - \frac{D_{32,i,j,k+1} - D_{32,i,j,k-1}}{4\Delta Y \Delta Z} \\ A(i,j,k)_8 &= \frac{D_{33,i,j,k}}{\Delta Z^2} - \frac{D_{13,i+1,j,k} - D_{13,i-1,j,k}}{4\Delta X \Delta Z} - \frac{D_{23,i,j+1,k} - D_{23,i,j-1,k}}{4\Delta Y \Delta Z} - \frac{D_{33,i,j,k+1} - D_{33,i,j,k-1}}{4\Delta Z^2} \\ A(i,j,k)_9 &= -2 \frac{D_{11,i,j,k}}{\Delta X^2} - 2 \frac{D_{22,i,j,k}}{\Delta Y^2} - 2 \frac{D_{33,i,j,k}}{\Delta Z^2} \\ A(i,j,k)_{10} &= \frac{D_{33,i,j,k}}{\Delta Z^2} + \frac{D_{13,i+1,j,k} - D_{13,i-1,j,k}}{4\Delta X \Delta Z} + \frac{D_{23,i,j+1,k} - D_{23,i,j-1,k}}{4\Delta Y \Delta Z} + \frac{D_{33,i,j,k+1} - D_{33,i,j,k-1}}{4\Delta Z^2} \\ A(i,j,k)_{12} &= \frac{D_{22,i,j,k}}{\Delta Y^2} + \frac{D_{12,i+1,j,k} - D_{12,i-1,j,k}}{4\Delta X \Delta Y} + \frac{D_{22,i,j+1,k} - D_{22,i,j-1,k}}{4\Delta Y^2} + \frac{D_{32,i,j,k+1} - D_{32,i,j,k-1}}{4\Delta Y \Delta Z} \end{aligned}$$

$$\begin{aligned}
 A(i, j, k)_{16} &= \frac{D_{11,i,j,k}}{\Delta X^2} + \frac{D_{11,i+1,j,k} - D_{11,i-1,j,k}}{4\Delta X^2} + \frac{D_{21,i,j+1,k} - D_{21,i,j-1,k}}{4\Delta X\Delta Y} + \frac{D_{31,i,j,k+1} - D_{31,i,j,k-1}}{4\Delta X\Delta Z} \\
 A(i, j, k)_0 &= -A(i, j, k)_4 = -A(i, j, k)_{14} = A(i, j, k)_{18} = \frac{D_{12,i,j,k}}{2\Delta X\Delta Y} \\
 A(i, j, k)_1 &= -A(i, j, k)_3 = -A(i, j, k)_{15} = A(i, j, k)_{17} = \frac{D_{13,i,j,k}}{2\Delta X\Delta Z} \\
 A(i, j, k)_5 &= -A(i, j, k)_7 = -A(i, j, k)_{11} = A(i, j, k)_{13} = \frac{D_{23,i,j,k}}{2\Delta Y\Delta Z}
 \end{aligned} \tag{25}$$

Thus, if we get the vectorized version of $C_{i,j,k}^n$ at time $n\Delta T$, as:

$$\mathbf{c}^n \equiv \left[\underbrace{C_{0,0,0}^n \quad C_{0,0,1}^n \quad \dots \quad C_{0,0,N_Z-1}^n \quad C_{0,1,0}^n \quad \dots \quad C_{0,N_Y-2,N_Z-1}^n \quad C_{0,N_Y-1,0}^n \quad \dots \quad C_{1,0,0}^n \quad \dots \quad C_{N_X-1,N_Y-1,N_Z-1}^n}_{N_X N_Y N_Z} \right]^T \tag{26}$$

the overall solution of the equation at time $n+1$ can be found by solving

$$\frac{\mathbf{c}^{n+1} - \mathbf{c}^n}{\Delta T} = \mathbf{A}\mathbf{c}^n + F(\mathbf{c}^n) \tag{27}$$

where \mathbf{A} is a $N_X N_Y N_Z \times N_X N_Y N_Z$ matrix with its elements defined as

$$\mathbf{A}_{ml} = \begin{cases} A(i, j, k)_0, l = m - N_Y N_Z - N_Z & A(i, j, k)_{10}, l = m + 1 \\ A(i, j, k)_1, l = m - N_Y N_Z - 1 & A(i, j, k)_{11}, l = m + N_Z - 1 \\ A(i, j, k)_2, l = m - N_Y N_Z & A(i, j, k)_{12}, l = m + N_Z \\ A(i, j, k)_3, l = m - N_Y N_Z + 1 & A(i, j, k)_{13}, l = m + N_Z + 1 \\ A(i, j, k)_4, l = m - N_Y N_Z + N_Z & A(i, j, k)_{14}, l = m + N_Y N_Z - N_Z \\ A(i, j, k)_5, l = m - N_Z - 1 & A(i, j, k)_{15}, l = m + N_Y N_Z - 1 \\ A(i, j, k)_6, l = m - N_Z & A(i, j, k)_{16}, l = m + N_Y N_Z \\ A(i, j, k)_7, l = m - N_Z + 1 & A(i, j, k)_{17}, l = m + N_Y N_Z + 1 \\ A(i, j, k)_8, l = m - 1 & A(i, j, k)_{18}, l = m + N_Y N_Z + N_Z \\ A(i, j, k)_9, l = m & 0, \text{ otherwise} \end{cases} \tag{28}$$

$$m = iN_Y N_Z + jN_Z + k \text{ and } m, l \in \{0, \dots, N_X N_Y N_Z - 1\}$$

and $F(\mathbf{c}^n)$ is the vectorized version of $f(C_{i,j,k}^n)$:

$$F(\mathbf{c}^n) \equiv [f(C_{0,0,0}^n) \quad f(C_{0,0,1}^n) \quad \dots \quad f(C_{N_X-1,N_Y-1,N_Z-1}^n)]^T \tag{29}$$

The choice of the vectorization operator is discussed in later.

The sparse matrix of the system

Matrix \mathbf{A} is a $N_X N_Y N_Z \times N_X N_Y N_Z$ sparse matrix with 19 diagonals, as shown in Figure 29. The light pinkish areas values are zero and the dark blue lines are the non-zero diagonals. Note that the thicker lines are 3 diagonals in a row, while the thin ones are single. This form is called tridiagonal with fringes: It has one central and four more tridiagonal areas, while having four more single-diagonal areas [98]. .

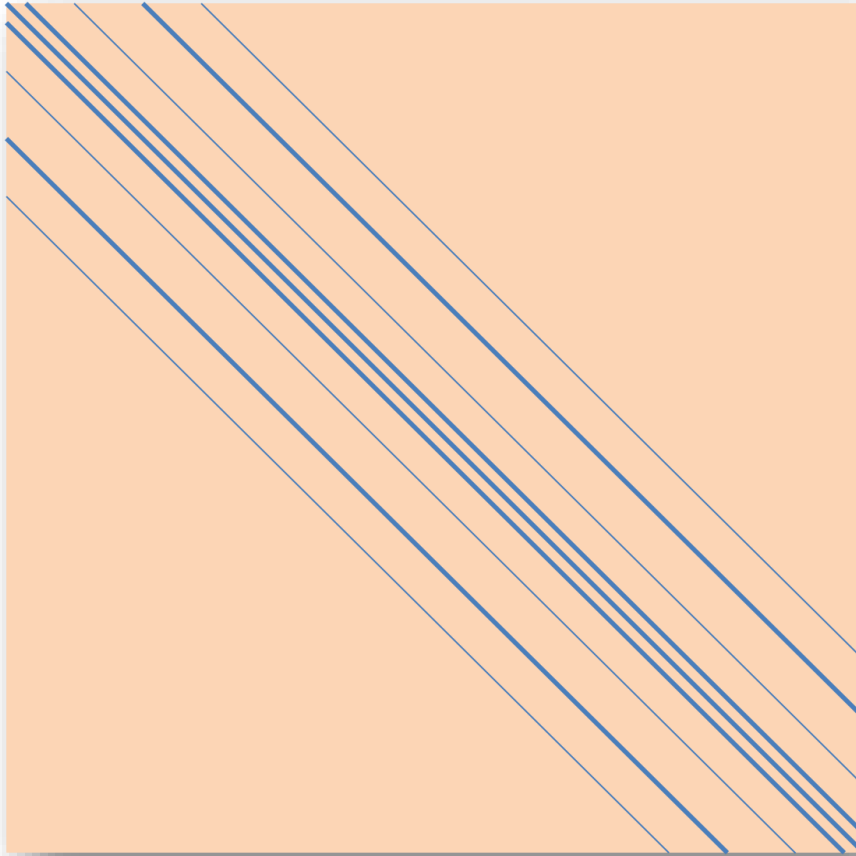


Figure 29 - The sparse matrix A and its 19 diagonals

Incorporating growth rate in the linear system

One important stage of GBM modeling is choosing the operator F , according to the common net proliferation rates, namely the exponential, the Verhulst and the Gompertz laws.

Exponential Rate

If the net proliferation rate is exponential:

$$f(c) = \rho c \quad 30$$

then according to Eq. 29

$$F(\mathbf{C}^n) = [\rho C_{0,0,0}^n \quad \rho C_{0,0,1}^n \quad \dots \quad \rho C_{N_X-1,N_Y-1,N_Z-1}^n]^T \quad 31$$

or equivalently

$$F(\mathbf{C}^n) = \rho \mathbf{C}^n \quad 32$$

Verhulst Rate

If the net proliferation rate follows the Verhulst (or logistic) law:

$$f(c) = \rho c \frac{c_m - c}{c_m} \quad 33$$

where c_m is the maximum value that concentration can reach, then according to Eq. 29:

$$F(\mathbf{C}^n) = \left[\rho C_{0,0,0}^n \frac{c_m - C_{0,0,0}^n}{c_m} \quad \rho C_{0,0,1}^n \frac{c_m - C_{0,0,1}^n}{c_m} \quad \dots \quad \rho C_{N_X-1, N_Y-1, N_Z-1}^n \frac{c_m - C_{N_X-1, N_Y-1, N_Z-1}^n}{c_m} \right]^T \quad 34$$

or equivalently

$$\begin{aligned} F(\mathbf{C}^n) &= \begin{bmatrix} \rho C_{0,0,0}^n & 0 & \dots & 0 \\ 0 & \rho C_{0,0,1}^n & \dots & 0 \\ \dots & \dots & \dots & \dots \\ 0 & 0 & \dots & \rho C_{N_X-1, N_Y-1, N_Z-1}^n \end{bmatrix} \begin{bmatrix} \frac{c_m - C_{0,0,0}^n}{c_m} & \frac{c_m - C_{0,0,1}^n}{c_m} & \dots & \frac{c_m - C_{N_X-1, N_Y-1, N_Z-1}^n}{c_m} \end{bmatrix}^T \\ &= \frac{\rho}{c_m} \begin{bmatrix} C_{0,0,0}^n & 0 & \dots & 0 \\ 0 & C_{0,0,1}^n & \dots & 0 \\ \dots & \dots & \dots & \dots \\ 0 & 0 & \dots & C_{N_X-1, N_Y-1, N_Z-1}^n \end{bmatrix} \left(\begin{bmatrix} c_m \\ c_m \\ \dots \\ c_m \end{bmatrix} - \begin{bmatrix} C_{0,0,0}^n \\ C_{0,0,1}^n \\ \dots \\ C_{N_X-1, N_Y-1, N_Z-1}^n \end{bmatrix} \right) \end{aligned} \quad 35$$

This that can be written as

$$F(\mathbf{C}^n) = \frac{\rho}{c_m} \text{diag}(\mathbf{C}^n) (c_m \mathbf{1}^{1 \times N_X N_Y N_Z} - \mathbf{C}^n) \quad 36$$

where

- diag of a $1 \times N$ vector V is a $N \times N$ matrix, which's diagonal values are the values of V , i.e. $\text{diag}(V)_{ij} = V_{1i}$ when $i=j$, and 0 when $i \neq j$
- $\mathbf{1}^{M \times N}$ is a $M \times N$ vector with all its values equal to 1.

Gompertz Rate

If the net proliferation rate follows the Gompertz law:

$$f(c) = \rho c \cdot \ln\left(\frac{c_m}{c}\right) \quad 37$$

where c_m is the maximum value that concentration can reach, then according to Eq. 29

$$F(\mathbf{C}^n) = \left[\rho C_{0,0,0}^n (\ln c_m - \ln C_{0,0,0}^n) \quad \dots \quad \rho C_{N_X-1, N_Y-1, N_Z-1}^n (\ln c_m - \ln C_{N_X-1, N_Y-1, N_Z-1}^n) \right]^T \quad 38$$

or equivalently

$$F(\mathbf{C}^n) = \rho \begin{bmatrix} C_{0,0,0}^n & 0 & \dots & 0 \\ 0 & C_{0,0,1}^n & \dots & 0 \\ \dots & \dots & \dots & \dots \\ 0 & 0 & \dots & C_{N_X-1, N_Y-1, N_Z-1}^n \end{bmatrix} \left(\ln \begin{bmatrix} c_m \\ c_m \\ \dots \\ c_m \end{bmatrix} - \ln \begin{bmatrix} C_{0,0,0}^n \\ C_{0,0,1}^n \\ \dots \\ C_{N_X-1, N_Y-1, N_Z-1}^n \end{bmatrix} \right) \quad 39$$

This can be written as

$$F(\mathbf{C}^n) = \rho \text{diag}(\mathbf{C}^n) (\ln(c_m \mathbf{1}^{1 \times N_X N_Y N_Z}) - \ln \mathbf{C}^n) \quad 40$$

Table 1 summarizes the derived vectorization operator F for the commonly used exponential, logistic and Gompertz proliferation rates.

Proliferation Rate	Constant Rate $f(c)$	Vectorization Operator $F(\mathbf{C}^n)$
Exponential	$f(c) = \rho c$	$F(\mathbf{C}^n) = \rho \mathbf{C}^n$
Verhulst (logistic)	$f(c) = \rho c \frac{c_m - c}{c_m}$	$F(\mathbf{C}^n) = \frac{\rho}{c_m} \text{diag}(\mathbf{C}^n)(c_m \mathbf{1}^{1 \times N_X N_Y N_Z} - \mathbf{C}^n)$
Gompertz	$f(c) = \rho c \cdot \ln\left(\frac{c}{c_m}\right)$	$F(\mathbf{C}^n) = \rho \text{diag}(\mathbf{C}^n)(\ln(c_m \mathbf{1}^{1 \times N_X N_Y N_Z}) - \ln \mathbf{C}^n)$
$\text{diag} \begin{bmatrix} x_1 \\ x_2 \\ \dots \\ x_N \end{bmatrix} = \begin{bmatrix} x_1 & 0 & \dots & 0 \\ 0 & x_2 & & 0 \\ \dots & \dots & \dots & \dots \\ 0 & 0 & \dots & x_N \end{bmatrix}$		$\mathbf{1}^{1 \times N} = \left. \begin{bmatrix} 1 \\ 1 \\ \dots \\ 1 \\ 1 \end{bmatrix} \right\} N$

Table 2 – Summary of vectorization factor F for different proliferation rates

The final linear system

After having acquired Eq. 27, a direct solution can be found by iteratively calculating

$$\mathbf{C}^{n+1} = (\mathbf{I} + \Delta T \mathbf{A}) \mathbf{C}^n + \Delta T \cdot F(\mathbf{C}^n) \tag{41}$$

where \mathbf{I} is the $N_X N_Y N_Z \times N_X N_Y N_Z$ identity matrix. In order this iteration to be able to start, we must provide the initial concentration \mathbf{C}^0 .

This is the solution of the forward Euler method. This is called forward, because the next-time approximation of concentration can be directly approximated as a linear combination of the previous-time approximation. This is a very easy to implement solution, but numerical stability has to be ensured by Eq. 23.

3.2.2. The Backward Euler Method

Let's now study the backward Euler method in approximation of the local derivatives in the internal points of Eq. 21. Finding a solution using the Backward Euler scheme is desirable, because there is no constraint in the numerical stability of this method. According to the backward Euler method, the local derivatives can now be approximated as:

$$\begin{aligned} \frac{\partial c}{\partial t} &\rightarrow \frac{C_{i,j,k}^{n+1} - C_{i,j,k}^n}{\Delta T} \\ \frac{\partial c}{\partial x} &\rightarrow \frac{C_{i+1,j,k}^{n+1} - C_{i-1,j,k}^{n+1}}{2\Delta X} \\ \frac{\partial^2 c}{\partial x^2} &\rightarrow \frac{C_{i+1,j,k}^{n+1} - 2C_{i,j,k}^{n+1} + C_{i-1,j,k}^{n+1}}{\Delta X^2} \\ \frac{\partial^2 c}{\partial x \partial y} &\rightarrow \frac{C_{i+1,j+1,k}^{n+1} + C_{i-1,j-1,k}^{n+1} - C_{i+1,j-1,k}^{n+1} - C_{i-1,j+1,k}^{n+1}}{4\Delta X \Delta Y} \\ \frac{D_{pq}}{\partial x} &\rightarrow \frac{D_{pq,i+1,j,k} - D_{pq,i-1,j,k}}{2\Delta X} \end{aligned} \tag{42}$$

and similarly for $\frac{\partial c}{\partial y}, \frac{\partial c}{\partial z}, \frac{\partial^2 c}{\partial y^2}, \frac{\partial^2 c}{\partial z^2}, \frac{\partial^2 c}{\partial x \partial z}, \frac{\partial^2 c}{\partial y \partial z}, \frac{D_{pq}}{\partial y}$ and $\frac{D_{pq}}{\partial z}$.

Linear System Derivation

Similarly to the forward Euler, by substituting the approximations of local derivatives in Eq. 21, we get

$$\frac{\mathbf{C}^{n+1} - \mathbf{C}^n}{\Delta T} = \mathbf{A}\mathbf{C}^{n+1} + F(\mathbf{C}^{n+1}) \quad 43$$

where \mathbf{A} is exactly the same matrix of Eq. 27 and F is the same vectorization operator of Eq. 29. The formulations of $F(\mathbf{C}^n)$ and $F(\mathbf{C}^{n+1})$ for exponential, Verhulst and Gompertz proliferation rates hold as in Forward Euler.

The final linear system

After having acquired equation (3.39), the concentration of the glioma cells at time t can be found by iteratively solving the linear system

$$(\mathbf{I} - \Delta T \mathbf{A})\mathbf{C}^{n+1} - \Delta T \cdot F(\mathbf{C}^{n+1}) = \mathbf{C}^n \quad 44$$

till fictitious time t is reached, starting with given \mathbf{C}^0 . The linear system at each iteration is big and can be expressed with a big, sparse, symmetric and positive definite matrix, thus an iterative method for solving linear systems, e.g. the conjugate gradient method can be used. Unconditional stability and accuracy are advantages of the backward Euler method, in contrary to computational and storage load that has to be performed

3.2.3. The θ -Methods

The θ -methods can be used for the approximation of the local derivatives in the internal points of Eq. 21. The θ -methods use the balancing parameter $\theta \in [0,1]$ so as to combine forward and backward schemes. According to the θ -methods, the local derivatives can now be approximated as:

$$\begin{aligned} \frac{\partial c}{\partial t} &\rightarrow \frac{C_{i,j,k}^{n+1} - C_{i,j,k}^n}{\Delta T} \\ \frac{\partial c}{\partial x} &\rightarrow (1 - \theta) \frac{C_{i+1,j,k}^n - C_{i-1,j,k}^n}{2\Delta X} + \theta \frac{C_{i+1,j,k}^{n+1} - C_{i-1,j,k}^{n+1}}{2\Delta X} \\ \frac{\partial^2 c}{\partial x^2} &\rightarrow (1 - \theta) \frac{C_{i+1,j,k}^n - 2C_{i,j,k}^n + C_{i-1,j,k}^n}{\Delta X^2} + \theta \frac{C_{i+1,j,k}^{n+1} - 2C_{i,j,k}^{n+1} + C_{i-1,j,k}^{n+1}}{\Delta X^2} \\ \frac{\partial^2 c}{\partial x \partial y} &\rightarrow (1 - \theta) \frac{C_{i+1,j+1,k}^n + C_{i-1,j-1,k}^n - C_{i+1,j-1,k}^n - C_{i-1,j+1,k}^n}{4\Delta X \Delta Y} + \\ &\theta \frac{C_{i+1,j+1,k}^{n+1} + C_{i-1,j-1,k}^{n+1} - C_{i+1,j-1,k}^{n+1} - C_{i-1,j+1,k}^{n+1}}{4\Delta X \Delta Y} \\ \frac{D_{pq}}{\partial x} &\rightarrow \frac{D_{pq,i+1,j,k} - D_{pq,i-1,j,k}}{2\Delta X} \\ c &\rightarrow (1 - \theta)C_{i,j,k}^n + \theta C_{i,j,k}^{n+1} \end{aligned} \quad 45$$

and similarly for $\frac{\partial c}{\partial y}, \frac{\partial c}{\partial z}, \frac{\partial^2 c}{\partial y^2}, \frac{\partial^2 c}{\partial z^2}, \frac{\partial^2 c}{\partial x \partial z}, \frac{\partial^2 c}{\partial y \partial z}, \frac{D_{pq}}{\partial y}$ and $\frac{D_{pq}}{\partial z}$.

Note that Backward Euler, Forward Euler and Crank-Nikolson are θ -methods, for $\theta=1,0$ and 0.5 respectively.

Linear System Derivation

Similarly to the forward and backward Euler, by substituting the approximations of local derivative, we derive

$$\frac{\mathbf{C}^{n+1} - \mathbf{C}^n}{\Delta T} = (1 - \theta)\mathbf{A}\mathbf{C}^n + \theta\mathbf{A}\mathbf{C}^{n+1} + (1 - \theta)F(\mathbf{C}^n) + \theta F(\mathbf{C}^{n+1}) \quad 46$$

where \mathbf{A} is exactly the same matrix of Eq. 27 and F is the same vectorization operator of Eq. 29. The formulations of $F(\mathbf{C}^n)$ and $F(\mathbf{C}^{n+1})$ for exponential, Verhulst and Gompertz proliferation rates hold as in Forward Euler.

The final linear system

After having acquired Eq. 46 the concentration of the glioma cells at time t can be found by iteratively solving the following linear system of equations:

$$(\mathbf{I} - \theta\Delta T\mathbf{A})\mathbf{C}^{n+1} - \theta\Delta TF(\mathbf{C}^{n+1}) = (\mathbf{I} + (1 - \theta)\Delta T\mathbf{A})\mathbf{C}^n + (1 - \theta)\Delta TF(\mathbf{C}^n) \quad 47$$

As, in backward Euler, a method for solving linear systems is required. A discussion on the choice of parameter θ , for the commonly used exponential proliferation rate $f(c) = \rho c$, is described in the next section.

The θ -method is a more accurate method than Backward Euler, is flexible due to choice of θ , is unconditionally stable, but a high computational and storage load has to be performed as well.

Choice of θ

After having acquired the formulation of the linear system, it is interesting to choose the parameter θ with care. If we neglect the diffusion term in Eq. 47, we obtain the scheme

$$\frac{\mathbf{C}^{n+1} - \mathbf{C}^n}{\Delta T} = (1 - \theta)F(\mathbf{C}^n) + \theta F(\mathbf{C}^{n+1}) \quad 48$$

For simplicity, it is supposed that the net proliferation rate is exponential, thus

$$\frac{\mathbf{C}^{n+1} - \mathbf{C}^n}{\Delta T} = (1 - \theta)\rho\mathbf{C}^n + \theta\rho\mathbf{C}^{n+1} \quad 49$$

or equivalently

$$\mathbf{C}^{n+1} = \frac{1 + \rho\Delta T - \theta\rho\Delta T}{1 - \theta\rho\Delta T}\mathbf{C}^n \quad 50$$

If the initial concentration is \mathbf{C}^0 then, iteratively, we get

$$\mathbf{c}^n = \left(\frac{1 + \rho\Delta T - \theta\rho\Delta T}{1 - \theta\rho\Delta T} \right)^n \mathbf{c}^0 \quad 51$$

However, the analytical solution for the exponential law is

$$\mathbf{c}^n = e^{n\rho\Delta T} \mathbf{c}^0 \quad 52$$

Thus, by substituting Eq. 52 to Eq. 51, we derive

$$(e^{\rho\Delta T})^n = \left(\frac{1 + \rho\Delta T - \theta\rho\Delta T}{1 - \theta\rho\Delta T} \right)^n \quad 53$$

which gives the relationship

$$\theta = \frac{1 + \rho\Delta T - e^{\rho\Delta T}}{\rho\Delta T(1 - e^{\rho\Delta T})} \quad 54$$

or

$$\theta = \frac{1}{\rho\Delta T} - \frac{1}{1 - e^{\rho\Delta T}} \quad 55$$

This is a good estimate for parameter θ . This estimate could also be used for Verhulst or Gompertz proliferation rate.

3.2.4. The Crank Nikolson Method

The Crank Nikolson method is widely used for diffusion equations, because it is unconditionally stable. The approximate solutions can still contain spurious oscillations if the ratio of time step to the square of space step is large (typically larger than 1/2). When this holds, backward Euler method is often used, which is both stable and immune to oscillations. Otherwise, Crank Nikolson scheme is more accurate than backward Euler.

The Crank Nikolson scheme is a θ -method for $\theta=1/2$. Thus, everything said for θ -methods in the previous chapter applies here, for $\theta=1/2$. Thus, the concentration of the glioma cells at time t can be found by iteratively solving the following linear system of equations:

$$\left(\mathbf{I} - \frac{1}{2}\Delta T\mathbf{A} \right) \mathbf{c}^{n+1} - \frac{1}{2}\Delta T\mathbf{F}(\mathbf{c}^{n+1}) = \left(\mathbf{I} + \frac{1}{2}\Delta T\mathbf{A} \right) \mathbf{c}^n + \frac{1}{2}\Delta T\mathbf{F}(\mathbf{c}^n) \quad 56$$

Summary

Now, we can present collectively the formulation of the iterative linear systems that produce the solution of the diffusion Eq. 21. Table 3 presents the derived linear systems according to the numerical scheme that is used.

Numerical Scheme	Linear System of Equations
Forward Euler	$\mathbf{C}^{n+1} = (\mathbf{I} + \Delta T \mathbf{A}) \mathbf{C}^n + \Delta T \cdot F(\mathbf{C}^n)$
Backward Euler	$(\mathbf{I} - \Delta T \mathbf{A}) \mathbf{C}^{n+1} - \Delta T \cdot F(\mathbf{C}^{n+1}) = \mathbf{C}^n$
θ -Methods	$(\mathbf{I} - \theta \Delta T \mathbf{A}) \mathbf{C}^{n+1} - \theta \Delta T F(\mathbf{C}^{n+1}) = (\mathbf{I} + (1 - \theta) \Delta T \mathbf{A}) \mathbf{C}^n + (1 - \theta) \Delta T F(\mathbf{C}^n)$
Crank Nikolson	$\left(\mathbf{I} - \frac{1}{2} \Delta T \mathbf{A}\right) \mathbf{C}^{n+1} - \frac{1}{2} \Delta T F(\mathbf{C}^{n+1}) = \left(\mathbf{I} + \frac{1}{2} \Delta T \mathbf{A}\right) \mathbf{C}^n + \frac{1}{2} \Delta T F(\mathbf{C}^n)$

Table 3 - Direct expressions of the iterative linear system that are used for solving Eq. 21.

4. Implementation

After having acquired the mathematical formalism of the linear system that solves Eq. 21 we are ready to describe an approach of the model implementation in 3D. This approach has been already been implemented in C++ and the author can be contacted for more information or more code sharing. This section describes the steps of implementation.

4.1. Grid Initialization

At first, we have to initialize the grid of the points, where finite differences are going to be applied. A visualization of this discrete 3D space is presented in Figure 30. Suppose that N_3 MRI images of $N_1 \times N_2$ pixels are initially available with local image information $I(x_1, x_2, x_3)$, $x_i \in \{0, \dots, N_i - 1\}$ and $i \in \{1, 2, 3\}$. Image information at each point (x_1, x_2, x_3) may include intensity, local diffusion tensor and the initial tumor cell concentration.

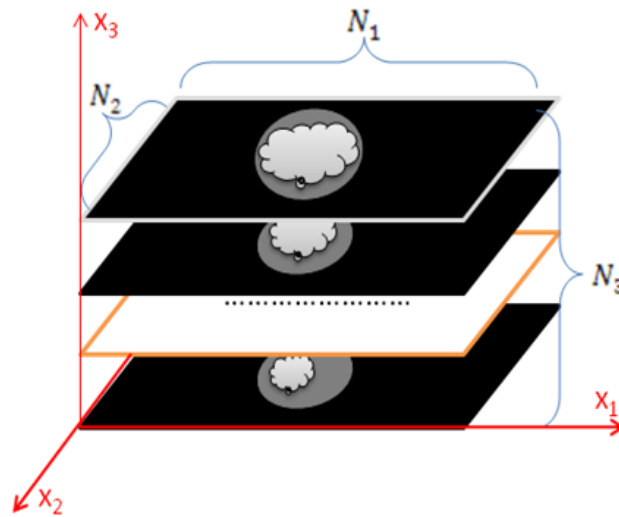


Figure 30 - A representation of a series of MRI images

Moreover, suppose that the distances between two consecutive points in direction of x_1 , x_2 and x_3 are physically interpreted to d_1 , d_2 and d_3 (mm) respectively within brain. One could directly use all the $N_1 N_2 N_3$ points of the initial brain space in the grid, so as to have more accurate results. However, by keeping all points on the grid, computational load and storage requirements increase. Oppositely, for instance, if one reduces the initial $N_1 \times N_2 \times N_3$ space to a $\frac{N_1}{2} \times \frac{N_2}{2} \times \frac{N_3}{2}$, then computational load and storage decrease to $\frac{1}{8}$. Thus, reducing initial data to less grid points (and sacrificing accuracy), is vital for the computational complexity of the model. In order to reduce the available data, one can sample local information I .

The initial $N_1 \times N_2 \times N_3$ grid can be sampled at every N_{S1} , N_{S2} and N_{S3} points, as Figure 31 shows. This is done by setting the sampled information as

$$I_S(x_1, x_2, x_3) \equiv I_S(N_{S1}x_1, N_{S2}x_2, N_{S3}x_3), x_i \in \left\{0, \dots, \left\lfloor \frac{N_i-1}{N_{Si}} \right\rfloor\right\} \quad 57$$

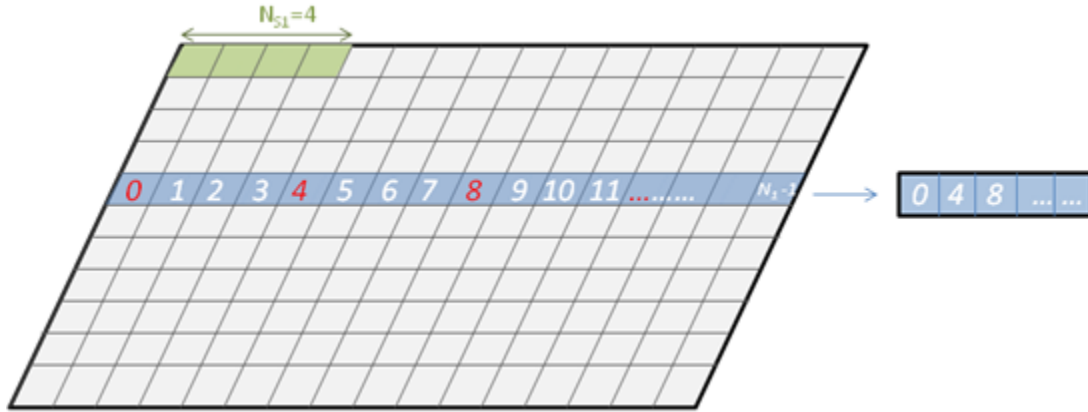


Figure 31 - Sampling of a MRI slice along the direction x , with $N_{S1} = 4$

Then, the new grid (Figure 32), on which the model will work on, has $N_x \times N_y \times N_z$ dimension, where:

$$N_x = \left\lfloor \frac{N_1}{N_{S1}} \right\rfloor, N_y = \left\lfloor \frac{N_2}{N_{S2}} \right\rfloor \text{ and } N_z = \left\lfloor \frac{N_3}{N_{S3}} \right\rfloor \quad 58$$

and the distance steps inside the brain are now

$$\Delta X = N_{S1} d_1, \Delta Y = N_{S2} d_2 \text{ and } \Delta Z = N_{S3} d_3. \quad 59$$

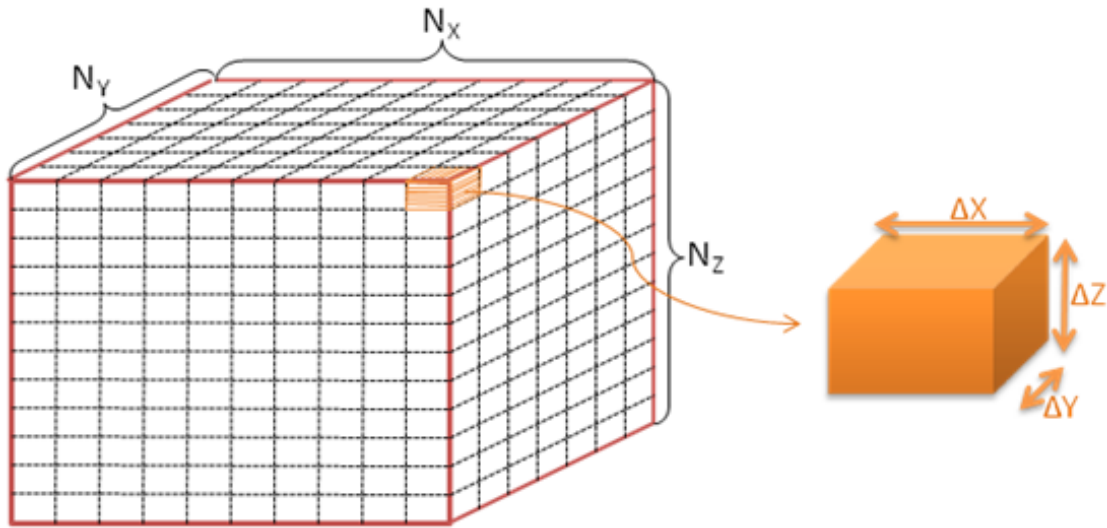


Figure 32 - The initialized grid and the dimensional interpretation to brain

4.2. Structures

This section presents a detailed formalism of the required structures for implementing the growth simulation program. Firstly, the information $I_S(x_1, x_2, x_3)$ of each point (x_1, x_2, x_3) is stored in a structure called `Point`. The structure can be implemented as shown in Figure 33 (left). `C_0` at iteration $n + 1$ is the concentration C_{x_1, x_2, x_3}^n , while `C_1` is C_{x_1, x_2, x_3}^{n+1} . `A[19]` is an array containing the 19 non-zero local values of matrix **A**, as estimated by Eq. 28. `is_boundary` is a boolean variable, expressing if boundary conditions apply at this point.

Finally, *intensity* is the local intensity of the medical image, while *D* is the 3x3 local diffusion tensor.

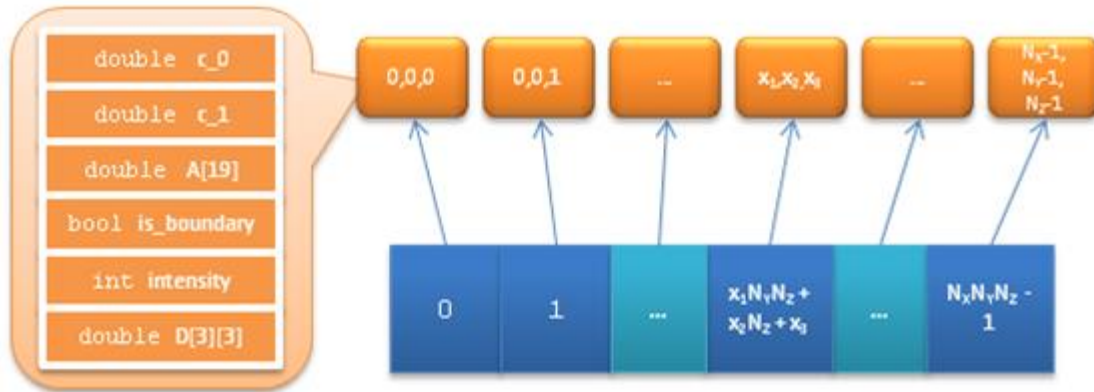


Figure 33 - (Left) Information structure Point for each point of the grid. (Right) The 1D array each position of which points to the information structure of the respective point.

One instance of this structure is associated with each point of the grid. Thus a 3D $N_X \times N_Y \times N_Z$ array of such structures should be used. Instead of using a 3D array, a $N_X N_Y N_Z$ row is used (Figure 33). The information structure for any point (x_1, x_2, x_3) , $x_1 \in \{0, \dots, N_X - 1\}$, $x_2 \in \{0, \dots, N_Y - 1\}$ and $x_3 \in \{0, \dots, N_Z - 1\}$ is pointed at the position $x_1 N_Y N_Z + x_2 N_Z + x_3$ of this 1D array.

Another structure that is used represents the matrix **A**. As already described, matrix **A** is a $N_X N_Y N_Z \times N_X N_Y N_Z$ 19-diagonal sparse matrix. Note that for a $128 \times 128 \times 128$ grid, the matrix has almost 4.4 quadrillion positions, only 40 million of which are non-zero. **A** cannot be stored in a compact format, since it is very large and it is surely inefficient to allocate storage for all elements. Obviously, some kind of indexed storage scheme is required. The scheme that is used is called row-indexed sparse storage mode and is well described in [98]. It requires about two times the number of nonzero matrix elements.

If $N = N_X N_Y N_Z$, then in order to represent the $N \times N$ matrix of the model, the scheme uses two 1D arrays, *sa* and *ija* with $19N$ locations. Array *sa* stores double values, while *ija* integers. The storage rules are:

- The first N locations of *sa* store **A**'s diagonal values, in order.
- Each of the first N locations of *ija* stores the index of the array *sa* that contains the first off-diagonal element of the corresponding row of the matrix. If there are no off-diagonal elements for that row, it is one greater than the index in *sa* of the most recently stored element of a previous row.
- Location 0 of *ija* is always equal to $N + 1$.
- Location N of *ija* is one greater than the index in *sa* of the last off-diagonal element of the last row.
- Entries in *ija* at locations $>N + 1$ contain **A**'s off-diagonal values, ordered by rows, and within each row, ordered by column.
- Entries in *sa* at locations $>N + 1$ contain the column number of the corresponding element in *sa*.

These rules result in an elegant storage scheme. As an example consider the matrix of Figure 34 (up). The row-indexed storage representation of this matrix is given in Figure 34 (down).

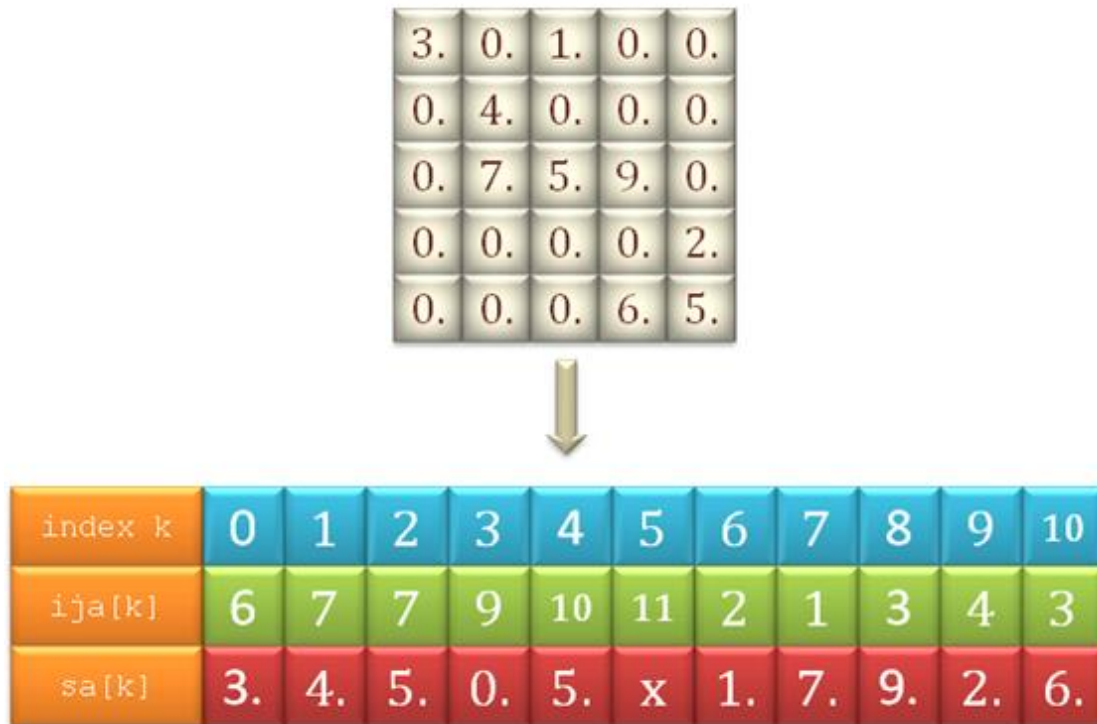
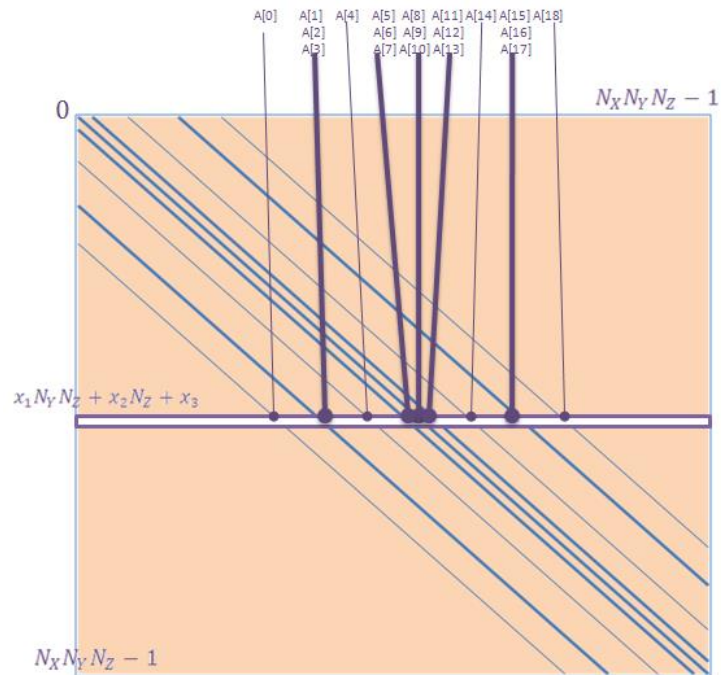


Figure 34 - (Up) Example of a 5x5 matrix. (Down) The representation of the row-indexed sparse matrix, after using the related rules.

4.3. Initialization of Structures

The first step of simulation is the initialization of the grid information. For each point of the grid, the relevant information structure is loaded. Initial concentration C_0 , intensity, the diffusion tensor D and the boundary conditions at each point are loaded from file. C_1 and $A[19]$ are initialized with zero values.

After having loaded the information for all grid points, $A[19]$ is calculated for each point using Eq. 28. As explained earlier, $A[19]$ for a point (x_1, x_2, x_3) represents the 19 nonzero elements of the $(x_1 N_y N_z + x_2 N_z + x_3)$ -th row of matrix A (see Figure 35). Thus, at this point, the row-indexed version of A , can be created by using the rules of the preceding paragraph. In our model, a slightly modified version of the C function described in [98] was used, in order to create the row-indexed scheme. The function is called `sprsin` and its code is given in Code 1.

Figure 35 - 19 A[] values for the grid point (x₁,x₂,x₃).

```

void sprsin(Point *a, double thresh, double *sA, unsigned long *ijA)
{
    //a:           the information struct of figure 4.1 (Left)
    //thresh:      Each A element with value <than thresh is truncated
    //N1N2N3:     the global variable for the product NX*NY*NZ
    int m,n,k;
    int nmax=19*N1N2N3;
    //Store diagonal elements
    for (m=0;m<N1N2N3;m++)
        sA[m]=A(a,m,m);
    //Store the first off diagonal element
    ijA[0]=N1N2N3+1;
    k=N1N2N3;
    //Start loop
    for (m=0;m<N1N2N3;m++)
    {
        //Choose only n's that are within matrix dimensions
        for (int i=0;i<19;i++)
        {
            n=n_est(m,i);
            if(m!=n && n>=0 && n<N1N2N3)
            {
                if(fabs(A(a,m,n))>=thresh)
                {
                    if (++k>nmax)
                    {
                        fprintf(stderr,"sprsin: sa, ija small");
                        exit(-1);
                    }
                    sA[k]=A(a,m,n);
                    ijA[k]=n;
                }
            }
        }
        ijA[m+1]=k+1;
    }
}
int n_est(int m, int index) //See 3.23
{
    switch(index)
    {
        case 9:
            return m;
        case 16:

```

```

        return m+N2N3;
    case 2:
        return m-N2N3;
    case 12:
        return m+N3;
    case 6:
        return m-N3;
    case 10:
        return m+1;
    case 8:
        return m-1;
    case 18:
        return m+N2N3+N3;
    case 0:
        return m-N2N3-N3;
    case 14:
        return m+N2N3-N3;
    case 4:
        return m-N2N3+N3;
    case 17:
        return m+N2N3+1;
    case 1:
        return m-N2N3-1;
    case 15:
        return m+N2N3-1;
    case 3:
        return m-N2N3+1;
    case 13:
        return m+N3+1;
    case 5:
        return m-N3-1;
    case 11:
        return m+N3-1;
    case 7:
        return m-N3+1;
    }
    return 0;
}
double A(Point *Volume, int m, int n) //Returns Amn (See 3.23)
{
    //Check if n,m are within limits
    if(n<0 || n>=N1N2N3 || m<0 || m>=N1N2N3)
    {
        fprintf(stderr, "Error: Tried to access A with invalid indeces.");
        exit(-1);
    }
    if(n==m)
        return (Volume[m].A[9]);
    if(n==m+N2N3)
        return (Volume[m].A[16]);
    if(n==m-N2*N3)
        return (Volume[m].A[2]);
    if(n==m+N3)
        return (Volume[m].A[12]);
    if(n==m-N3)
        return (Volume[m].A[6]);
    if(n==m+1)
        return (Volume[m].A[10]);
    if(n==m-1)
        return (Volume[m].A[8]);
    if(n==m+N2*N3+N3 || n==m-N2*N3-N3)
        return (Volume[m].A[18]);
    if(n==m+N2*N3-N3 || n==m-N2*N3+N3)
        return (-Volume[m].A[18]);
    if(n==m+N2*N3+1 || n==m-N2*N3-1)
        return (Volume[m].A[17]);
    if(n==m+N2*N3-1 || n==m-N2*N3+1)
        return (-Volume[m].A[17]);
    if(n==m+N3+1 || n==m-N3-1)
        return (Volume[m].A[13]);
    if(n==m+N3-1 || n==m-N3+1)
        return (-Volume[m].A[13]);
    return(0);
}

```

Code 1- Function sprsin() that creates the row-indexed representation of a matrix and its subroutines

4.4. Solving the Linear system

Continuing, after having stored the big sparse matrix \mathbf{A} , using `sprsin()`, the next step is to create the linear system that is going to be solved numerically. Suppose that the net proliferation rate is geometric. Then Eq. 41, Eq. 44 and Eq. 47 become

$$\mathbf{C}^{n+1} = ((1 + \rho\Delta T)\mathbf{I} + \Delta T\mathbf{A})\mathbf{C}^n \quad 60$$

$$((1 - \rho\Delta T)\mathbf{I} - \Delta T\mathbf{A})\mathbf{C}^{n+1} = \mathbf{C}^n \quad 61$$

and

$$((1 - \rho\theta\Delta T)\mathbf{I} - \theta\Delta T\mathbf{A})\mathbf{C}^{n+1} = ((1 + (1 - \theta)\rho\Delta T)\mathbf{I} + (1 - \theta)\Delta T\mathbf{A})\mathbf{C}^n \quad 62$$

Similarly, we work for other net proliferation schemes of $f(c)$.

4.4.1. Forward Euler

In order to create and solve Eq. 60, matrix \mathbf{A} has to be initially multiplied by ΔT . After this, $(1 + \rho\Delta T)$ should be added to each diagonal of $\Delta T\mathbf{A}$. In order to achieve this using the sparse array representation, we use the following two functions of Code 2.

```
void sprsl(double L, double *sA, unsigned long *ija)
{
    //Multiply sparse matrix A with the number L
    for (int i=0; i<ija[ija[0]-1]; i++)
    {
        sA[i]=L*sA[i];
    }
}

void sprsI(double lamda, double *sA, unsigned long *ija)
{
    //Compute A+λI
    for (int i=0; i<ija[0]-1; i++)
        sA[i]=lamda+sA[i];
}
```

Code 2 - Functions `sprsl()` and `sprslI()`

Thus, by using the two functions of Code 1, $((1 + \rho\Delta T)\mathbf{I} + \Delta T\mathbf{A})$ of Eq. 60 can be computed. In order to achieve this, the functions are called as

```
sprsl(ΔT, sa, ija);
sprsI(1+ΔT*ρ, sa, ija);
```

The next step is to iteratively solve the system. In order to be able to resolve this, two $1 \times N_x N_y N_z$ vectors \mathbf{C}^n and \mathbf{C}^{n+1} have to be allocated. After this, the vector \mathbf{C}^n has to be initialized. When the first iteration is met (i.e. $n = 0$) \mathbf{C}^n is initialized by setting its values equal to the initial concentration \mathbf{C}^0 . For $n > 0$, \mathbf{C}^n is initialized by setting this equal to the previous state concentration \mathbf{C}^{n-1} (i.e. \mathbf{C}^{n+1} of the previous state).

At each iteration, \mathbf{C}^{n+1} is approximated by just calculating the product of matrix $((1 + \rho\Delta T)\mathbf{I} + \Delta T\mathbf{A})$ by \mathbf{C}^n . In order to do that we use function `sprax()`, the implementation of which is presented in Code 3. This is called as `spr sax(Cn, Cn+1, sa, ija)`.

```

void sprsax(double *x, double *b, double *sA, unsigned long *ija)
{
    //Computes Ax=b (b is unknown)
    int i,k;

    if (ija[0] != N1N2N3+1)
    {
        fprintf(stderr,"sprsax: mismatched vector and matrix");
        exit(-1);
    }
    for (i=0;i<ija[0]-1;i++)
    {
        b[i]=sA[i]*x[i];
        for(k=ija[i];k<ija[i+1];k++)
        {
            b[i] += sA[k]*x[ija[k]];
        }
    }
}

```

Code 3 - Function sprsax that estimates $b=Ax$

By using all these function, the eventual implementation of forward Euler scheme can be summarized in the following code.

```

void ForwardEuler(Point *Volume,unsigned int days, double DT, double *sa, unsigned
long *ija) //DT is ΔT (in days)
//days is the total simulation time
{
    //Declarations
    ...
    double *Cn;
    double *Cn_plus_1; //Cn+1
    //Create Sparse matrix ((1+ρΔT)I+ΔT*A)
    sprsin(Volume, 0, sa, ija); //A
    sprsl(DT, sa, ija); //Multiply by ΔT
    sprsI(1+DT*r,sa, ija); //Add (1+ΔT*ρ)I
    //Allocate memory for vector C and Cn+1
    Cn..., Cn_plus_1 ...
    //Initialize Cn and Cn+1
    for(int i=0;i<N1N2N3;i++)
    {
        Cn[i]=Volume[i].concentration[0]; // Cn=C0
        Cn_plus_1[i]=0;
    }
    //Start iterations
    for(t=0; t< int (days/DT); t++)
    {
        sprsax(Cn,Cn_plus_1,sa,ija); //Solve ((1+ρΔT)I+ΔT*A)*Cn=Cn+1}
        //Update values of Cn, for the next iteration
        for(int i=0;i<N1N2N3;i++)
            Cn[i]=Cn_plus_1[i];
    }
    //Here, C_plus_1 is the approximated concentration at time n=days
    ...Use/return C_plus_1
    //Deallocate memory
    Free...
}

```

Code 4 - Implementation of the forward Euler scheme

4.4.2. Backward Euler

We work similarly for deriving the system of the backward Euler scheme; however an iterative method has to be used here for solving the system. Firstly, $((1 - \rho\Delta T)\mathbf{I} - \Delta T\mathbf{A})$ of Eq. 61 is created by calling

```

sprsl(-DT, sa, ija); //Multiply by -DT (-ΔT*A)

sprsI(1-DT*r,sa, ija); //Add (1-ρΔT)I

```

The next step is to iteratively solve the system. As in forward Euler, two $1 \times N_x N_y N_z$ vectors C^n and C^{n+1} have to be used. At each iteration the emerging system is solved by using the iterative biconjugate gradient method for sparse matrices that is provided in [98]. The code for implementing the biconjugate gradient method is given in Code 5.

```

void linbcg(double *b, double *x, const int itol, const double tol, const int itmax ,
double *sa, unsigned long *ija)
{
/*Solves Ax=b by iterative conjugate gradient method (x is unknown). x should be set
to an initial guess of the solution, 0 otherwise. itol is 1,2,3 or 4 (see [98]), itmax
is the maximum number of iterations, tol is the desired convergence tolerance.*/

double err,ak,akden,bk,bkden=1.0,bknum,bnrm,dxnrm,xnrm,zmlnrm,znrm;
const double EPS=1.0e-14;
int j, iter;

int n=N1N2N3;

double *p,*pp,*r,*rr,*z,*zz;
//Allocate memory for p, pp, r, rr, z and zz
p = (double *)malloc(N1N2N3*sizeof(double));
pp = (double *)malloc(N1N2N3*sizeof(double));
r = (double *)malloc(N1N2N3*sizeof(double));
rr = (double *)malloc(N1N2N3*sizeof(double));
z = (double *)malloc(N1N2N3*sizeof(double));
zz = (double *)malloc(N1N2N3*sizeof(double));
//

iter=0;
atimes(x,r,0,sa,ija);
for (j=0;j<n;j++) {
r[j]=b[j]-r[j];
rr[j]=r[j];
}
if (itol == 1) {
bnrm=snrm(b,itol);
asolve(r,z,0, sa, ija);
}
else if (itol == 2) {
asolve(b,z,0, sa, ija);
bnrm=snrm(z,itol);
asolve(r,z,0, sa, ija);
}
else if (itol == 3 || itol == 4) {
asolve(b,z,0, sa, ija);
bnrm=snrm(z,itol);
asolve(r,z,0, sa, ija);
znrm=snrm(z,itol);
} else fprintf(stderr,"illegal itol in linbcg");
//cout << fixed << setprecision(6);
while (iter < itmax) {
++iter;
asolve(rr,zz,1, sa, ija);
for (bknum=0.0,j=0;j<n;j++) bknum += z[j]*rr[j];
if (iter == 1) {
for (j=0;j<n;j++) {
p[j]=z[j];
pp[j]=zz[j];
}
} else {
bk=bknum/bkden;
for (j=0;j<n;j++) {
p[j]=bk*p[j]+z[j];
pp[j]=bk*pp[j]+zz[j];
}
}
bkden=bknum;
atimes(p,z,0, sa, ija);
for (akden=0.0,j=0;j<n;j++) akden += z[j]*pp[j];
ak=bknum/akden;
atimes(pp,zz,1, sa, ija);
for (j=0;j<n;j++) {
x[j] += ak*p[j];
}
}
}

```

```

        r[j] -= ak*z[j];
        rr[j] -= ak*zz[j];
    }
    asolve(r,z,0, sa, ija);
    if (itol == 1)
        err=snrm(r,itol)/bnrm;
    else if (itol == 2)
        err=snrm(z,itol)/bnrm;
    else if (itol == 3 || itol == 4) {
        zmlnrm=znrn;
        znrn=snrm(z,itol);
        if (fabs(zmlnrm-znrn) > EPS*znrn) {
            dxnrm=fabs(ak)*snrm(p,itol);
            err=znrn/fabs(zmlnrm-znrn)*dxnrm;
        } else {
            err=znrn/bnrm;
            continue;
        }
        xnrn=snrm(x,itol);
        if (err <= 0.5*xnrn) err /= xnrn;
    } else {
        err=znrn/bnrm;
        continue;
    }
}
//cout << "iter=" << setw(4) << iter+1 << setw(12) << err << endl;
if (err <= tol) break;
}

//Free memory
free(p); p=NULL;
free(pp); pp=NULL;
free(r); r=NULL;
free(rr); rr=NULL;
free(z); z=NULL;
free(zz); zz=NULL;
//
}
void atimes(double *x, double *r, const int itrnsp, double *sa_p, unsigned long
*ija_p)
{
    if (itrnsp) sprstx(sa_p,ija_p,x,r);
    else sprsax(x,r,sa_p,ija_p);
}
double snrm(double *sx, const int itol)
{
    int i,isamax;
    double ans;

    int n=N1N2N3;
    if (itol <= 3) {
        ans = 0.0;
        for (i=0;i<n;i++) ans += sx[i]*sx[i];
        return sqrt(ans);
    } else {
        isamax=0;
        for (i=0;i<n;i++) {
            if (fabs(sx[i]) > fabs(sx[isamax])) isamax=i;
        }
        return fabs(sx[isamax]);
    }
}
void asolve(double *b, double *x, const int itrnsp, double *sa_p, unsigned long
*ija_p)
{
    int i;

    int n=N1N2N3;
    for(i=0;i<n;i++) x[i]=(sa_p[i] != 0.0 ? b[i]/sa_p[i] : b[i]);
}
void sprstx(double *sa, unsigned long *ija, double *x, double *b)
{
    int i,j,k;

    int n=N1N2N3;
    if (ija[0] != (n+1))

```

```

        fprintf(stderr, "mismatched vector and matrix in sprstx");
    for (i=0; i<n; i++) b[i]=sa[i]*x[i];
    for (i=0; i<n; i++) {
        for (k=ija[i]; k<ija[i+1]; k++) {
            j=ija[k];
            b[j] += sa[k]*x[i];
        }
    }
}

```

Code 5 - Function linbcg that solves $Ax=b$ and its subroutines

By using all these functions, the eventual implementation of backward Euler scheme, is the same with that of Code 4, with just altering line `spr sax(Cn, Cn_plus_1, sa, ija);` to `linbcg(Cn, Cn_plus_1, ITOL, TOL, ITMAX, sa, ija);`

4.4.3. θ -methods

Continuing, the implementation of the solution of Eq. 62 is presented. Note that the forward part, i.e. $((1 - \rho\theta\Delta T)\mathbf{I} - \theta\Delta T\mathbf{A})$ and the backward part, i.e. $((1 + (1 - \theta)\rho\Delta T)\mathbf{I} + (1 - \theta)\Delta T\mathbf{A})$ use the same \mathbf{A} matrix. Thus, one more row-indexed sparse matrix is necessary, for representing both sides of the equation. The implementation of θ -method is given in Code 6.

```

void theta(Point *Volume, unsigned int days, double DT, double *sa, unsigned long *ija,
double *sa2, unsigned long *ija2, double th)
//DT is ΔT (in days)
//days is the total simulation time
//sa2 and ija2 implement the 2nd sparse array.
//th is θ in [0,1]. Crank Nikolson scheme is applied for θ=0.5
{
    //Declarations
    ...
    double *B, Cn;
    double *Cn_plus_1; //Cn+1
    //Create Sparse matrix A1=((1+(1-θ)ρΔT)I+(1-θ)ΔT*A)
    sprsin(Volume, 0, sa, ija); //A
    sprsl((1-th)*DT, sa, ija); //Multiply by (1-θ)ΔT
    sprsI(1+(1-th)*DT*r, sa, ija); //Add (1+(1-θ)ρΔT)I
    //Create Sparse matrix A2=(1-θρΔT)I-θΔT*A)
    sprsin(Volume, 0, sa2, ija2); //A
    sprsl(-th*DT, sa2, ija2); //Multiply A by -θΔT
    sprsI(1-th*DT*r, sa2, ija2); //Add (1-θρΔT)I
    //Allocate memory for vector C and Cn+1
    Cn..., Cn_plus_1 ...
    //Initialize Cn and Cn+1
    for(int i=0; i<N1N2N3; i++)
    {
        Cn[i]=Volume[i].concentration[0]; // Cn=C0
        Cn_plus_1[i]=0;
    }
    for(t=0; t< int (days/DT); t++) //Start iterations
    {
        //Solve A2Cn+1=A1Cn

        sprsax(Cn, B, sa, ija); //Compute B=A1Cn=((1+(1-θ)ρΔT)I+(1-θ)ΔT*A)Cn
        linbcg(B, Cn_plus_1, ITOL, TOL, ITMAX, sa2, ija2); //Solve A2*Cn+1=B
        for(int i=0; i<N1N2N3; i++) //Update values of Cn, for the next iteration
            Cn[i]=Cn_plus_1[i];
    }
    //Here, C_plus_1 is the approximated concentration at time n=days
    ...Use/return C_plus_1
    //Deallocate memory
    Free...
}

```

Code 6 - Implementation of the θ -methods

5. Qualitative and Quantitative Analysis

After having derived the system of equations, iterative solution of which yields the approximated glioma cell concentration at a desired time, it is essential to evaluate the performance of the different numerical schemes that have been implemented (Forward, Backward Euler and θ -methods) [99]. As described earlier, due to spatial dependence of diffusion tensor \mathbf{D} , an analytical solution of Eq. 19 cannot be acquired, so it is impossible to mathematically compare the performance of each used scheme. Therefore, a simplified test case of the pure diffusion equation is used, for which there is a known analytical continuous expression of the solution:

$$\frac{\partial c}{\partial t} = \nabla \cdot (D \nabla c) \quad 63$$

Hence, the magnitude of each numerical scheme deviation from the real solution can be studied, which serves here as 'ground truth' for validating the different numerical approximations.

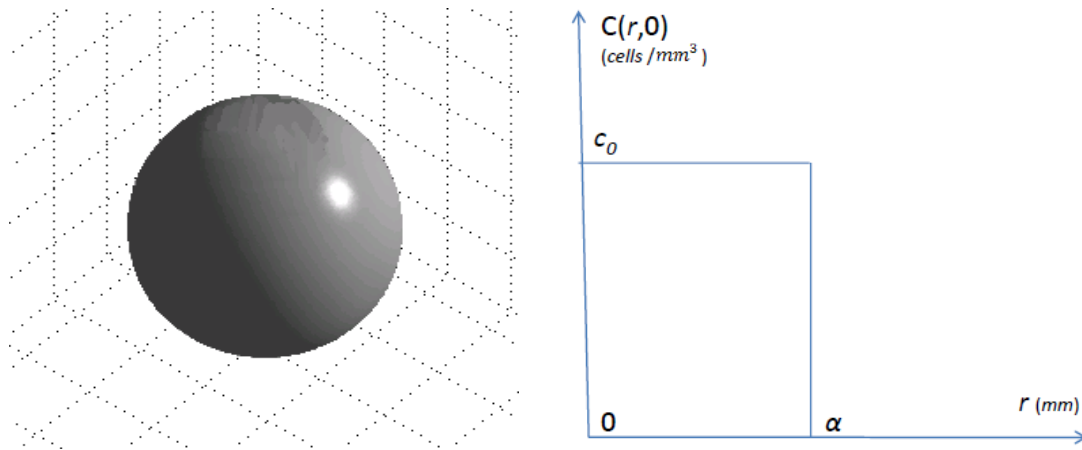


Figure 36- Left: The initial spherical tumor of radius α . Right: The tumor cell concentration according to r at time $t=0$

5.1. Pure diffusion modeling

To validate our methodology, it is assumed that tumor growth in 3 dimensional, homogeneous, unbounded and isotropic (i.e. D is constant) region and exhibits a pure diffusion behavior (i.e. Eq. 63 holds). The tumor has initially a concentration c_0 and it is constrained in a sphere of radius a (

Figure 36). Due to symmetry, the concentration of glioma cells depends only on the distance r from the center of the sphere (i.e. the distance from the center computed along the orange line of Figure 37) and it is given by the expression [100]:

$$C(r,t) = \frac{1}{2} c_0 \left(\operatorname{erf} \left(\frac{a-r}{2\sqrt{Dt}} \right) + \operatorname{erf} \left(\frac{a+r}{2\sqrt{Dt}} \right) \right) - \frac{c_0}{r} \sqrt{\frac{Dt}{\pi}} \left(\exp \left(-\frac{(a-r)^2}{4Dt} \right) - \exp \left(-\frac{(a+r)^2}{4Dt} \right) \right) \quad 64$$

where erf is the error function:

$$erf(x) = \frac{2}{\sqrt{\pi}} \int_0^x e^{-t^2} dt$$

The initial concentration $C(r, 0)$ is presented in Figure 36 (right). Thus, the solution of Eq. 63 can be approximated by the implemented numerical schemes, with Eq. 64 serving as ground truth for validating these approximations.

5.2. Testing and Simulation Description

In our tests, the model is adapted to approximate the solution of Eq. 63 by using the parameters that are presented in Table 4.

Parameter	Value	Unit
Growth rate	$f(c)$	0
Diffusion Tensor	D	$0,1 \times \begin{bmatrix} 1 & 0 & 0 \\ 0 & 1 & 0 \\ 0 & 0 & 1 \end{bmatrix}$
Initial tumour radius	a	10
Grid	$\Delta X = \Delta Y = \Delta Z$	1
Time Step	ΔT	12 (0.5)
Grid Resolution	$N_X \times N_Y \times N_Z$	$128 \times 128 \times 128$
Initial concentration	c_0	10^4
Simulation Days	T	1000

Table 4 – Model parameters for pure diffusion experiment

Five different simulations were run for 1000 fictitious days, using Forward Euler, three θ -methods for $\theta=0.25$, $\theta=0.5$ (Crank Nikolson) and $\theta=0.75$, and Backward Euler performed on a Pentium 4 at 3.8 GHz with 4GB RAM.

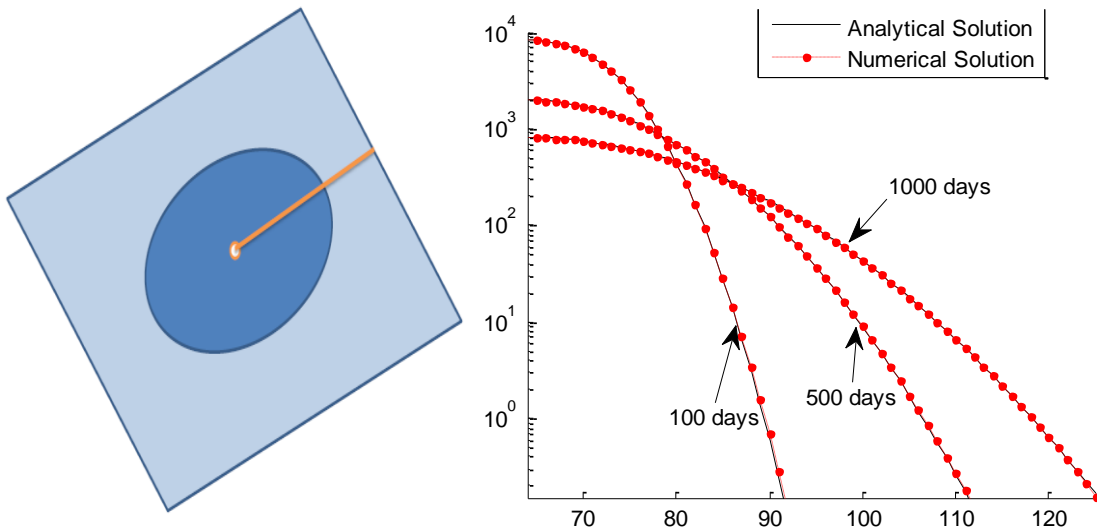


Figure 37 - Left: with orange: The direction on the central slice of the grid ($N_Z/2$) along which the concentration is sampled. Right: The evolution of $C(r)$ after 100th, 500th and 1000th day. Dots are the approximations of $C(r)$ with the Crank Nikolson scheme.

Figure 37 presents the evolution of cell concentration in time, with respect to r , with lines corresponding to results from analytical expression of Eq. 64, while dots representing what simulation with Crank Nikolson yields. This figure shows a very good agreement between

these results; however a more rigorous investigation would require an error estimation analysis.■

When designing a model, engineers should not ignore the computational limitations of the model. The processing power and storage capacity of the computers that are used in clinical practice should be seriously taken into account, since a resource-demanding model would turn out to be cumbersome when no access to supercomputers is possible. This chapter stresses the limitations and advantages of each modeling scheme and provides quantitative proof. Hence, engineers and bioinformaticians working with glioma models (or any model with similar diffusion – reaction behavior) could assess the limitations of the model that they are about to develop, especially for real clinical models. Therefore, even if one method (e.g. Finite Elements) would initially seem as the most accurate, this work indicates specific tradeoffs (such as simulation time, storage and computational needs) that can cause computational problems on the main-stream computers of hospitals and may alter the preference to this method.

5.3. Analysis on Finite Differences

Normalized mean absolute error

In order to estimate the error that each numerical scheme yields, the normalized mean absolute error e is introduced. Due to symmetry, e at a time $t = n\Delta T$ is computed as

$$e = \frac{1}{N} \sum_{i=1}^N \left| \frac{C(i\Delta X, n\Delta T) - C_{i, \frac{N}{2}, \frac{N}{2}}^n}{c_0} \right| \times 100\% \quad 66$$

Table 5 shows the estimated error for each scheme on day 100, 500 and 1000 of simulation. Moreover, the overall simulation times are also reported, with the forward Euler scheme being 6.5 times faster than the next faster scheme. The highest e for all five schemes is on day 100 while it decreases to values $\leq 0.5\%$ on the 1000th day. Forward Euler error is the lowest on the 100th day, i.e. 2.24%, but eventually overcomes all other schemes, reaching 0.50% on 1000th day. Backward Euler expresses the worst performance on early days, but eventually yields the best results of all schemes on day 1000, with $e=0.39\%$.

Numerical Scheme	100 days	500 days	1000 days	Simulation Time
Forward Euler ($\theta=0$)	2.24%	0.67%	0.50%	27'53"
θ -Methods ($\theta=0.25$)	2.32%	0.59%	0.48%	182'13"
Crank Nikolson	2.41%	0.51%	0.45%	190'01"
θ -Methods ($\theta=0.75$)	2.54%	0.46%	0.42%	205'16"
Backward Euler ($\theta=1$)	2.69%	0.48%	0.39%	226'11"

Table 5 - Mean absolute error and execution time for approximating Eq. 63 using various numerical schemes.

In order to make a better comparative study of the numerical schemes performance, Figure 38 presents the logarithmic graph of e in time for each scheme. It is noticeable that all schemes initially produce very high errors, with the best performance carried by forward Euler with $e = 12\%$. A possible explanation is that the initial concentration $C(r, 0)$ has an abrupt step descent at $r = 10mm$, as seen in Figure 36 (right). This makes the approximation of the local partial derivatives at the edge of this step erroneous for all schemes. However, as simulation continues, e tends to significantly decrease e for all schemes.

Continuing, one can observe that e decreases to values $< 1\%$ for all schemes on day 190, 203, 252, 287 and 308 for forward Euler, 0.25-method, Crank Nikolson, 0.75-method and backward Euler, respectively. Forward Euler error has the most descent till day 274, but later decreases smoothly and overcomes all other schemes. Generally, it is noticeable that the smoother one scheme decreases at start, the better performance it expresses at the end. Indeed, the backward Euler method starts with the smoothest decrease, but eventually yields the lowest error, at 0.39%. Moreover, one can observe that there is a decrease in e till day 270, 365, 451, 557 and 644 for forward Euler, 0.25-method, Crank Nikolson, 0.75-

method and backward Euler, respectively. After these days, error decreases very smoothly till all schemes acquire balancing values.

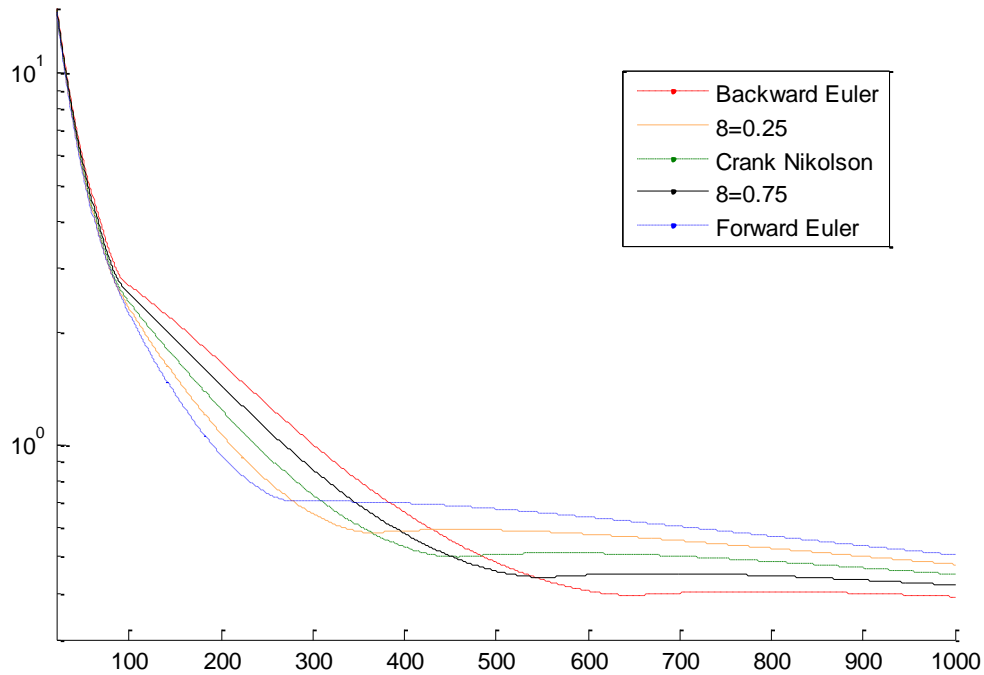


Figure 38- Mean absolute error for approximating Eq. 63 using different numerical schemes.

As a conclusion, the backward Euler method seems to yield the more accurate approximations of $C(r, t)$, but with the worst simulation times. If there is urgent need for faster simulations, one could use some faster models, such as the Crank Nikolson scheme, since the error is still below 0.45%. Similarly, if there is room for sacrificing accuracy for the fastest scheme, then the forward Euler scheme should be used, since it is 8.07 times faster than backward Euler. Even if one chooses the forward Euler, that is the worst case scenario, error e doesn't overcome 0.5%.

Effect of grid resolution

A very interesting study would be watching how accuracy is influenced by the change of $\Delta X, \Delta Y$ and ΔZ , i.e. the resolution of grid. We have used five different grid resolutions for approximating a pure-diffusion sphere of initial radius $a=10\text{mm}$ in a cubic space of $120 \times 120 \times 120 \text{mm}$.

Grid	Grid size ($N \times N \times N$)	$\Delta X = \Delta Y = \Delta Z$ (mm)	Sphere radius (pixels)	Simulation Time
1	120x120x120	1.0000	12.0000	65' 58"
2	60x60x60	2.0000	6.00000	7'26"
3	30x30x30	4.0000	3.00000	57"
4	15x15x15	8.0000	1.50000	7"
5	10x10x10	12.000	1.00000	2"

Table 6 - Grid and radius dimensions and simulation times for the experiment.

In Figure 39 the approximated (dots) and the real (line) values of concentration for the five different grids are presented. The model parameters are presented in Table 6. As expected,

as the grid resolution decreases (i.e. ΔX increases), the accuracy of approximation seems to decrease. For very low grid resolution, the simulation is highly erroneous.

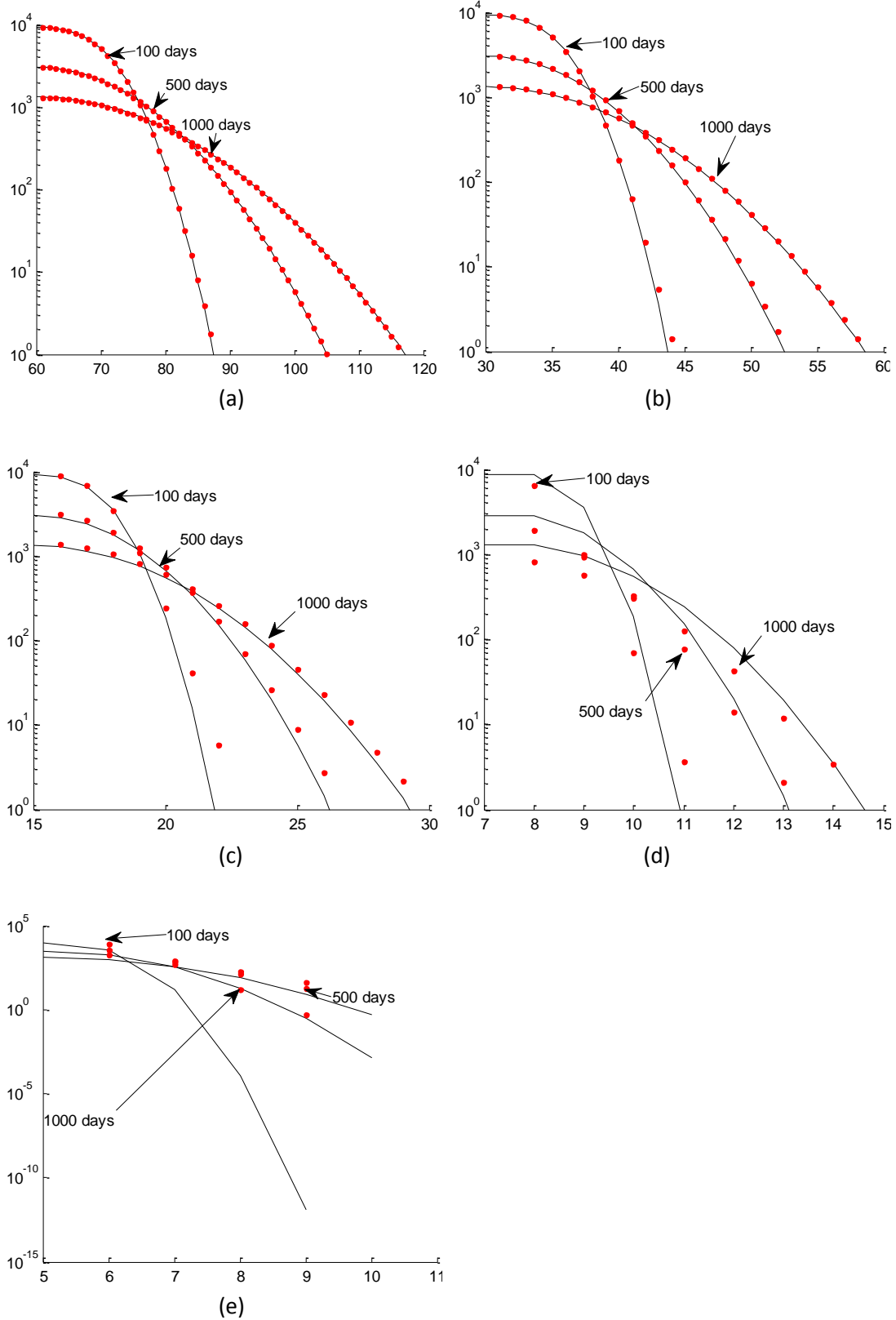


Figure 39 - (a, b, c, d, e) Approximation (red dots) of real solution (black line) taken in three moments for $\Delta X = \Delta Y = \Delta Z = 1, 2, 4, 8$ and 12 mm respectively

Continuing, we present how error e changes in time for the five different grids of our experiment. Figure 40 presents how error changes in time for the first day to the 1000th. We indeed see that the error is increasing as ΔX increases.

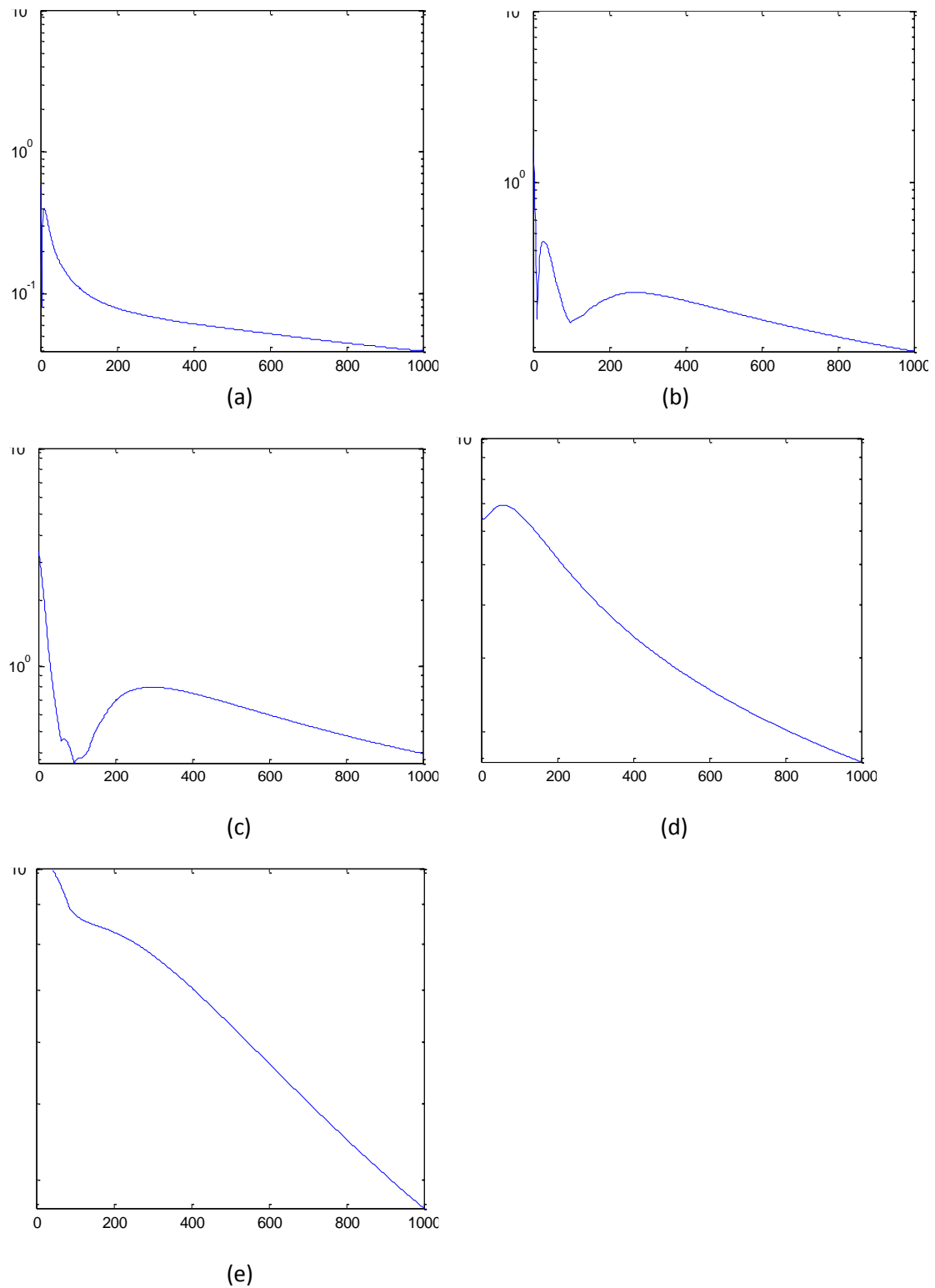


Figure 40 - (a, b, c, d, e) Error e taken in time for $\Delta X = \Delta Y = \Delta Z = 1, 2, 4, 8$ and 12 mm respectively

Lastly, all these errors are plotted in the same figure (Figure 41), in order to be easily comparable. As seen, the lowest e occurs for the smallest $\Delta X = 1$ mm and does not overcome

0.04%. However, as ΔX increases, error e increases. For $\Delta X=2, 4, 8$ and 12mm the lowest error is 0.10%, 0.39%, 1.69% and 3.67%.

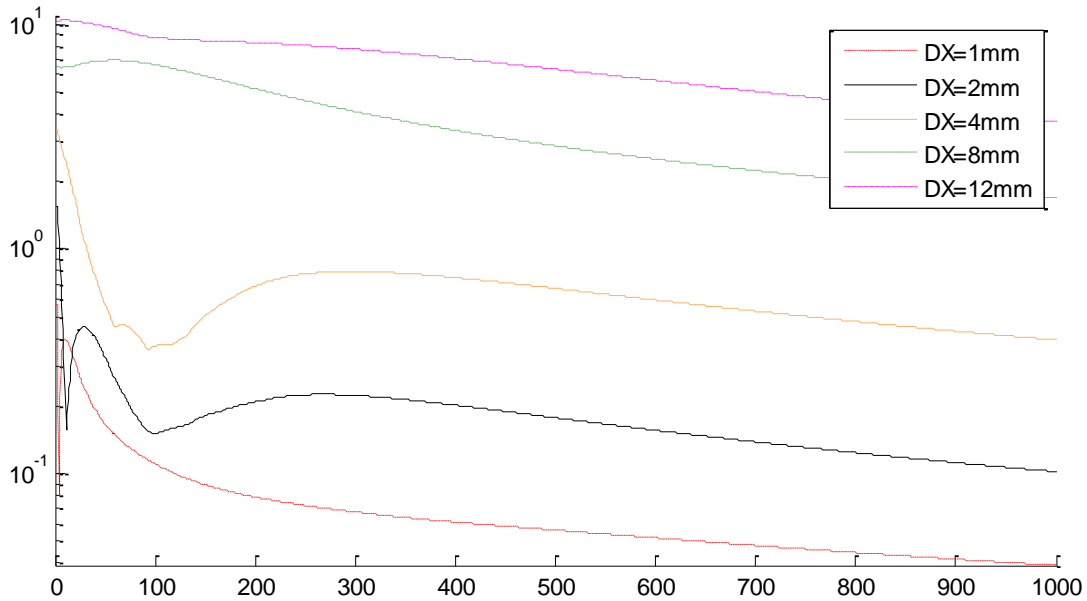


Figure 41- Error e in the first 1000 days for five different grids with $\Delta X=1, 2, 4, 8$ and 12mm .

Table 7 summarizes the error e in days 100, 500 and 1000, with the last column giving mean e . This is noteworthy to mention that halving of grid size from $120 \times 120 \times 120$ (grid-1) to $60 \times 60 \times 60$ (grid-2) yields a 157% increase in mean e and halving from $60 \times 60 \times 60$ (grid-2) to $30 \times 30 \times 30$ (grid-3) produces a 250% increase. However, halving of grid size $30 \times 30 \times 30$ (grid-3) to size $15 \times 15 \times 15$ (grid-4) results in a 453% increase in mean error. This means that the error rises rapidly as the grid size decreases.

Grid	Day 100	Day 500	Day 1000	Mean e
1	0.11%	0.06%	0.04%	0.07%
2	0.15%	0.18%	0.10%	0.18%
3	0.37%	0.69%	0.39%	0.63%
4	6.61%	2.88%	1.69%	3.49%
5	8.73%	6.31%	3.67%	6.44%

Table 7- Error e for the five different grids in day 100, 500 and 1000. The last column is the mean error e during these 1000 days.

Effect of time step

It is important to check the effect of time step ΔT in simulation accuracy. We have used three different numerical schemes (Forward Euler, Crank Nikolson and Backward Euler) in order to estimate the error e for approximating the concentration of cells for 1000 fictitious days of diffusion. The spatial steps $\Delta X, \Delta Y$ and ΔZ were set to 1mm and the experiments where run on a $60 \times 60 \times 60$ cubic grid and a sphere of 6mm.

Table 8 presents the mean error \bar{e} for the 1000 days of overall simulation. It is observed that the minimum \bar{e} is 0.0888%, performed by the Crank Nikolson scheme for $\Delta T = 2$ days.

Almost the same is the minimum \bar{e} for the cases for Forward Euler and Backward Euler methods, which are 0.79% and 1.01% higher than Crank Nikolson minimum, respectively. Someone could also notice that for $\Delta T = 0.001$ and $\Delta T = 0.01$, the errors for all schemes are the same. Especially for Forward Euler, this holds for ΔT values from 0.001 to 0.1. This indicates that there is a balancing value for ΔT under which no more accuracy can be achieved. This value of ΔT is around 0.1 for the Forward Euler method and around 0.01 for Crank Nikolson and Forward Euler methods.

Continuing, as expected, \bar{e} generally increases as ΔT increases, for all schemes. For Forward Euler, \bar{e} increases as ΔT increases, but when ΔT changes from 1 to 1.5 days, a slight decrease of 1.4% is observed. $\Delta T=1.5$ is the threshold, over which the model is unstable. For Backward Euler, \bar{e} generally increases smoothly as ΔT increases, with a small decrease of 3.38% from $\Delta T=0.5$ to 1 days. The error \bar{e} for the Crank Nikolson scheme shows a “basin” like behavior, since it starts at 0.0897% for $\Delta T=0.001$, rises smoothly to 0.0984% for $\Delta T=0.5$, falls at 0.0888% at $\Delta T=1$ and gradually increases from there.

Mean error e in the 1000 days of simulation			
ΔT (days)	\bar{e} for Forward Euler	\bar{e} for Backward Euler	\bar{e} for Crank Nikolson
0.001	0.0895%	0.0898%	0.0897%
0.01	0.0895%	0.0898%	0.0897%
0.05	0.0895%	0.0905%	0.0900%
0.1	0.0895%	0.0916%	0.0905%
0.5	0.0934%	0.1036%	0.0984%
1	0.0998%	0.1001%	0.0896%
1.5	0.0984%	0.1053%	0.0892%
2	<i>Instable</i>	0.1106%	0.0888%
3		0.1218%	0.0913%
4		0.1338%	0.0938%
5		0.1458%	0.0967%
50		0.7047%	1.5355%

Table 8 - Mean error \bar{e} for changing ΔT , using the Forward Euler, the Crank Nikolson and the Backward Euler numerical schemes.

As far as the performance of the three different schemes is concerned, one could say that the Crank Nikolson scheme shows the lowest \bar{e} for higher ΔT . Figure 42 presents the mean error \bar{e} according to ΔT for the three different schemes. It is interesting to note that Crank Nikolson scheme, for $\Delta T=4$, has almost the same accuracy with the respective case for $\Delta T=0.1$ of Backward Euler. Similarly, it has the same accuracy with the Forward Euler scheme for $\Delta T=0.5$. Thus a time step 40 times bigger than that of Backward Euler yields equivalent results. For lower time steps (around 0.1 days), Forward Euler yields the lowest \bar{e} , but simulation takes time. ■

By comparing different schemes of Finite Differences, we conclude that Explicit methods (Forward Euler) run faster, but are prone to errors. On the other hand, implicit methods (Backward Euler, Crank Nikolson, θ -methods) produce lower errors, but are computationally

greedy. Especially, Backward Euler has performed the most accurate approximation of the real solution, but also results in the worst simulation time. Moreover, the error increases rapidly as the grid resolution decreases. Finally, Forward Euler yields good approximation for small simulation time steps ΔT , but Crank Nikolson yields the low error for higher values of ΔT .

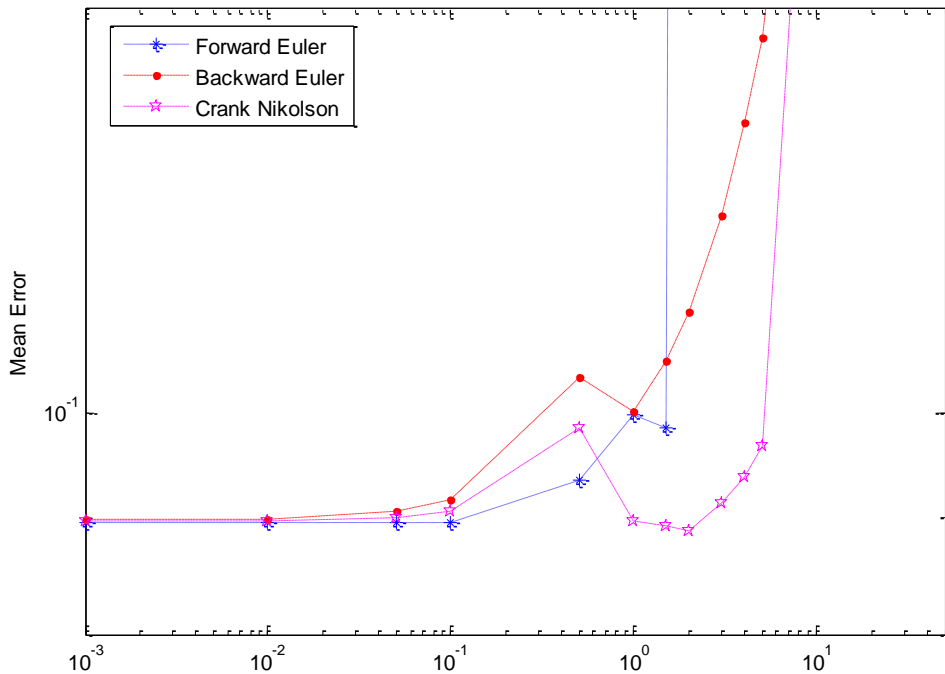


Figure 42- Mean error \bar{e} for changing ΔT , using the Forward Euler, the Crank Nikolson and the Backward Euler numerical schemes. The mean error has been calculated for 1000 days simulations.

5.4. Comparison with Finite Elements

The diffusive model has also been implemented with the Finite Element Method, using commercial software (COMSOL), in order to compare its efficiency to that of the Finite Differences model. The model uses tetrahedral Lagrange Quadratic Elements. Figure 43 presents an example of a meshed brain using Finite Elements with COMSOL.

Like Finite Differences, the solution requires the construction of a large sparse matrix, having its elements randomly located. Biconjugate gradient methods can be used for the solver, but the rate of convergence is slow and the quality of the approximate solution may be sensitive to roundoff errors [101]. Thus, there are limitations in the dimensions of the emerging sparse matrix.

Finite Elements and Finite Differences have been compared at approximating Eq. 64 on the same sphere presented earlier. Four different experiments have been performed for different grid resolutions, with the Finite Elements having used 125.000, 166.375, 216.000 and 343.000 elements, respectively. For the same experiments, Finite Differences have used the same number of cubic elements (voxels). When designing a model, developers should not ignore the computational limitations of the model. The process power and storage capacity of the computers that are used in clinical practice should be taken into account, since a resource-demanding model would turn out to be cumbersome when no access to

supercomputers is possible. The above comparison issues are elaborated in the following subsections.

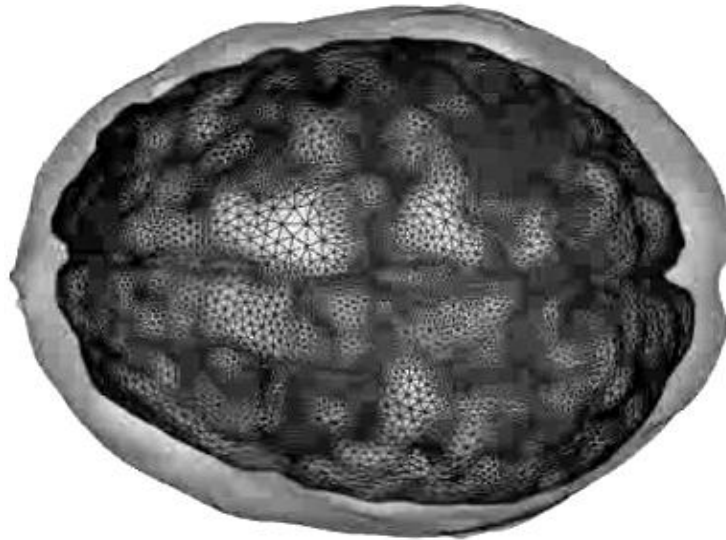


Figure 43 - An example of meshing 3-dimensional brain using COMSOL Lagrange Quadratic elements for mesh generation

Accuracy

The accuracy of the models has been studied, by estimating the deviation of the approximated solution $C_{appr}(r, t)$ from the real solution $C(r, t)$. The error E of the approximation at a distance r from the center of the sphere, is estimated as:

$$E(r) = |C_{appr}(r, t) - C(r, t)| \tag{67}$$

where t is set to 1000 days. The accuracy of the models is estimated by calculating the mean normalized error \bar{E} as follows:

$$\bar{E} = \frac{1}{\Delta} \int_{r=0}^{\Delta} E(r) \times 100\% \tag{68}$$

Table 9 presents the comparative results of approximating the pure diffusion equation with Lagrange Quadratic Finite Elements, Forward Euler, Crank Nikolson and Backward Euler. The first row presents the total number of elements of the mesh. The columns present the mean error of approximation at the 1000th day of diffusion simulation for each model.

Scheme	125.000	166.375	216.000	343.000
Finite Elements	2.97%	0.16%	0.06%	-
Backward Euler	2.99%	0.15%	0.06%	0.04%
Forward Euler	4.09%	0.21%	0.10%	0.08%
Crank Nikolson	3.16%	0.17%	0.08%	0.07%

Table 9- Error \bar{E} After 1000 Days For Different Grid Resolutions

In the first case (125.000 elements), Finite Elements achieved slightly lower error than that of Backward Euler and lower than Forward Euler. For 166.375 elements, Finite Elements produced higher error than Backward Euler and lower than Forward Euler. For 216.000 elements, Finite Elements produced the same error with Backward Euler and lower than Forward Euler. Lastly, for 343.000 elements, Finite Elements caused memory overflow and could not approximate the solution. On the other hand, Backward Euler produced the lowest error, at 0.04%.

Simulation Time

Table III presents the simulation time of each of the previous experiments, dependant on the grid resolution. It is observed that simulation time Finite Elements in the first experiment (125.000 elements) is 5.16 times higher than Backward Euler and 31 times higher than Finite Elements. In the second case, simulation time for Finite Elements is 2.8 times higher than Backward Euler and 52.69 times higher than Forward Euler. Lastly, in the third case, Finite Elements has 1.93 times higher simulation time than BE and 27.2 times higher than Finite Elements.

Scheme	125.000	166.375	216.000	343.000
Finite Elements	31"	20' 12"	151' 3"	-
Backward Euler	6"	7' 12"	78' 5"	210' 25"
Forward Euler	1"	23"	5' 32"	35' 48"
Crank Nikolson	6"	6' 59"	64' 1"	198' 12"

Table 10 – Simulation time for different grid resolutions

Storage and Computational Consistency

One important issue governing the comparison of the models that have been implemented with Finite Elements and Finite Differences, is their computational consistency. If the grid resolution of the mesh exceeds some limits, then the storage of the sparse matrix and the solving of the solution are practically impossible [98]. This is important, since a developer of such a system should bear in mind that clinicians may not have access to supercomputers or grid services, thus they have to adjust their products to realistic conditions.

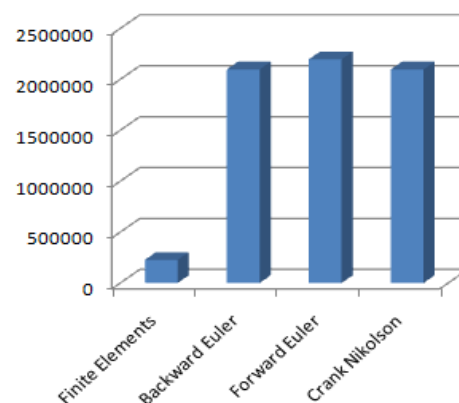


Figure 44 - The maximum number of elements, for which no memory overflow is performed

In this experiment, different grid resolutions have been used for approximating Eq. 64. Figure 44 presents the maximum element number that the computer can handle without memory overflow. As observed in the chart, Finite Elements Method “crashes” with total element number being almost 10% of the respective number of Finite Differences models. ■

Summary

By comparing Finite Differences with Finite Elements, it is observed that Finite Elements do not provide additional accuracy to the model. On the other hand, Finite Differences need less simulation time and extend the limitation of the total element number to almost 10 times more than the number of Finite Elements. This extends the accuracy potentials of Finite Differences into higher levels, because they can use higher resolution than Finite Elements.

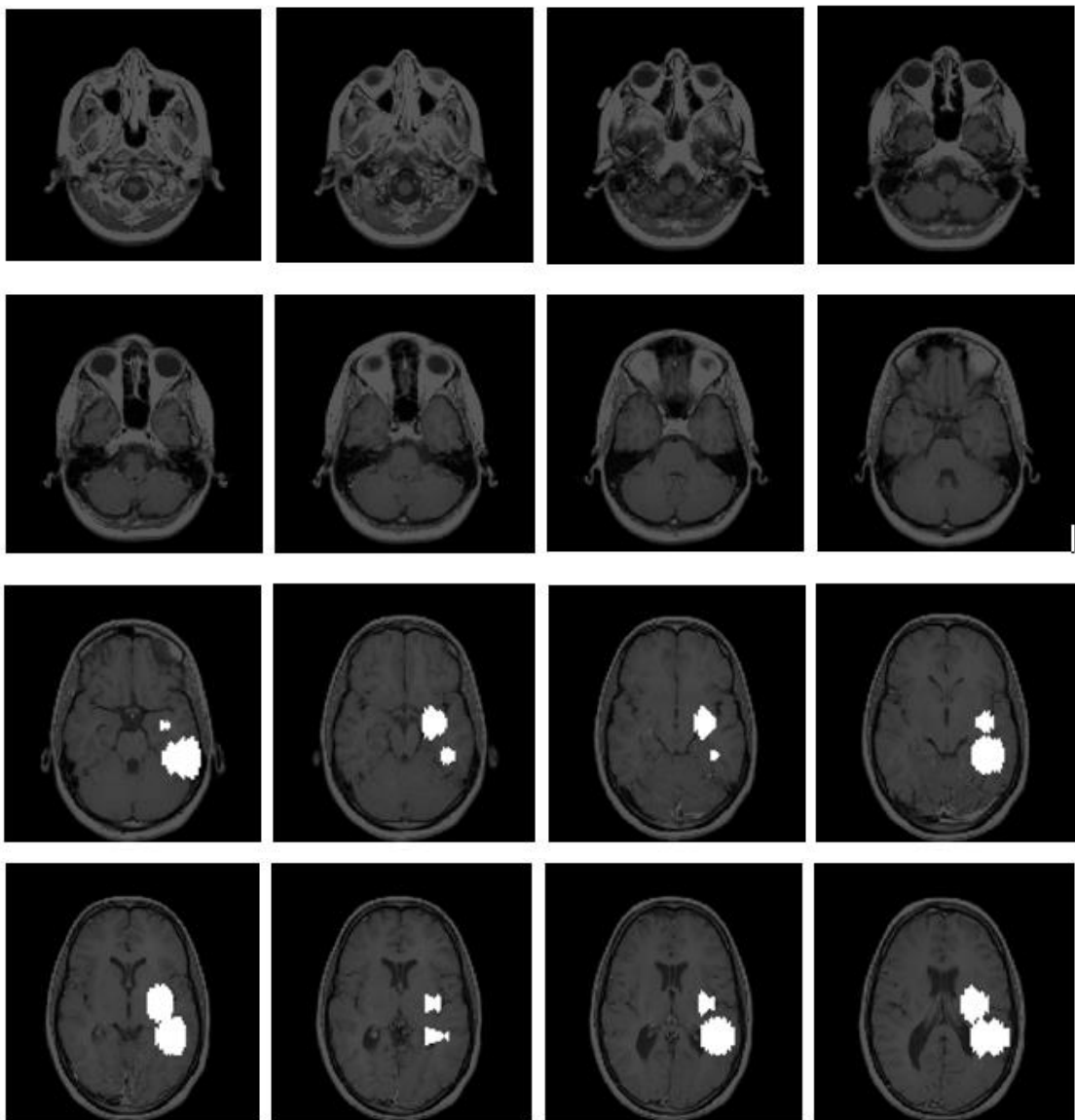
This analysis indicates that Finite Differences are practically more suitable for the needs of a glioma diffusive model. Therefore we select Finite Differences for further applying the model to real clinical cases.

6. Application on real tumors

According to the results of the previous chapter, we select Backward Euler for further applying the model to a real clinical case. Therefore all steps till the final result of simulation are presented. This chapter presents an example of model application.

6.1. Initial Patient Dataset

Figure 45 presents a series of 27 MRI slices of a 58 year old patient, taken from the Harvard Medical School database [102], with white areas reflecting glioblastoma multiforme, being delineated by a clinician. The patient passed away after 112 days and no therapy was applied, because of the advanced stage of the tumor at the time of diagnosis.



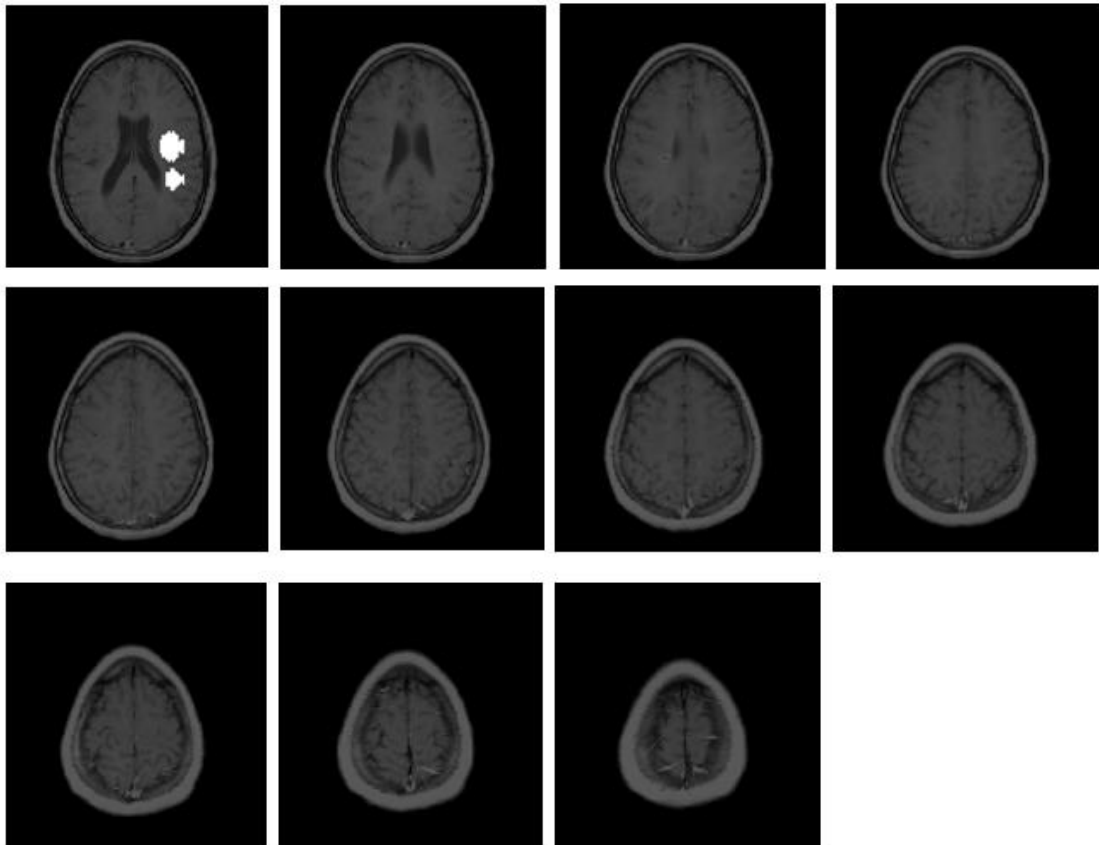


Figure 45 - 27 MRI slices taken from a patient with glioma at the first day that glioma was diagnosed in 17 April 2007 – The tumor areas have been defined with white color.

These slices have been interpolated and represented in 3 dimensions by using the Mathworks Matlab software (2010a). Figure 46 - Different angles of the 3D visualization of initial tumors, extracted from MRIs of Figure 45 depicts the representation of the tumor in the skull at the time of diagnosis taken from different angles, on which the model is applied.

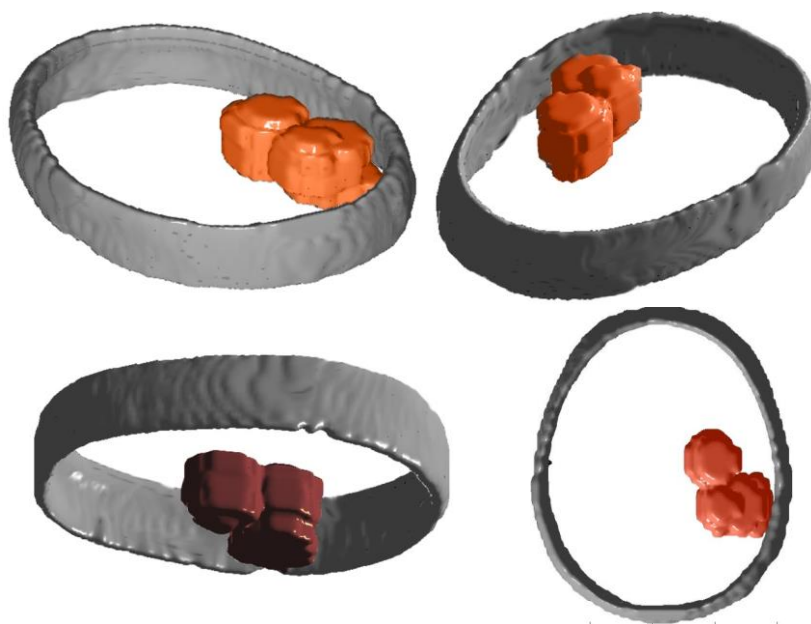


Figure 46 - Different angles of the 3D visualization of initial tumors, extracted from MRIs of Figure 45

6.2. Simulation Parameters

The glioma of the patient was classified to high-grade glioma, namely GBM. The geometrical proliferation rate ρ was set, according to Table 1, at $\rho = 0.012 \text{ day}^{-1}$. Moreover, $D_{ij}(\mathbf{x})$ was set to $w_i(\mathbf{x})D(\mathbf{x})$ for $i = j$ and zero otherwise, where $w_i(\mathbf{x}) \in [0,1]$ expresses the local anisotropic migration of cells along the direction i (x , y or z axis) and $D(\mathbf{x})$ is the local diffusion coefficient. $D(\mathbf{x})$ equals $D_g = 0.13 \text{ mm}^2/\text{day}$ when point \mathbf{x} is located in gray matter and $D_w = 0.65 \text{ mm}^2/\text{day}$ when in white matter. Furthermore, local anisotropy parameter $w_i(\mathbf{x})$ was estimated according to [103][104], the initial concentration was defined at 200 cells/mm^3 and the density threshold for detection at 400 cells/mm^3 . Lastly, the grid distances $\Delta X, \Delta Y$ and ΔZ were defined at 1 mm , 1 mm and 3 mm respectively, time step was defined at 0.5 days and overall simulation time at 112 days, when the patient passed away. Table 11 summarizes these parameters.

Parameter	Value		Unit
Proliferation scheme	<i>Geometrical</i>		—
Proliferation Rate	ρ	0.012	day^{-1}
Diffusion Coefficient in white matter	D_w	0.65	mm^2/day
Diffusion Coefficient in gray matter	D_g	0.13	mm^2/day
Initial concentration	c_0	200	cells/mm^3
Grid	ΔX	1	mm
	ΔY	1	
	ΔZ	3	
Time Step	ΔT	12 (0.5)	hours (days)
Simulation Days	T	112	Days
Detection Threshold	Th	400	cells/mm^3

Table 11- Simulation parameters

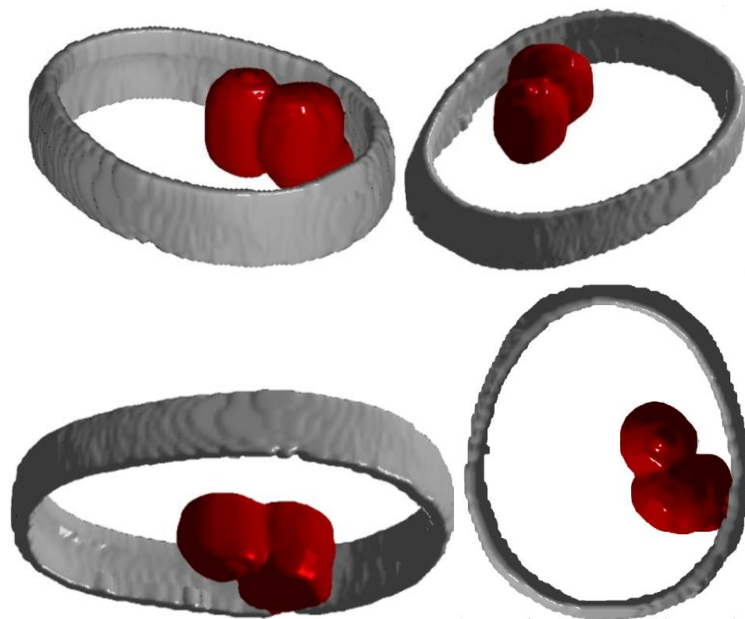


Figure 47 - Different angles of the 3D visualization of simulated tumor, after 112 fictitious days

6.3. Simulation Results

Figure 47 presents the produced result of the simulation of our model, after 112 days, after applying the detection threshold Th . The numerical method that has been used for the iterative solution of the diffusion equation is the Backward Euler scheme. Similarly, Figure 48 presents how these results are reconstructed back to MRI images (the first four are omitted).

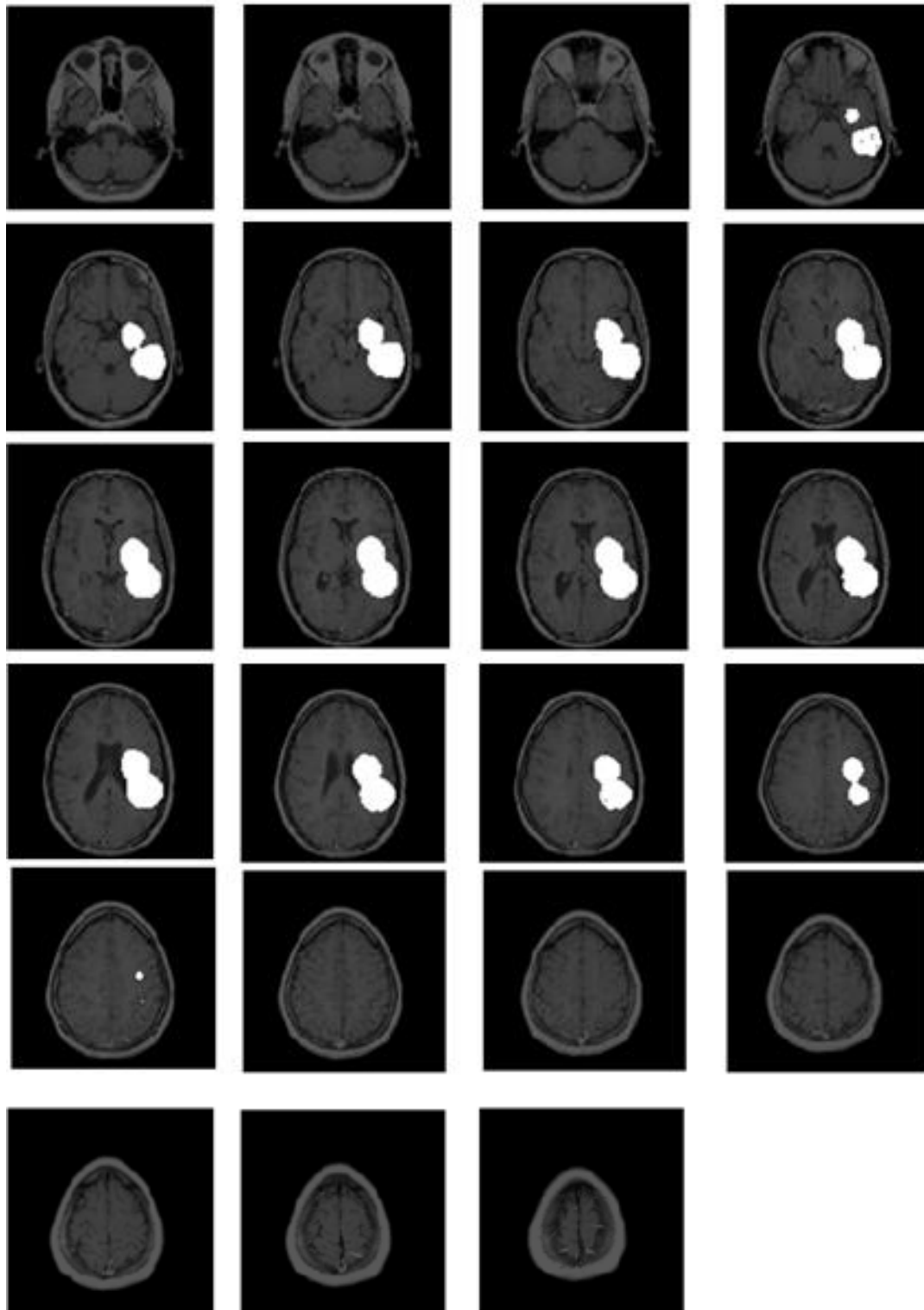


Figure 48 - Reconstructed MRI images for the simulated volume at the time of 112 days

6.4. Final Patient Dataset

Similarly, to initial dataset, Figure 49 presents the real final dataset at the time of death and Figure 50 presents its 3-dimensional representation. This will be used for cross validation of the simulation results.

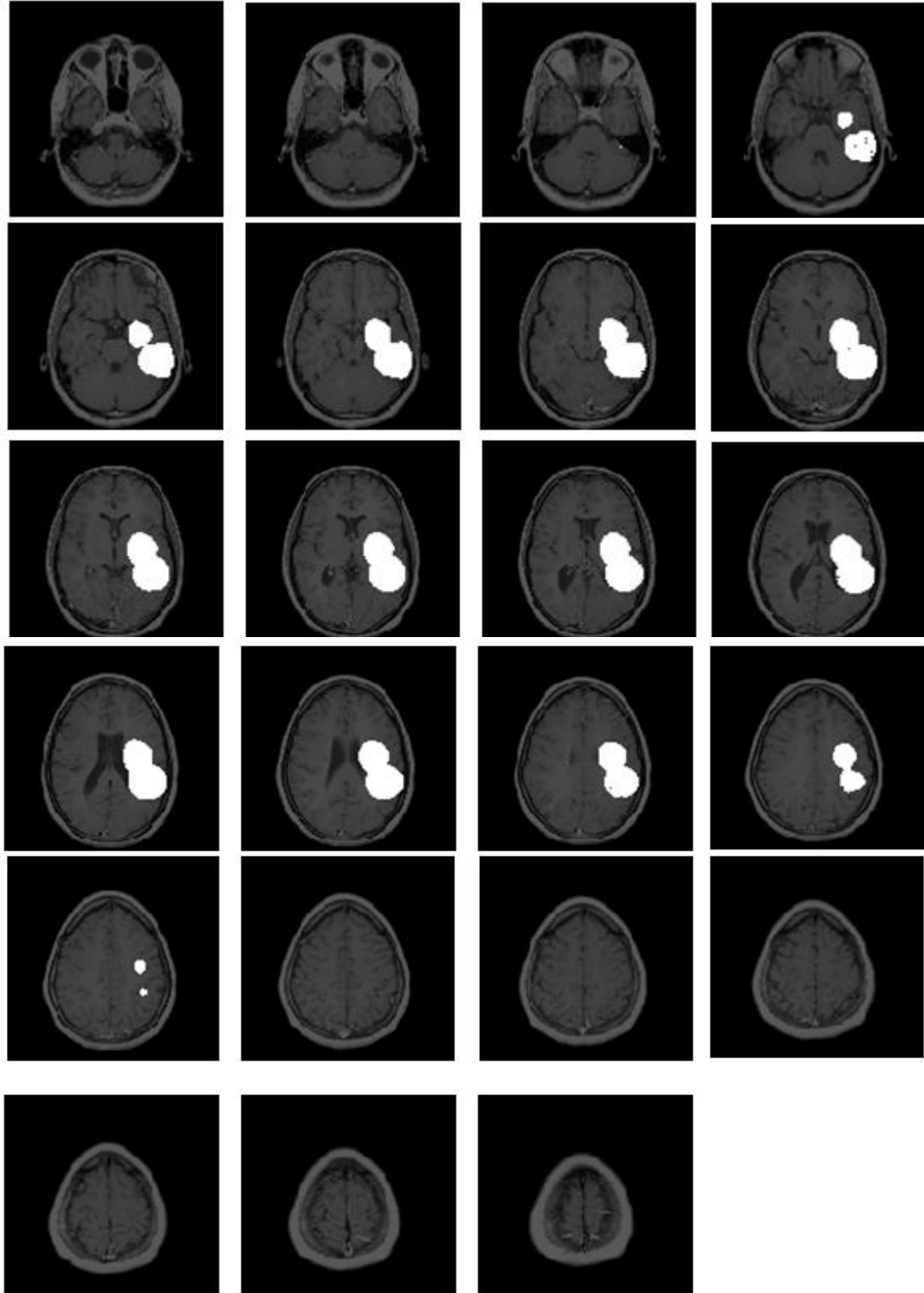


Figure 49 - Real MRI images at the time of death

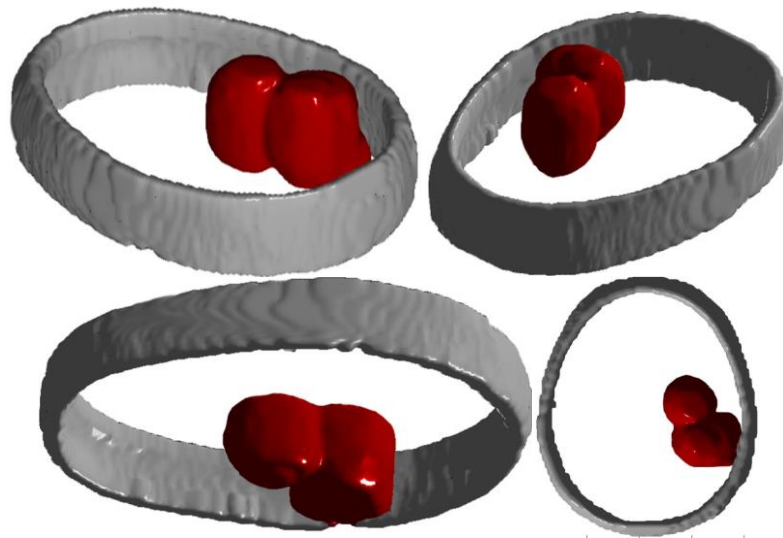


Figure 50 - Different angles of the 3D visualization of final tumors, extracted from MRIs of Figure 49

6.5. Cross validation

For having a better view of the results, we present the following table of images (Figure 51). The first column includes some images of the initial data at the first day of diagnosis. The second column contains the respective images of the simulated data after 112 days, while the third column contains the real data of the images after 112 days. The first impression on the results is that simulated data is quite similar to real data.

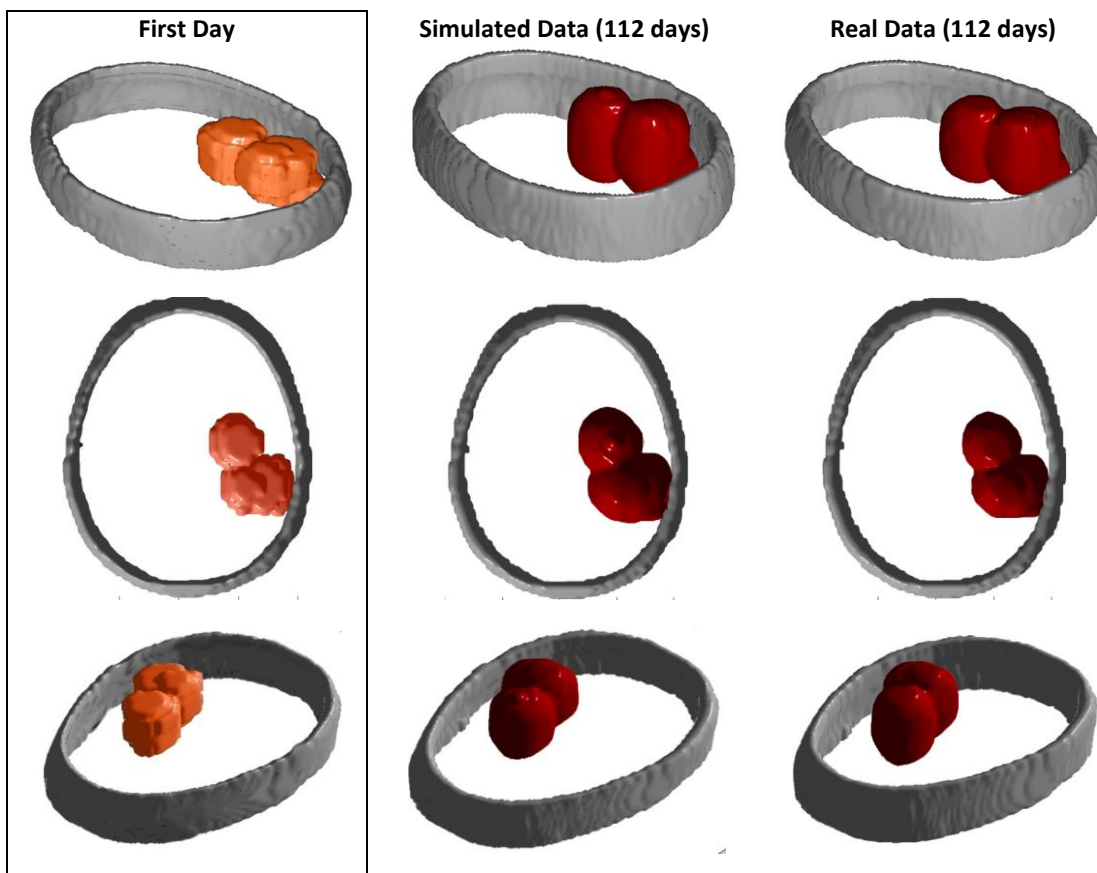


Figure 51 - Results Comparison: (left) Initial Data, (central) Simulated and (right) real data after 112 days.

However, it is important to make a quantitative evaluation of the agreement between the simulated tumor and the final tumor. For evaluation we use a scheme that uses solid metrics and provides objective comparison. Therefore, if we use the final tumor as golden ground truth, then we can adopt the Jaccard (JC), Dice (DS) and Volume Similarity (VS) metrics for identifying similarity [105]. JC, DS and VS are defined as:

$$\begin{aligned} JC &= TP / (FP + TP + FN) \\ DS &= 2TP / (FP + 2TP + FN) \\ VS &= 1 - |FP - FN| / (FP + 2TP + FN) \end{aligned} \quad 69$$

TP (True Positive) is the number of tumor voxels belonging to both the ground truth and simulated result, FP (False Positive) is the number of tumor voxels belonging to simulated result but not belonging to ground truth and FN (False Negative) is the number of tumor voxels belonging to ground truth but not belonging to simulated tumor. In this case, TP, FP and FN are 8515, 356 and 299 voxels, respectively. Thus, the metrics are JC=92.86%, DS=96.30% and VS=99.68%.

Summary

This chapter presents some initial results applied on real MRIs taken from patient with diagnosed GBM. By comparing the results of the simulation, with these of the real data, there seems to be a good agreement. Moreover, for evaluation we adopt a scheme that uses solid metrics and provides objective comparison (JC, DS, VS metrics).

7. Merging model with brain atlases

The diffusive model of the previous chapter takes into consideration the heterogeneous velocity of glioma in gray and white matter, by using two different discrete diffusion coefficients in these two areas. Moreover, by using Diffusion Tensor Imaging, it simulates the anisotropic migration of glioma cells, which is facilitated along white fibers, assuming diffusion tensors with different diffusion coefficients along each candidate direction of growth. This chapter extends this concept by fully exploiting the proportions of white and gray matter extracted by normal brain atlases, rather than discretizing diffusion coefficients. Moreover, the proportions of white and gray matter, as well as the diffusion tensors, are extracted by the respective atlases, thus no DTI processing is needed. This novel model has been applied on real data and the results indicate that prognostication rates can be improved.

7.1. Methods

Instead of using two discrete values for diffusion coefficients in white matter (WM) and gray matter (GM) (depicted in Figure 52), the model uses continuous values, indicating the proportion of white and gray matter in each voxel. Moreover, it has been observed in some cases that a portion of cancer cells can spread in the cerebrospinal fluid (CSF), causing symptoms similar to meningitis - headaches, sickness, and problems with sight and movement [106][107]. For large

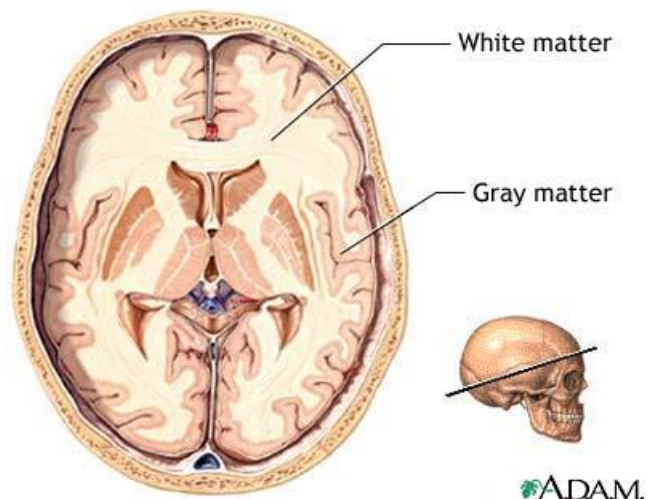


Figure 52 - White and Gray matter brain tissue [110]

glioma, in which proliferating cells may leak to CSF, this could be simulated by setting a non-zero diffusion coefficient for CSF voxels. The proportion of gray, white matter and CSF in each voxel of the patient data has been extracted from the SRI24 atlas [104][108], which is an MRI-based atlas of normal adult human brain anatomy, generated by registering images of 24 normal brains. In order to apply the model the patient, MRI data is initially registered and interpolated to the normal atlas slices. Then, glioblastoma is annotated and delineated on the interpolated patient data by an expert radiologist, before simulating the growth of tumor using this new proposed method. Our hypothesis is that the proposed proportional model can, in most cases, predict glioma growth more effectively than the two standard diffusive models: uniform radial growth across all tissue types and faster diffusion in white matter. An overview of the modeling flow is presented in Figure 53, which depicts the simulation procedure.

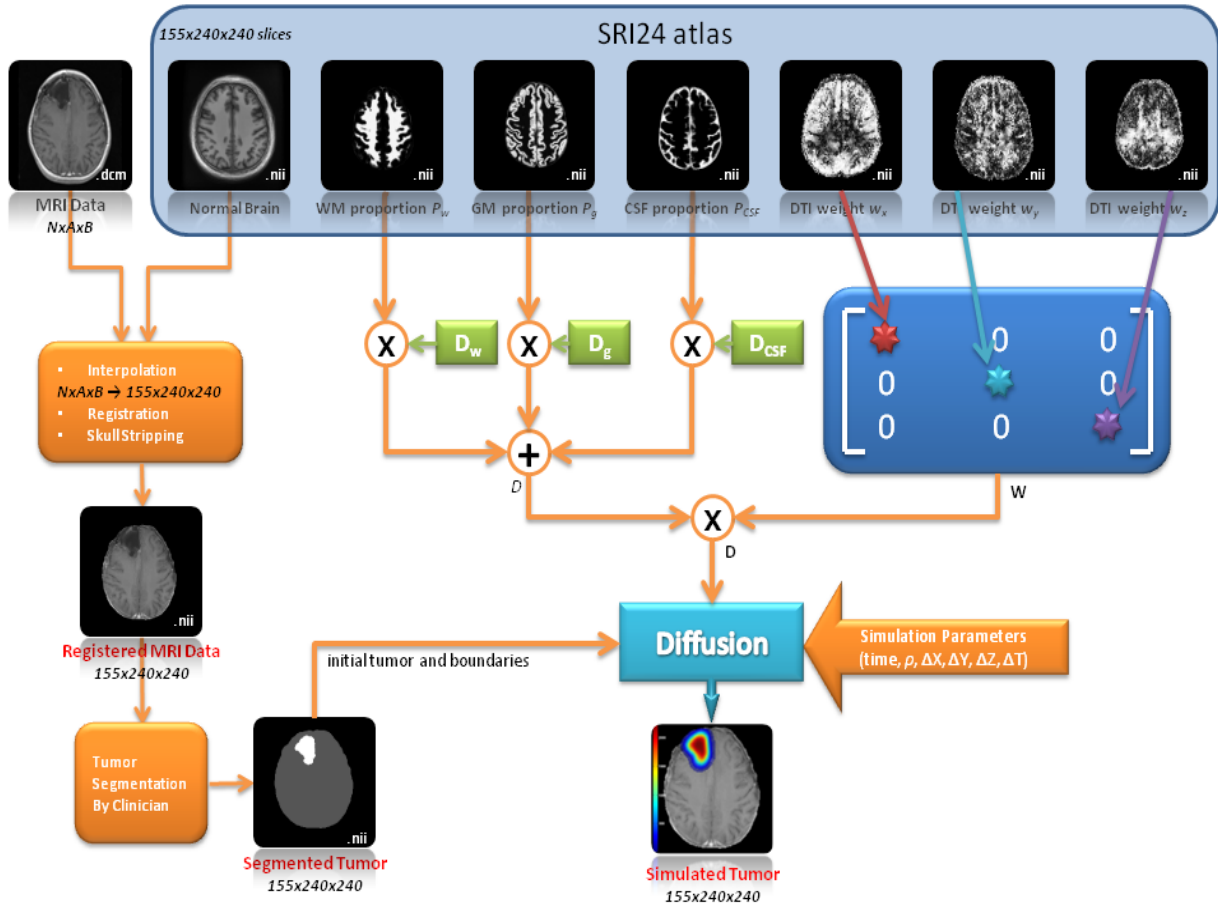


Figure 53 - Flow and overview of the proposed model

7.1.1. Tissue heterogeneity and anisotropic diffusion model

Our biologically based modeling efforts are based on the hypothesis that glioma can be characterized by two net rates, namely proliferation and invasion, which are included in the diffusion - reaction equation (recall Eq. 19). Diffusion (invasion) term incorporates the brain tissue heterogeneity, taking into account that high grade glioma invasion in white matter is 5 times faster than in gray matter [90], by using locally different diffusion coefficients, $D(\mathbf{x})$. Moreover, in order to simulate the anisotropic invasion of glioma along white matter fibers, the local coefficients are multiplied by a matrix \mathbf{W} that describes the anisotropy of cell diffusion along the 3-dimensional directions for each voxel. If the diagonal fiber directions are ignored, the local diffusion weighting tensor $\mathbf{W}(\mathbf{x})$ is an array of the following form:

$$\mathbf{W}(\mathbf{x}) = \begin{bmatrix} w_x(\mathbf{x}) & 0 & 0 \\ 0 & w_y(\mathbf{x}) & 0 \\ 0 & 0 & w_z(\mathbf{x}) \end{bmatrix} \quad 70$$

Here, $w_i(\mathbf{x}) \in [0,1]$, $i = x, y, z$ is the directional diffusion weight, which denotes the anisotropic diffusion of cell migration along the respective direction in position \mathbf{x} . \mathbf{W} denotes the contribution of each axis to the local direction of white fibers, while $D(\mathbf{x})$ actually denotes the scale of this parameter. Thus, by using these definitions, the local diffusion tensor \mathbf{D} in Eq. 19 is expressed as:

$$\mathbf{D}(\mathbf{x}) = D(\mathbf{x})\mathbf{W}(\mathbf{x}) \quad 71$$

And the spatiotemporal diffusion reaction equation that describes glioma growth is equivalent to:

$$\frac{\partial c}{\partial t} = \text{div} \left((D(\mathbf{x})\mathbf{W}(\mathbf{x}))\nabla c \right) + f(c) \quad 72$$

7.1.2. Using proportional local diffusion coefficients

In diffusive models where tissue heterogeneity is simulated by using local diffusion coefficients, $D(\mathbf{x})$ takes two discrete values, that is D_g when voxel \mathbf{x} is located in gray matter and D_w when in white matter tissue. Usually, a fivefold difference between these two values is used, but this can also reach a 100-fold difference in very aggressive high grade glioma [90]. Thus, the brain is segmented into gray and white matter, either by automatic segmentation or by mapping the real medical images on normal tissue atlases, for which a proportion of white and gray matter cells is provided. In the latter case, real images are firstly registered to the atlas. Then, each image voxel is classified either as white or gray matter, according to the proportion of white and gray matter in the respective atlas position. Consequently, if a voxel of the real data is mapped to a voxel in the atlas, for which the proportion of gray matter cells is 51% and the proportion of white matter cells is 49%, then older approaches would classify this voxel as gray matter. However, this totally ignores the existence of white matter and, hence, important information is truncated. Moreover, such models do not simulate glioma diffusion to CSF, although it has been observed that glioma cells may spread in the fluid.

What the current model suggests is to extend this idea and to fully utilize the continuous information on tissue matter, provided by atlases, such as the SRI24 normal brain atlas. Except for the T1 and T2 MRI maps, such atlases provide the proportion $P_w(\mathbf{x})$ of white matter, the proportion $P_g(\mathbf{x})$ of gray matter and the proportion $P_{CSF}(\mathbf{x})$ of CSF in each voxel \mathbf{x} . Thus, after registering medical data on the atlas and setting the diffusion coefficient constants to D_g , D_w and D_{CSF} in white, gray matter and CSF, respectively, the proportional local diffusion coefficient $D(\mathbf{x})$ can be calculated at each voxel \mathbf{x} as follows:

$$D(\mathbf{x}) = P_g(\mathbf{x})D_g + P_w(\mathbf{x})D_w + P_{CSF}(\mathbf{x})D_{CSF} \quad 73$$

Hence, the model makes a total use of the proportion of white/gray matter in brain areas. Indeed, in the previous example, for which the proportion of gray and white matter is 51% and 49% respectively, the voxel was classified as in gray matter, thus the respective diffusion coefficient is $D(\mathbf{x}) = D_g$. On the other hand, the proportional $D(\mathbf{x})$ for the same example is $D(\mathbf{x}) = 0.51D_g + 0.49D_w$, fully exploiting the atlas information of tissue proportion.

7.1.3. The SRI24 atlas

The SRI24 atlas [104] is an MRI-based atlas of normal adult human brain anatomy, generated by registering images of 24 normal brains. This atlas provides the proportions P_g of white and P_w of gray matter at each position of the brain, which can be registered to the clinical

datasets of the patients. The data is provided in 155 slices with 240×240 pixels, for both stripped and unstripped skull.

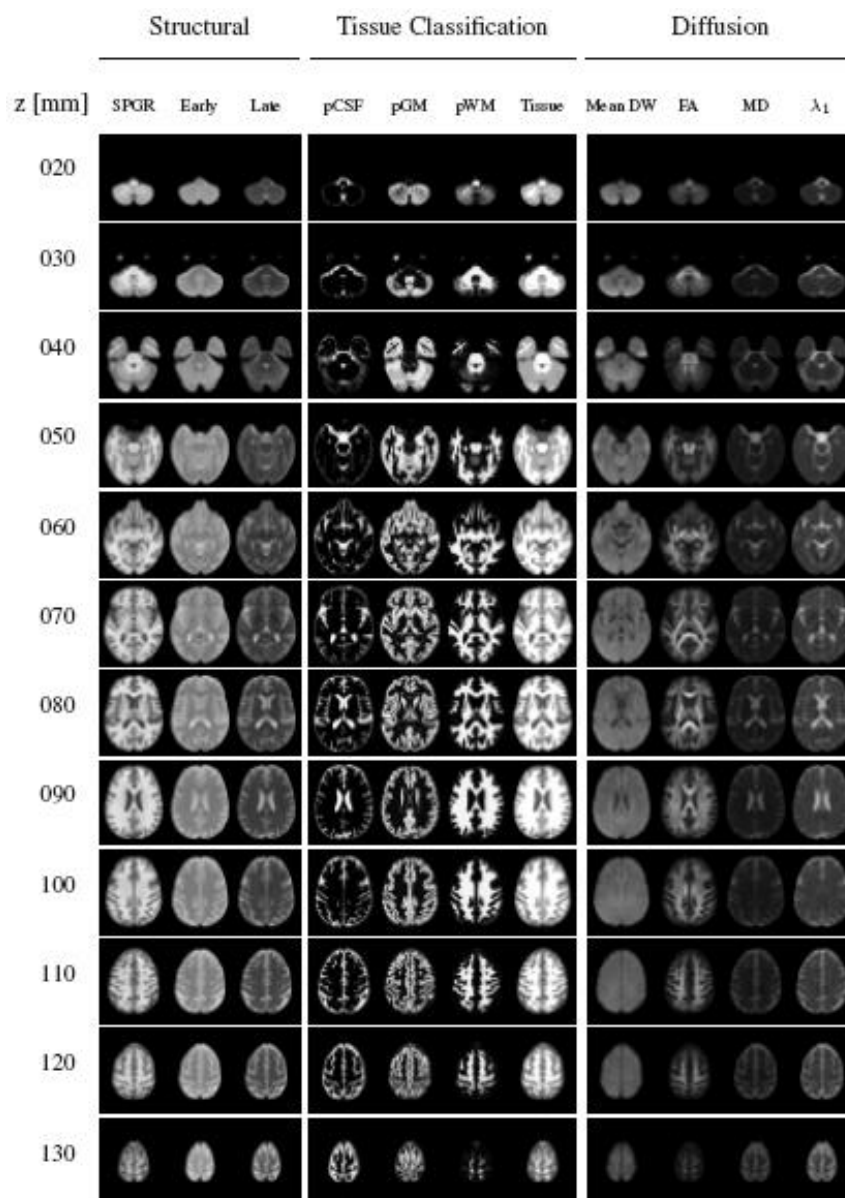


Figure 54 - Channels of the SRI24 atlas (axial slices) [108]

Apart from the matter proportions, the atlas provides the dominant eigenvectors of the diffusion tensor. These eigenvectors have been extracted from DTI, by computing the covariance matrices of the distribution of the 3D Gaussian probability which simulates the diffusion of water. Thus, they can be directly used for simulating the anisotropic migration of glioma cells along white matter fibers, as they represent the directions towards which the water diffusion extends mostly.

By mapping clinical MRI data to a brain matter atlas, it is possible to approximate the required tissue information/ composition in the tumor area, since this is not possible to extract from the real MRI. Hence, using local diffusion coefficients on real MRI images becomes possible, even if the lesion “hides” the underlying tissue.”

Figure 54 presents some slices for the different channels of the SRI24 atlas. In our model we use SPGR (normal brain for registration) and all proportions P_w, P_g, P_{CSF} (i.e the columns named pWM, pGM and pCSF).

7.1.4. The local diffusion weighting factor

In order to simulate the anisotropic growth of glioma along white matter tracts [109], the model uses the 3-by-3 local diffusion weighting tensor \mathbf{W} , which represents towards which direction the distribution of water diffusion extends the farthest. Moreover, SRI24 atlas provides the dominant eigenvectors of the diffusion tensor, which are produced as the covariance matrices of the 3D Gaussian probability distribution that models the water diffusion, at each voxel \mathbf{x} . These eigenvectors have been extracted from DTI.

Thus, since the vector $\mathbf{W}(\mathbf{x}) = \begin{bmatrix} w_x(\mathbf{x}) & 0 & 0 \\ 0 & w_y(\mathbf{x}) & 0 \\ 0 & 0 & w_z(\mathbf{x}) \end{bmatrix}$ is diagonal and $\begin{bmatrix} w_x(\mathbf{x}) \\ w_y(\mathbf{x}) \\ w_z(\mathbf{x}) \end{bmatrix}$ is an eigenvector of \mathbf{W} (this is directly provided by SRI24), \mathbf{W} is directly provided by the eigenvectors of SRI24 atlas.

7.2. Data and Simulation

The model uses T1-MRIs taken from patients diagnosed with malignant glioblastoma multiforme. Such data for 9 patients has been provided by the Department for Pediatric Hematology and Oncology at the University Hospital of the Saarland, in Germany, for the needs of the ContraCancrum project [95], which aims at developing a composite multilevel platform for simulating malignant tumor development and response to therapeutic schedules. For all these datasets provided by Saarland University, there are two or more sessions taken on different dates, while therapy or surgery information has been provided, for tracking glioma development. However, because of its aggressive nature, the GBM is usually excised after diagnosis and for this reason only one case (without surgery or therapy) was found by the time this work was written. However, 8 more cases were found where the partially excised tumor was followed up with imaging examinations while the patient received radiotherapy and simulations were performed in those specific intervals.

7.2.1. Data Preprocessing

The proposed model requires that both atlas and real data are registered and have the same form and size before applying modeling Eq. 72. In our test case, the patient dataset consists of 29 T1-MRI slices with unstripped skull (255×255 pixel images), while the SRI24 atlas provides 155 slices of normal brain (240×240 pixel images), with stripped and unstripped skull. Figure 55 (a) shows the 8th slice of the patient dataset, where the tumor has its largest size. The tumor has been identified on the left frontal lobe. Images (b) and (c) depict the 99th slice of the SRI24 atlas normal brain, unstripped and stripped respectively. These are the most similar images to the real slice shown in (a).

Initially, the patient dataset has to be aligned to the midsagittal line, for correcting skew distortion before registering to the atlas using the MIPAV Application [110]. Next, the skull in

the patient dataset is removed to match the stripped atlas images using fully-automated skull stripping technique, namely the Brain Extraction Tool (BET) [111].

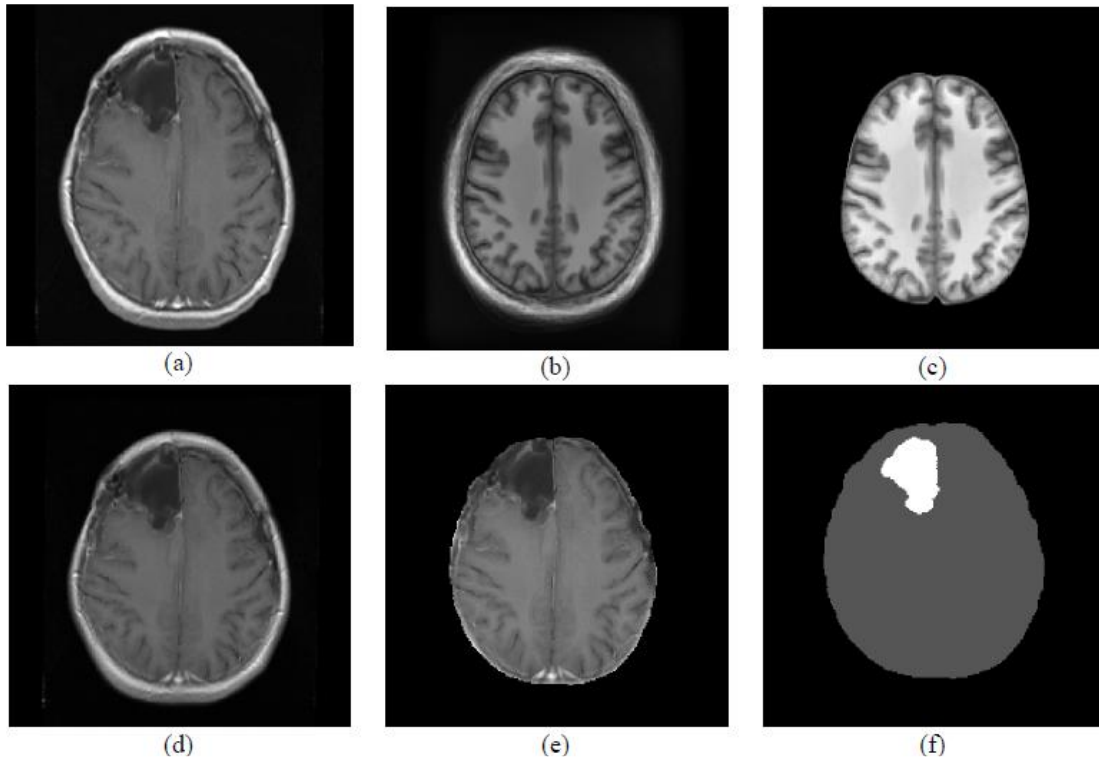


Figure 55 - (a) 8th slice of the initial 29-slice patient dataset before registration (b) the most similar to (a) unstripped slice of normal brain atlas (99th slice), (c) similar to (b) for stripped brain, (d) the 99th slice of the patient dataset after registration and interpolation, (e) the 99th image after skull stripping, (f) is annotated (d)

The final registration step is done using the Optimized Automatic Registration 3D approach, by MIPAV. This method iteratively determines an optimal transformation of the image that globally minimizes a cost function (correlation ratio in our case), starting from the lowest resolution of the target image and moving to the highest (i.e. a simple blurring filter was applied to downgrade the resolution of the image). The optimum transformation is determined by the minimization of the correlation ratio (between target and reference images) computed for several rotation angles which vary from -30 to 30 degrees over the grid. The reference, as well as the target image are resampled and interpolated (using trilinear interpolation) to create high resolution isotropic voxels. Finally, the registration of the two images is completed by calculations performed to the center of mass from both images. The derived unstripped, registered and interpolated patient dataset consists of 155 slices with dimension 240×240 and being registered to the atlas. Figure 55 (d) presents the 99th slice of the registered to the atlas patient dataset and (e) presents the same slice after skull stripping.

The last step before handing data over simulation is the delineation of the initial tumor boundaries provided by expert radiologists from the University of Saarland using the annotation and segmentation platform DoctorEye [112][113]. The delineated slice is shown in Figure 55 (f) (in white). Summarizing, after acquiring the stripped, registered, interpolated and annotated dataset, diffusion simulation can be performed. A screenshot of the DrEye

tool during annotation is presented in Figure 56, where different areas (green, red, blue, yellow) have been selected.

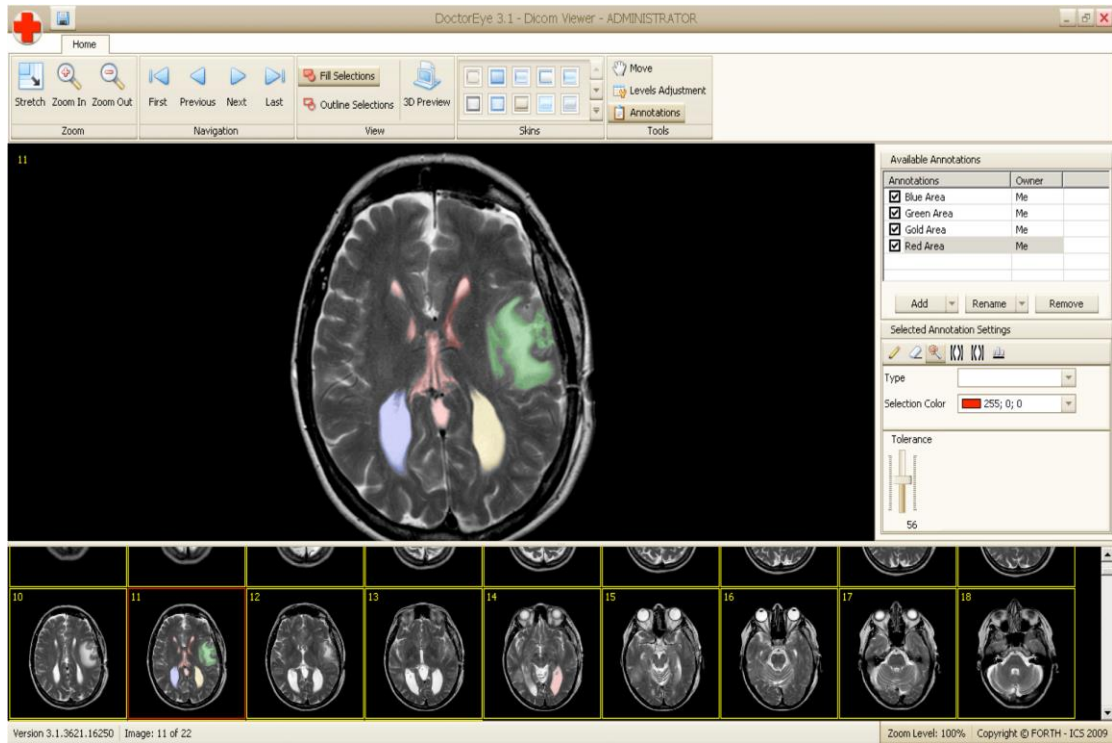


Figure 56 – DrEye screenshot: different areas of interest may be annotated accordingly using respective labels in different colors.

Patient image data can now be directly mapped to the SRI24 atlas, where $D(\mathbf{x})$ and $\mathbf{W}(\mathbf{x})$ for solving Eq. 72 are available. Following the current example, Figure 57 (a-d) presents the respective mappings of the P_w , P_g , P_{CSF} and one of the three coordinates of the dominant eigenvector (w_z). It is important to mention that because these coefficients depict proportions of brain matter and directionality measures, the image values are ranged in $[0,1]$. On the other hand MRIs in Figure 55 (a-d) take discrete intensity values in $[0, 1, \dots, 255]$.

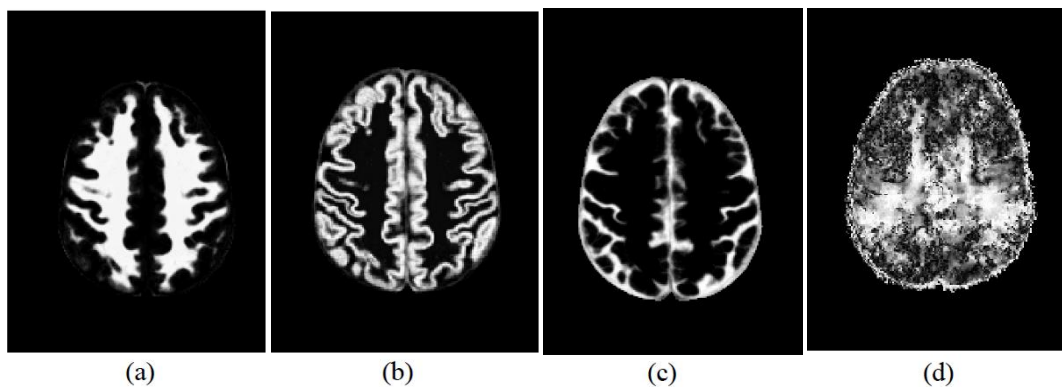


Figure 57 - The SRI24 atlas mappings for the proportion of (a) white matter (P_w), (b) gray matter (P_g) and (c) cerebrospinal fluid (P_{CSF}) and the one out of the three dominant eigenvector images (w_z), respective to the example of Figure 55

7.2.2. Model Parameters

As already mentioned, one real temporal glioma case was chosen on the basis that no surgery was performed and no therapy given to the patient (Figure 55) for demonstrating our method in detail, consisting of two sets of 29 T1-MRI slices, taken from two different post-treatment sessions. The respective T2 MRIs were also available and were used for estimating how well the model parameters D and ρ , extracted from bibliography [81], approached the values derived with the method proposed by Harpold et al. [80][114].

This specific patient suffered from inoperable glioblastoma and did receive irradiation for 2 months, till 17-12-2009, concurrently with temozolomide treatment. Then, the tumor was stable for 16 days and progressed again. The first dataset of MRI slices after treatment was acquired on 31-3-2010, while the second set on 31-5-2010. Thus, the tumor progression within that 60-day post-treatment period can be approximated as a free-growth procedure, i.e. $T(t)=0$. Similarly, the rest 8 datasets were intentionally picked from similar cases (with post-operation relapse of tumor), so as to model glioma growth as free- growth procedure for the respective period of time for each case.

The proliferation parameter ρ was set to the constant value of $\rho=0.012 \text{ day}^{-1}$ corresponding to the observed rate of high-glioma of previous chapters. Similarly, the constant values D_w and D_g for diffusion were set as $0.010 \text{ mm}^2/\text{day}$ and $0.002 \text{ mm}^2/\text{day}$ respectively. These values were found to meet the values derived with the method proposed by Harpold et al. [80], for estimating the ratio D/ρ by using the two T1 and T2 MRI sessions. For the rest 8 cases, ρ was set to the constant value 0.012 day^{-1} . On the other hand, D_w and D_g were picked from bibliography, for high glioma values, to optimally correspond to the respective values of D , estimated by Harpold's method for $\rho=0.012 \text{ day}^{-1}$.

Continuing, because the CSF is rarely invaded by glioma cells, a first approach adopted for simulating diffusion in CSF was to set a very small diffusive coefficient as $D_{CSF}=0.01 D_w$. The value of D_{CSF} was not arbitrarily chosen, but it has been estimated by applying the method of Harpold et al. on a different provided dataset where CSF has been infected by glioma cells. Thus, the ratio D_{CSF}/ρ was estimated in the CSF area, by using two T1 and T2 MRI sessions.

Moreover, the initial concentration for the tumor voxels was set at $200 \text{ cells}/\text{mm}^3$ and the Verhulst law parameter for the maximum concentration was defined as $c_m=10^6 \text{ cells}/\text{mm}^3$. Lastly, the simulation grid dimensions were defined as $\Delta X = \Delta Y = \Delta Z = 1 \text{ mm}$, the time step was defined as $\Delta T = 1 \text{ h}(1/24 \text{ day})$ and the overall modeling time of cell progression was 60 days, as in the real clinical case.

7.3. Results

After extracting the required datasets using the SRI24 atlas and after defining the simulation parameters, the proposed model of Eq. 72 can be applied on the real annotated clinical case. Figure 58 (a) presents the 99th slice of the initial tumor, as produced after data preprocessing and (b) shows the respective simulated glioma concentration after 60 days of progression, mapped on the initial dataset. On the other hand, Figure 58 (c) presents the respective real final tumor, as provided by the clinicians. Lastly, Figure 58 (d) depicts the 3-dimensional

perspective of the initial brain tumor. Figure 58 (e) presents the simulated tumor after 60 days, while (f) presents the real tumor, derived after registering and interpolating the real tumor (second session) to the atlas. The visualization threshold of the simulated tumor concentration was set to 400 cells / mm³.

In order to better evaluate the efficiency and the practical usefulness of the model, it is important to conduct a large number of simulations with real data, especially datasets with the characteristic fingering invasion of glioma. However, from the figures reported here, there seems to be a good qualitative agreement between the real and the simulated tumor growth. The next step is to evaluate the performance of the proposed model using all nine datasets, comparing it to the two standard diffusive models: uniform radial growth across all tissue types and faster diffusion in white matter with discrete diffusion coefficients.

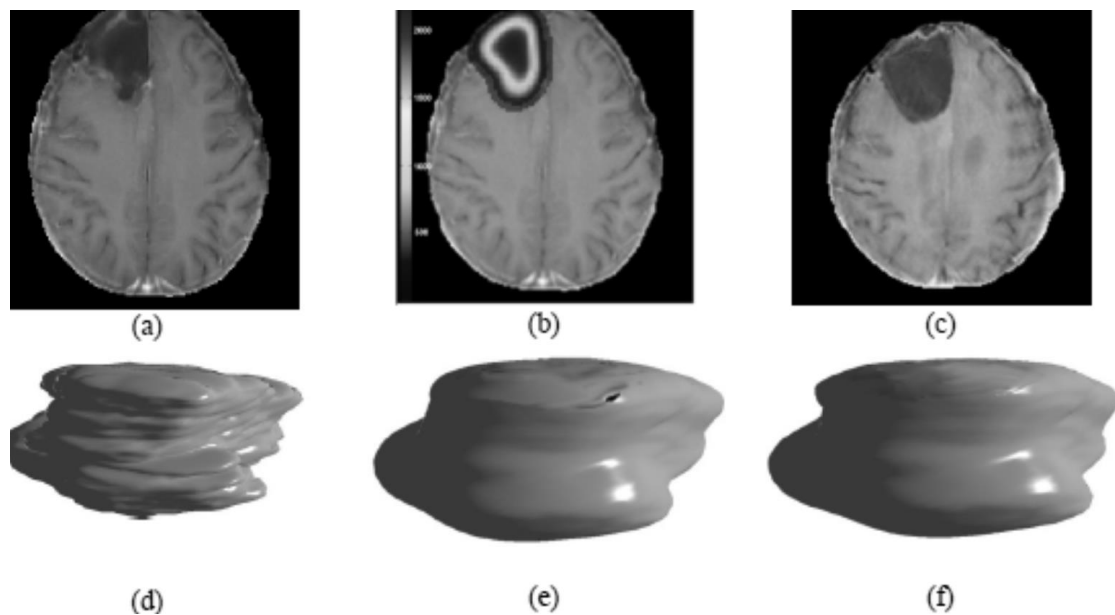


Figure 58 - Some simulation results; Up: the 99th slice of the (a) initial tumor, (b) the simulated final tumor, mapped on (a), and the (c) real final tumor. Down: the 3-dimensional reconstructions of (d) the initial annotated tumor, (e) the simulated tumor after 60 days and (f) the real annotated tumor after 60 days.

7.4. Cross Validation

We have made simulations on a series of nine datasets in order to compare the simulated tumor with the final actual tumor, as annotated by the radiologists. In the eight other cases however, the tumor was treated with radiotherapy which isn't currently taken into consideration in the models compared. For evaluation, we used the scheme Jaccard (JC), Dice Similarity (DS) and Volume Similarity (VS) metrics that we used earlier.

The evaluation metrics have been calculated on the simulation results of the nine patient datasets. On each dataset, three different models have been applied; the proportional model, the model with uniform tumor growth and the model with discrete values for $D(\mathbf{x})$. After running all three models for each dataset, the metrics for each one have been calculated. Finally, the average metrics for each model have been estimated.

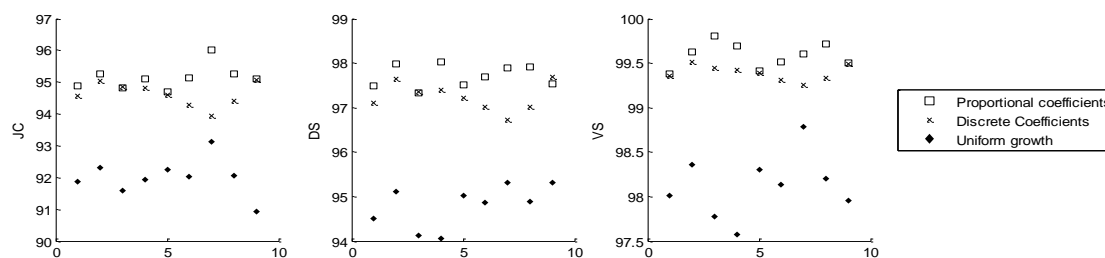


Figure 59 - Scatter plot of JC, DS and VS (%) for 9 cases where the proportional, the discrete and the uniform growth models have been applied

The scatter plots of the three metrics are presented in Figure 59. For the proportional model, the average JC is 0.54% higher than the discrete model and 3.39% higher than the uniform growth model. Similarly, the average DS for the proportional model is 0.48% and 3.07% higher than the discrete and the uniform model, respectively. Lastly, the average VS is 0.19% and 1.49% higher for the proposed model, compared to the results of the discrete and the uniform growth model, respectively. Thus, the results indicate that there is a potential advantage of the probabilistic diffusion coefficients over uniform and discrete diffusion parameters. ■

Summary

The first applications on real patient datasets, of the continuous proportional diffusion coefficients, proposed in this work, instead of the discrete two-value coefficients, seem to slightly improve the average performance of these models. This indicates that using proportions of tissue matter on each voxel, instead of classifying them either in GM or WM, valuable information is not truncated and the model simulates more accurately the actual tumor growth.

The proportional model requires the a priori knowledge of white matter, gray matter and CSF proportions and the directions of the white matter tracts in brain. Therefore, structural and statistical information of brain is extracted by open-access brain atlases, such as SRI24. By mapping clinical MRI data to a brain matter atlas, it is possible to approximate the required tissue information / composition in the tumor area, since it is not possible to extract from the real MRI data we had in this work. Hence, simulation using local diffusion coefficients on real MRI images becomes possible, even if the lesion “hides” the underlying tissue. This of course, is an approximation and the added value can only be assessed through extending the gold truth experiments / results presented herein. However, it should be stressed that GBM follow ups without surgery are rare since surgery is performed in almost all cases after diagnosis rendering impossible to assess actual temporal tumor evolution.

Apart from the commonly used gray matter and white matter tissue information, CSF proportion is also provided and utilized for simulating the rare cases of glioma, in which the cerebrospinal fluid has been invaded by tumor cells. Tumor expansion in CSF has been modeled by applying a non-zero diffusion coefficient. In the current experiments, the initial tumor size was not so large to allow tumor cells migrate into CSF, as in real cases. However, in experiments for large glioblastoma, where CSF might get infected, tumor cells have

appeared in the CSF areas. Therapy has been simulated with the current model, after adjusting the treatment term $T(t)$, and is presented in next chapter.

8. Radiotherapy

The characteristics of GBM lead to aggressive treatment strategies that most often include surgery, irradiation and chemotherapy. The mathematical approaches that were used for simulating GBM growth inevitably raised the need for incorporating techniques for therapy simulation. Including therapy parameters in GBM models could help the clinicians optimize therapy schemes, as they could predict the response of patients to different therapeutic plans.

This work presents the results of applying a linear quadratic model for simulating the effects of radiotherapy on real clinical datasets. The model used is the diffusive GBM model of the previous chapter, after ignoring the effect of CSF, with some extensions. This study extends our prior model with *in silico* prediction of tumor growth to incorporate the effects of radiotherapy in real clinical datasets. Compared to previous model this approach includes some improvements:

- The application of the linear quadratic model on our previous model for simulating radiotherapy.
- The simulation of radiotherapy in multiple fractions by using the linear quadratic model.
- The evaluation of radiotherapy simulation by using Jaccard, Dice and Volume similarity metrics.
- The anisotropic diffusion of cells only in white matter areas, excluding gray matter tissue.

8.1. Methods

This study makes use of the proportional diffusion model presented in the previous section, accounting for proportional diffusion coefficients, ignoring diffusion in CSF ($D_{CSF} = 0$). This work extends the previous model by improving Eq. 73, so as to turn off anisotropic migration in gray matter tissue. In order to apply anisotropy only to white tissues, as noticed in clinical praxis, the identity matrix \mathbf{I}_3 is used for changing Eq. 73 to the following formalism:

$$\mathbf{D}(\mathbf{x}) = P_g(\mathbf{x})D_g\mathbf{I}_3 + P_w(\mathbf{x})D_w\mathbf{W}(\mathbf{x}) \quad 74$$

8.1.1. The Linear Quadratic model

This work investigates an extension of the preceding proportional glioma model to include the effects of the radiotherapy using the Linear Quadratic Model. According to the model, the probability of cells surviving S following a single dose of radiation $R(\mathbf{x}, t)$ was observed to follow this relationship [115]:

$$S(R) = \exp(-aR - \beta R^2) \quad 75$$

where *linear* α (Gy^{-1}) and *quadratic* β (Gy^{-2}) are the radiobiology parameters, which are interpreted biologically as repairable single and lethal double-strand breaks to the cell's DNA, respectively [116]. In our case, where the clinical datasets have been extracted from patients with radiation in a number of fractions with the same dose, Eq. 75 turns to the following equation [117]:

$$S(R) = \exp(-aR - \beta Rr) \quad 76$$

where r is the dose per fraction and $R = nr$ is the total dose for n fractions. In general, fast-proliferating cells, like GBM, have a high tissue response α/β . In our experiment, we use a constant ratio $\alpha/\beta=10$ that is widely used in clinical applications for highly developing cancer and has been extracted from empirical dose response data [114]. Thus, if 4b is used for approximating cell proliferation, the overall proliferation term $f(c)$ for Eq. 72 turns out to be the following.

$$f(c) = \begin{cases} \left(\rho - (1 - e^{-aR(t) - \beta R(t)r(t)}) \right) c \frac{c_m - c}{c_m} & , t \in \text{therapy} \\ \rho c \frac{c_m - c}{c_m} & , t \notin \text{therapy} \end{cases} \quad 77$$

8.1.2. Clinical Datasets and Model Settings

The model uses T1- and T2-MRIs (255x255 pixel slices) taken from six patients diagnosed with malignant glioblastoma multiforme and cured with radiotherapy. The datasets were provided by Saarland University, Germany, for the needs of the ContraCancrum project [95]. For each dataset there is information provided for the dose and the fractions. Moreover, there are two or more sessions taken on different dates for tracking glioma development and evaluation simulation result.

The simulation workflow is similar to that of the previous section, with $f(c)$ adjusted to Eq. 77. The clinical datasets have been firstly registered and interpolated to the atlas. After registration, the datasets are delineated by expert radiologists by using DoctorEye (mentioned earlier). In order to solve the DRE, the Crank Nikolson numerical scheme has been implemented in three dimensions. We used $\rho=0.012 \text{ day}^{-1}$, $D_w=0.010 \text{ mm}^2/\text{day}$, $D_g=0.002 \text{ mm}^2/\text{day}$, $c_0 = 10^6 \text{ cells}/\text{mm}^3$. For the solver of Finite Differences, we used a grid with dimensions $\Delta X = \Delta Y = \Delta Z = 1\text{mm}$ and a stable time step of $\Delta T = 1h$.

8.1.3. Radiotherapy Settings

Before applying the model, it is appropriate to estimate the values of the radiobiology parameters α and β . The method used is that of Rockne et al. [114], by projecting the temporal tumor curves for different values of a on the real datasets. Estimating radius is ideal for spherical tumors however GBM has very complex shape. Thus, instead of tumor radii, the estimated total number of GBM cells is used for identifying the value of a that minimizes the error between simulated and actual target total GBM cells.

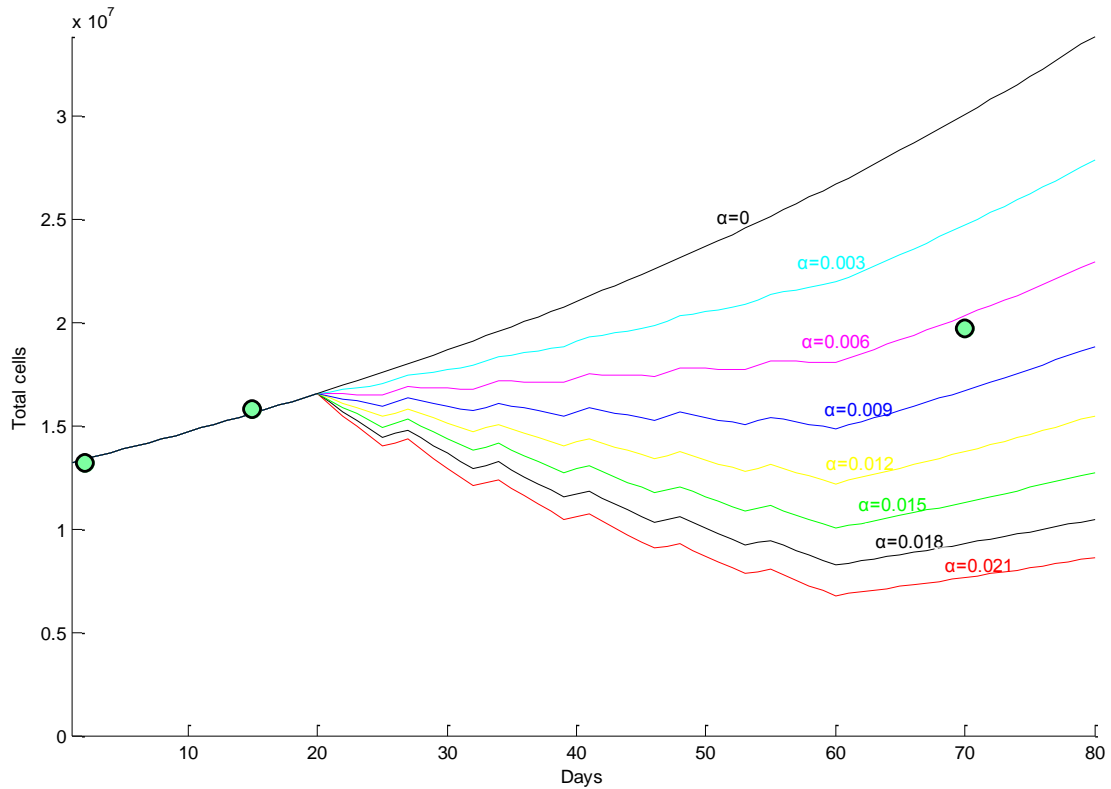


Figure 60 - The curves depict the total number of GBM cells for one patient for eight values of α ranging from 0 (no effect of radiotherapy) to 0.021 Gy^{-1} after applying the diffusive model. The same plot shows the three different points of real cell numbers, estimated after segmenting the tumors on three MRI datasets on the respective days. The optimal value of α lies around 0.006 Gy^{-1} .

Figure 60 presents a set of simulated curves extracted for one specific patient after applying seven different values of α . The real tumor total cells are marked on the curve for three different MRI provided (the three green points on day 1, 15 and 70). The patient was treated with a total dose of 60 Gy at 2 Gy per fraction and 5 fractions per week for 6 weeks. Treatment starts 21 days after the first MRI and finishes on day 56. Each different curve is extracted by simulating radiotherapy for 0.003 increments of α , starting from zero (no effect) and reaching 0.021 Gy^{-1} . One can see that the optimal value for α , that minimizes the error from the total number of cells is $\alpha = 0.006 \text{ Gy}^{-1}$. The same process is followed for approximating the radiobiology parameters for the rest five patients. Table 12 presents the patient specific parameters for all the patients.

Patient	Age	$\alpha \text{ (Gy}^{-1}\text{)}$	$R \text{ (Gy)}$	$r \text{ (Gy)}$	n
1	47	0.114	60	2	30
2	64	0.003	48	3	16
3	52	0.006	60	2	30
4	41	0.211	58	2	29
5	73	0.000	42	3	14
6	56	0.013	60	2	30

Table 12 - Summary of model parameters for all six patients with glioblastoma multiforme included in the study

8.2. Results

After defining all simulation parameters, the diffusive model has been applied on the clinical datasets of MRIs. Figure 61 presents the simulated results for the 4th patient 21 days after the end of radiotherapy (100 days after diagnosis). The hot areas depict the resulting simulated tumor projected on the real MRI dataset. The real dataset has been extracted on the same day of simulation.

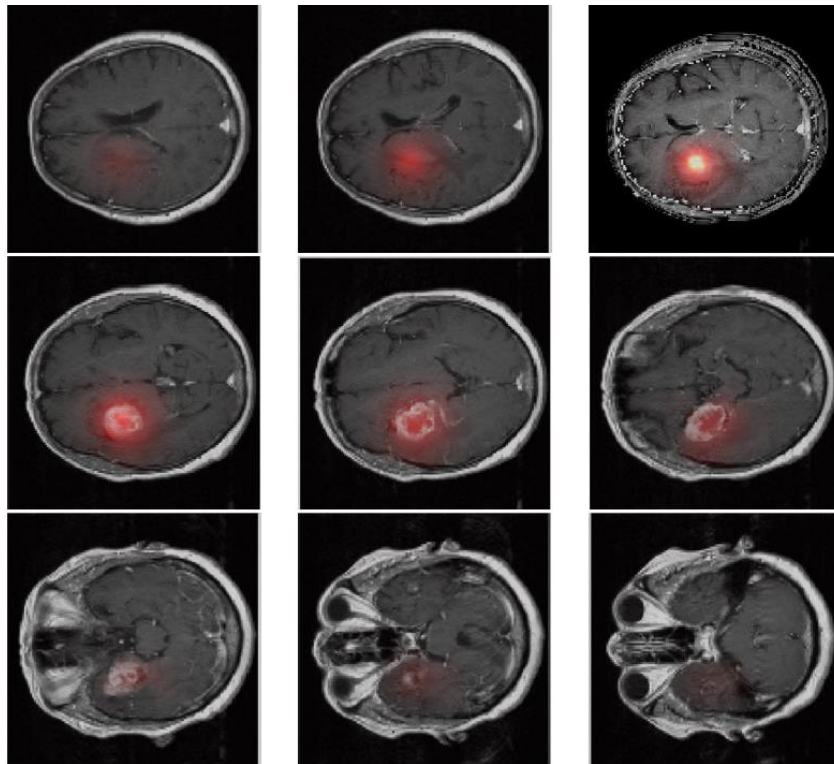


Figure 61 - The simulated cell concentration (hot areas) projected on the real patient data on the 100th day after diagnosis and 21 days after the last fraction of radiotherapy

For this specific patient, radiotherapy caused shrinkage of the tumor, which cannot be clearly seen on the simulation results of Figure 61. In order to have a better understanding of the shrinkage effect of radiotherapy, we use a line intersecting the point with the maximum concentration. Then, concentration is estimated along this line and presented on a graph. This is applied both on the real initial MRIs (day 1) and the simulated final result. Figure 62 (left) shows the initial MRI with the intersection line projected, while Figure 62 (right) presents the graph of the concentration of GBM along this line. The red curve shows the initial estimated concentration along this line, while the blue curve shows the simulated concentration of radiotherapy along the same line. In order to have a better visualization of the shrinkage effect, we also provide Figure 63 that depicts the change of the total number of cells in time (for 100 days). It is obvious that the tumor has shrunk considerably.

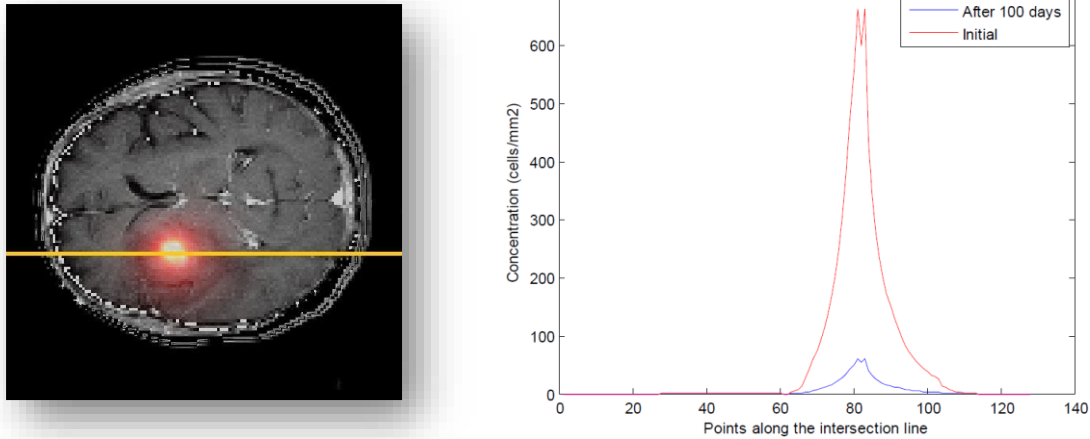


Figure 62 - The graph presents the tumor cell concentration for the initial day (diagnosis day) and the 100th day after diagnosis (21th day after the last fraction of radiotherapy). These values have been calculated along the yellow line shown on the left MRI slice, which comes across the point with the maximum concentration value

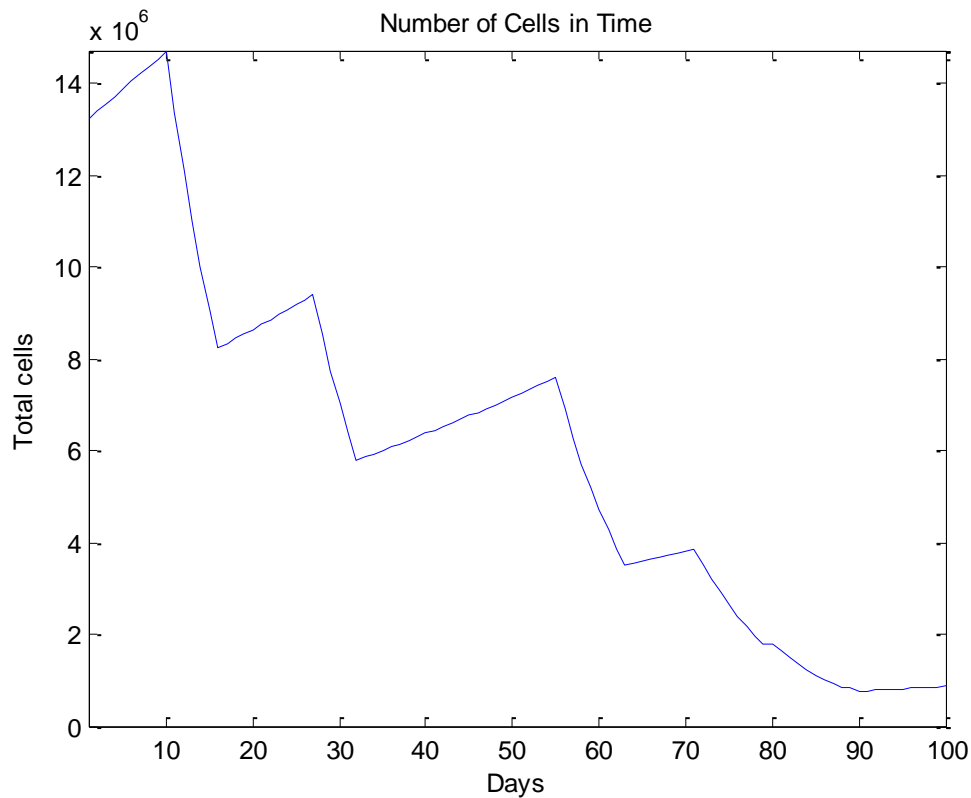


Figure 63 - The temporal change of the number of glioma cells for the 4th patient for 100 days. The last radiotherapy session was carried on day 79.

8.2.1. Cross validation

We have made simulations on a series of six datasets in order to compare the simulated tumor with the final actual tumor, as annotated by the radiologists. Similarly to all previous simulations, the annotated final tumor serves as a golden ground truth and the Jaccard (JC), Dice (DS) and Volume Similarity (VS) metrics are adopted.

Figure 64 depicts the scatter plots of the three metrics for each patient. The average resulting JC, DS and VS values for all patients are 95.21%, 98.09% and 99.62%. These values are 2.1%, 4.01% and 1.89% higher than the respective results for discrete diffusion coefficients and 6.45%, 8.49% and 4.07% than the uniform tumor growth model.

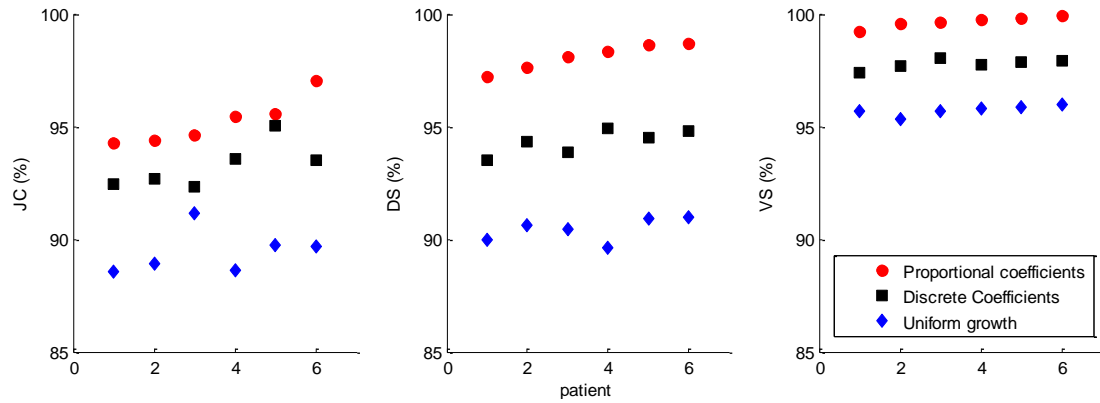


Figure 64- Scatter plot of JC, DS and VS (%) for six cases where the proportional, the discrete and the uniform growth models have been applied



Summary

Radiotherapy is usually applied in fractions and the linear quadratic model has been adjusted to this, contrary to previous diffusive models which use the quadratic model for a single dose. By using the formalism of Eq. 76, the diffusive model incorporates this idea.

9. Introducing Gross Tumor Volume

In this work we propose an extended model of GBM growth including the brain deformation (mass effect) induced by the tumor invasion. Furthermore, we propose to make the link between the classification of tumors in Gross Tumor Volumes (GTV) proposed in some protocols for radiotherapy treatment [118] and the two distinct invasion behaviors:

- The GTV1 is associated with the expansion component. Because it does not infiltrate the tissue, this proliferation is directly correlated with a volume increase. By creating new cells, the GTV1 pushes away the surrounding structures. It is therefore responsible for the major mechanical mass effect. The GTV1 is thus described in our model with a new stress equation.
- The GTV2 is associated with the diffusion component. It invades adjacent structures by a diffusion process and is responsible for the infiltration in white and gray matter. This diffusion component expands faster than the GTV1 but exhibit little mass-effect. The GTV2 is thus described in our model with the reaction-diffusion equation we already have designed.

In our model T1-contrast enhanced MRI is used for delineating GTV1, while T2 MRI is used for delineating GTV2 [72]. An example of the usual GTV segmentation can be seen on Figure 65. The model is initialized using a standard segmented patient MRI.

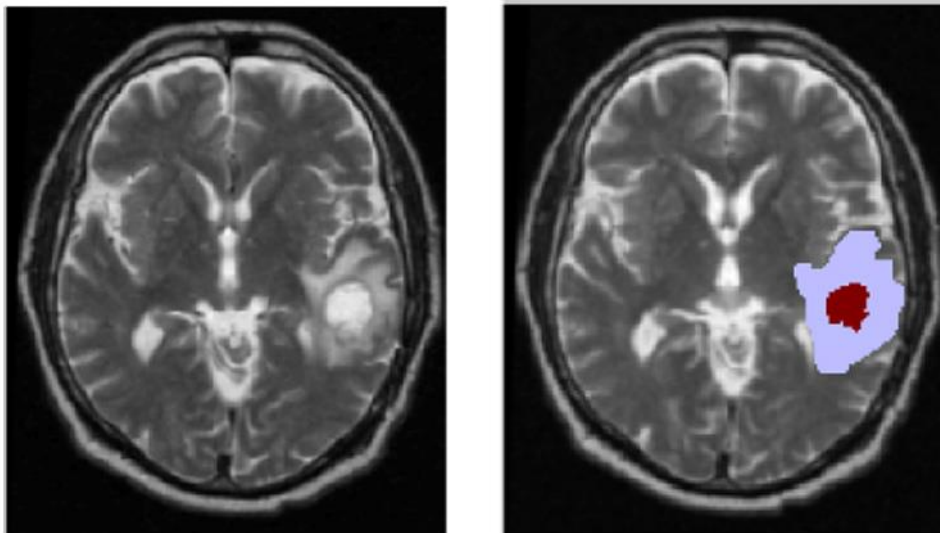


Figure 65 - MR images of a patient (left) T2; (right) GTV1 (dark red) and GTV2 (light blue) segmentations overlaid on the T2 MRI.

9.1. Methods

9.1.1. Real Initial and Final Dataset

As already mentioned, the model of this chapter follows the same procedure of the previous chapter. T1, T2 and T1-contrast (with gadolinium) are required MRI modalities for the purposes of this method. Therefore, a dataset of a 54 year old male patient with diagnosed

GBM has been acquired for the needs of the ContraCancrum project, providing these modalities. The initial MRI session used here, has been extracted on 5th day after therapy (on 16-2-2010), while the final MRI session has been produced on 15-7-2010, without treatment in between. Both sessions include 19 slices of 256x256-pixel MRI images. Figure 66 shows some sample slices of the initial dataset (3 modalities), where tumor can be identified at the right part of the brain. Figure 67 presents the respective slices for the final dataset.

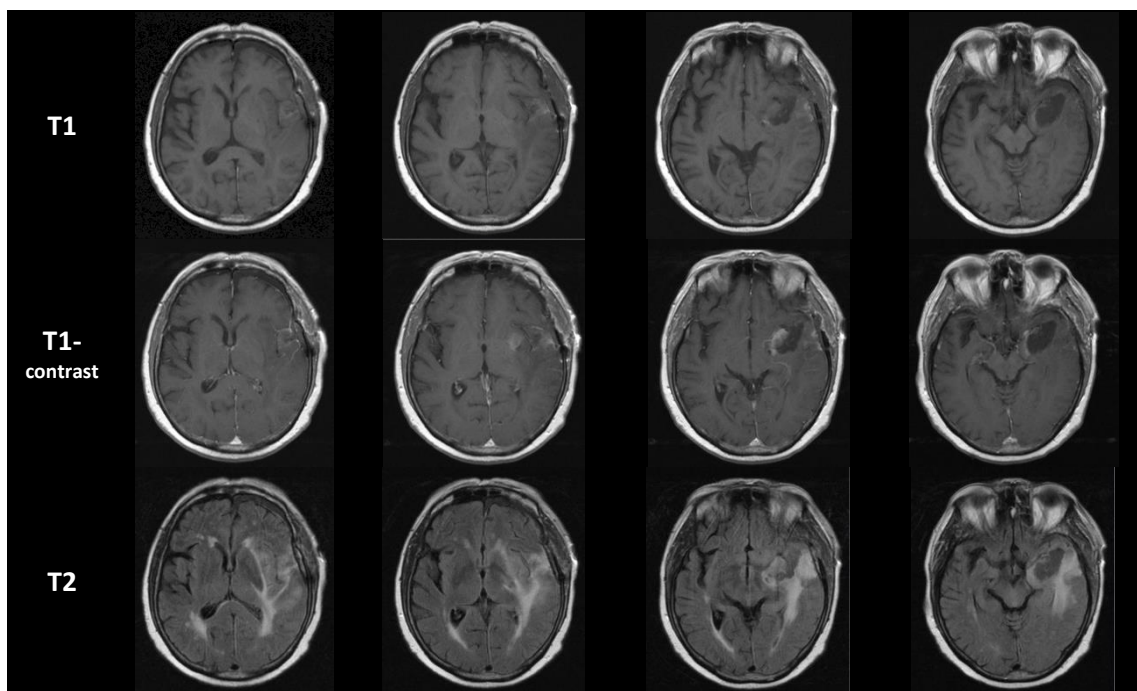


Figure 66 - Slice 11, 13, 15 and 17 (out of 19) taken from the initial dataset on Feb 16, 2010

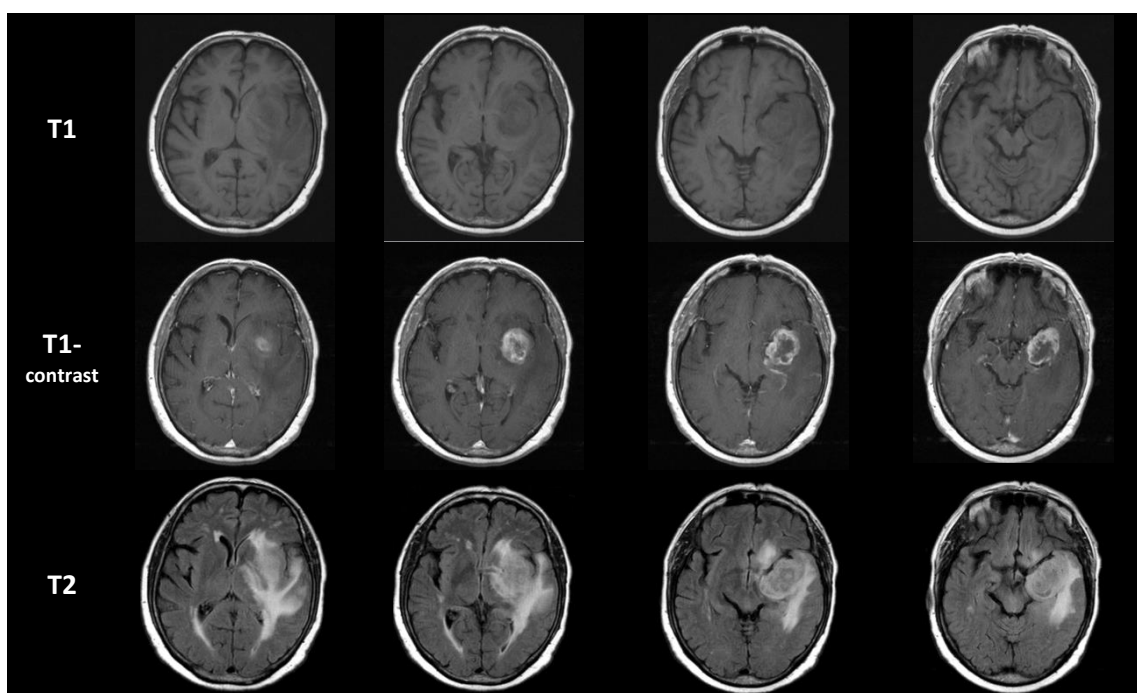


Figure 67 - Slice 11, 13, 15 and 17 (out of 19) taken from the final dataset on July 15, 2010

9.1.2. Annotation of GTV1 and GTV2

Radiologists from Universität des Saarlandes Klinikum (Germany) have used the platform of DrEye for delineating the areas of GTV1 and GTV2 on T1-contrast and T2 MRIs, respectively. However, before annotation, the slices have been registered and interpolated to the SRI24 atlas following with the same procedure as in previous model, producing 150 slices of 240x240 pixels.

Figure 68 (a-c) shows an example of GTV1 and GTV2 annotations on T1-contrast and T2 70th slice and their merged version on T2, for the initial session. Similarly, (d-f) show the respective slices for the real final tumor.

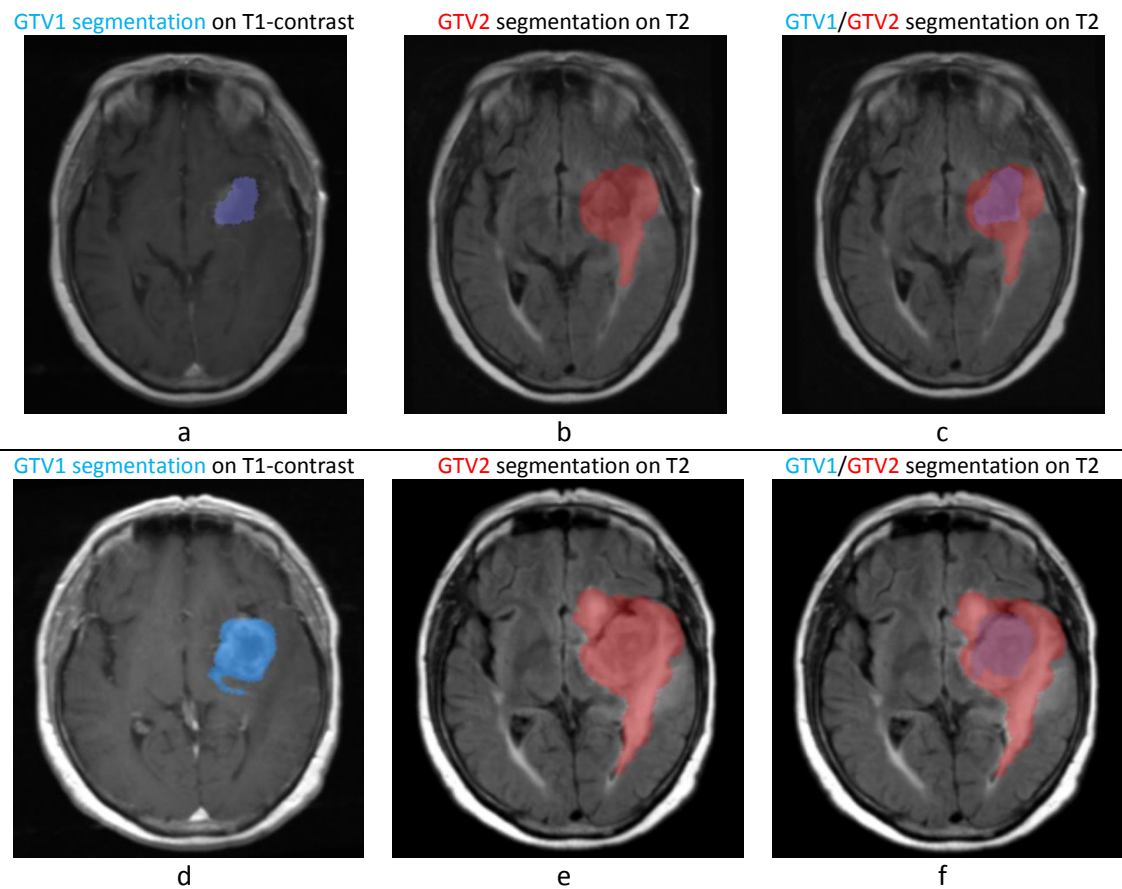


Figure 68 - Annotations of (a) GTV1 on T1 contrast, (b) GTV2 on T2, and GTV1 + GTV2 on (c) T1-contrast and (d) T2 for the real initial tumor. (d-f) the respective of (a-c) for the final tumor.

9.1.3. Simulation

After annotation, the next step is to move to the simulation process. Initially, the initial tumor slices are translated into a 3 dimensional grid, which allows us apply the diffusion equation. In order to set the initial concentration of tumor cells, we initially set $T_{h,gtv2}=8000$ cells/mm³ around the borders of GTV2 and $T_{h,gtv1}=35000$ cells/mm³ around the borders of GTV1 [52]. Then we solve the steady state version of DRE with numerical integration until equilibrium is nearly reached. At the end we derive the interpolated concentration between the two initial contours of GTVs. Figure 69 presents various angles of the 3D representation of the initial tumor, with skull, GTV1, GTV2 and ventricle plotted for $T_{h,gtv1}$ and $T_{h,gtv2}$.

GTV1+GTV2+Ventricle+Skull

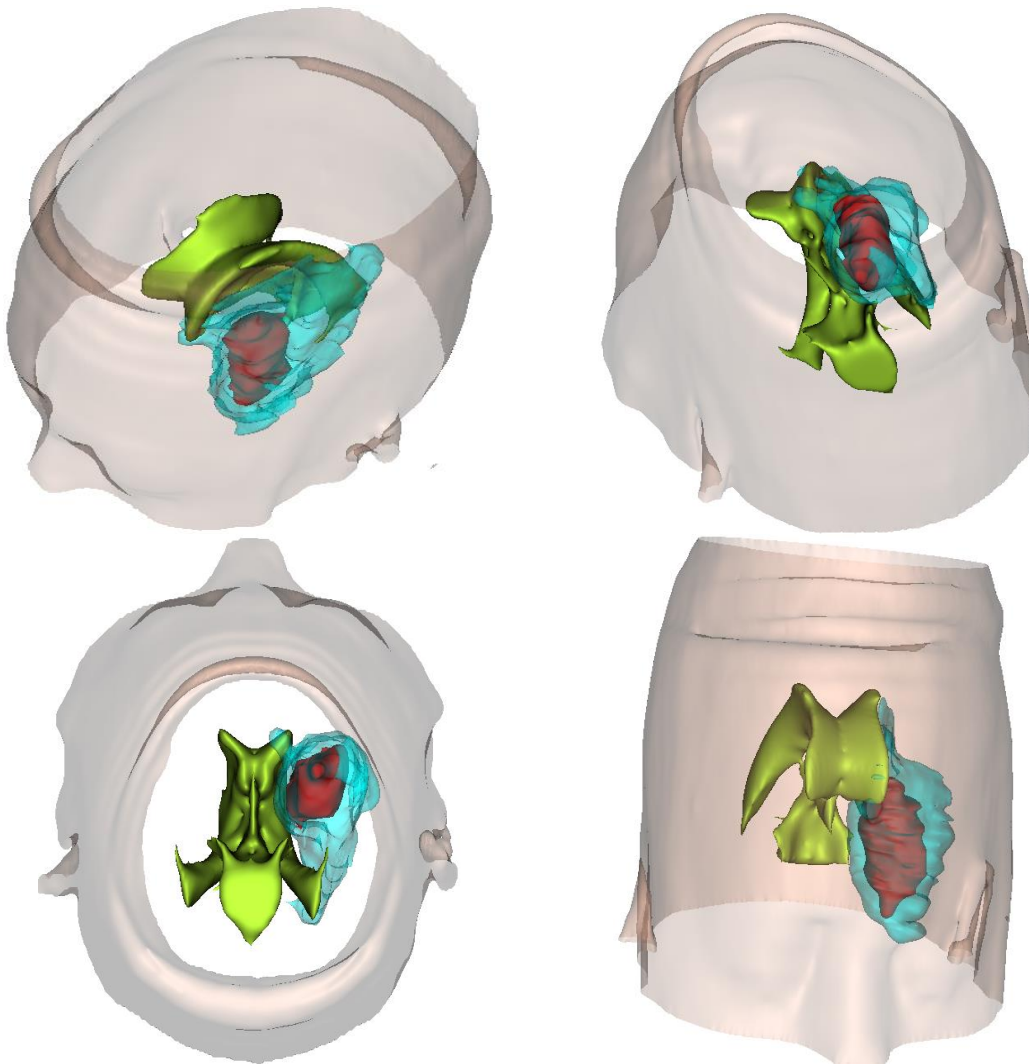


Figure 69 – GTV1 and GTV2 of the initial tumor are plotted within the brain, with skull and ventricle drawn.

After setting up the initial concentration, the simulation starts over 180 fictitious days. Every 1 day the algorithm computes the mass deformation caused by the increasing tumor, by solving a stress function using COMSOL tool [72]. This stress is translated into new gray and white matter proportions, thus new diffusion coefficients are then used.

9.2. Results

Figure 70 shows a cross check of the real initial, real final and simulated final tumor after thresholding GTV1 and GTV2 areas with $T_{h,gtv1}$ and $T_{h,gtv2}$. From a first view, a very good agreement is observed with fingering being predicted. In order to have a better perspective of the real and simulated tumor, Figure 71 presents a cross presentation with transparent parts of GTV1 so as to check the overlapping areas. It is easy to notice that there is a very good agreement between real final and simulated results.

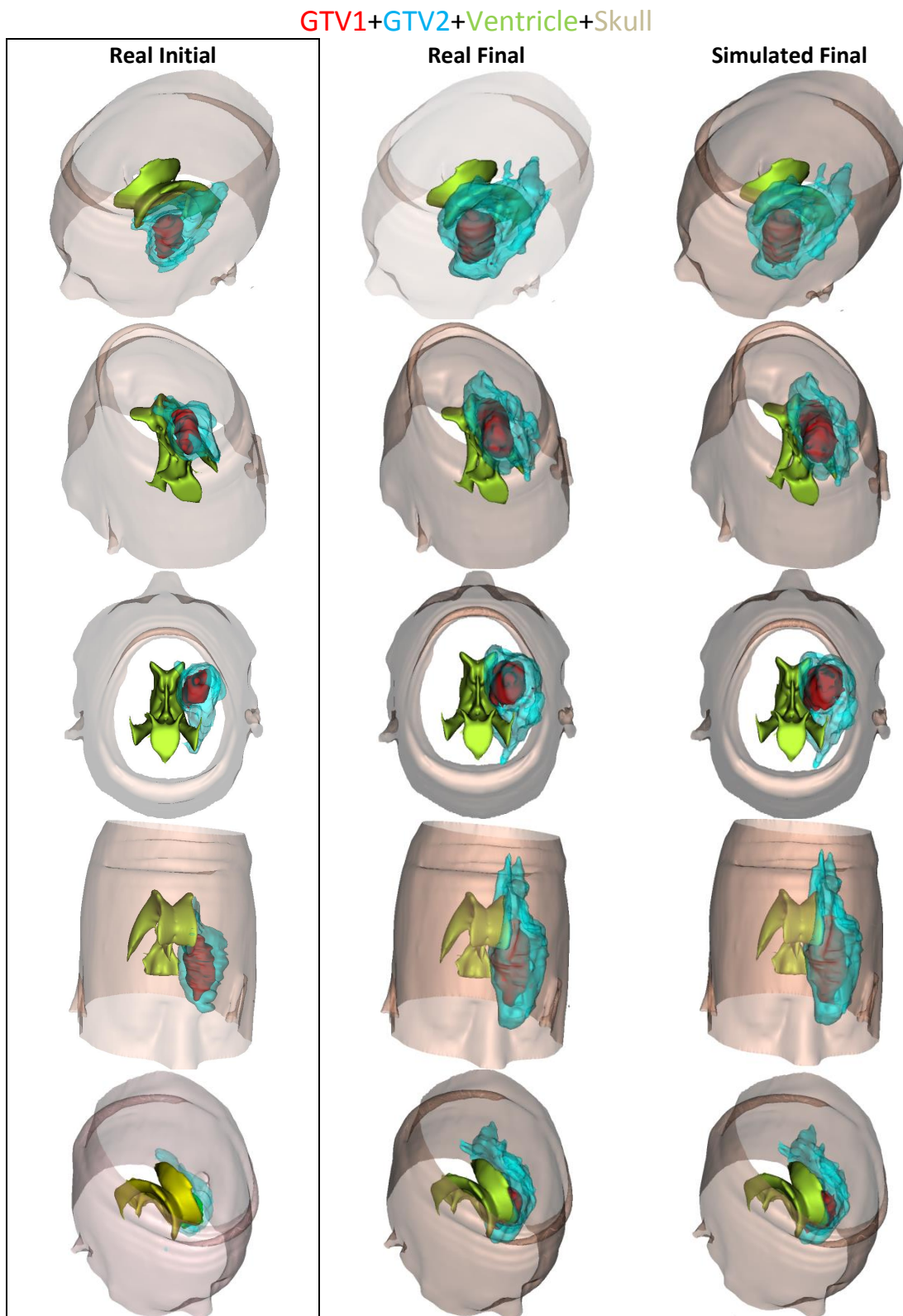


Figure 70 – Different angles of the real initial, real final and simulated final tumors depicting GTV1, GTV2, ventricle and skull.

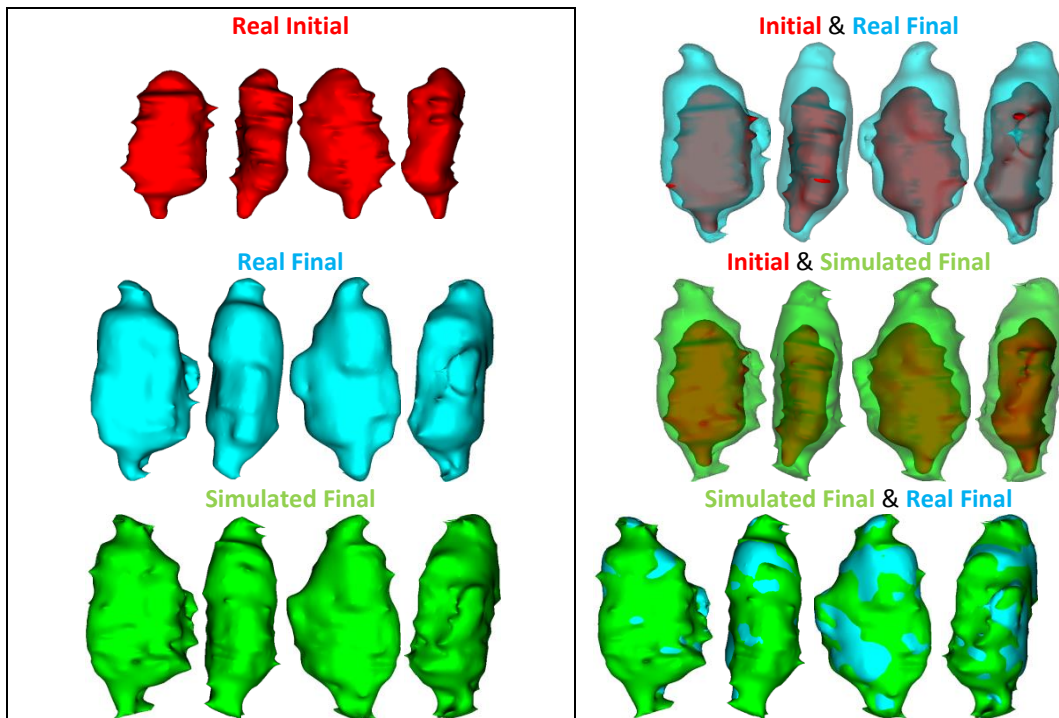


Figure 71 – Cross presentation of GTV1 (left column): real initial, real final and simulated final tumor; (right column) cross check of initial over real final, initial over simulated final and simulated over real final tumor.

9.3. Cross validation

Similarly to all previous simulations, the final tumor (GTV1 only) serves as a golden ground truth and the Jaccard (JC), Dice (DS) and Volume Similarity (VS) metrics are adopted. In order to locate the TP, TN, FP, FN we use the evaluation plugin of DrEye. Figure 72 (left) presents an example of evaluation using this tool for a specific slice and (right) the produced results for the entire tumor. The metrics were computed as JC=82.06%, DS=91.93% and VS=95.20%.

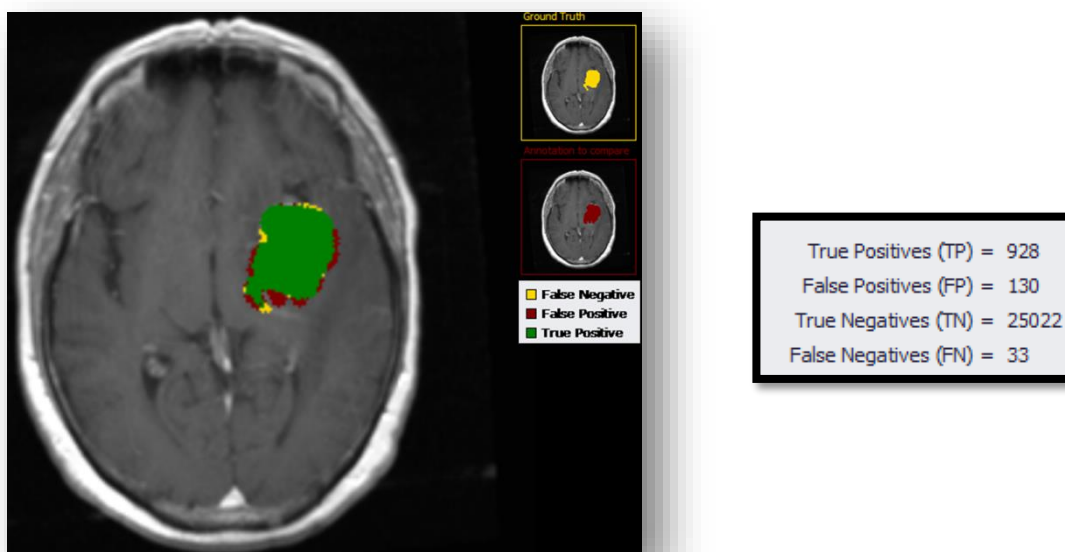


Figure 72 – (left) Example of evaluation using DrEye for a specific slice and (right) the estimated values for TP, FP, TN, FN for the entire tumor.

10. Proliferation–Invasion–Hypoxia–Necrosis–Angiogenesis model

During the last decades, especially via the EU initiative related to the Virtual Physiological Human, significant progress has been made in advancing *In silico* computational models to produce accurate and reliable tumor growth simulations. However, currently most attempts to validate the outcome of the models are either done in-vitro or ex-vivo after tumor resection. In this work, we incorporate information provided by fluorescence molecular tomography data performed in-vivo into a new mathematical model that describes tumor growth and builds upon the diffusive model by incorporating the angiogenic net rates and different concentration of cell populations (normoxic, hypoxic and necrotic). This work presents the proliferation- invasion- hypoxia- necrosis- angiogenesis (PIHNA) model in two dimensions. The outcome is validated against tumor evolution snapshots captured in vivo using advanced molecular probes in laboratory animals.

10.1. Introducing the PIHNA model

The previous model assumes that cancerous cells proliferate at a constant global rate which is independent of nutrients availability and the cell population has the same type. In order to incorporate nutrient availability and oxygenation, the model of Eq. 19 can be altered to the proliferation- invasion- hypoxia- necrosis- angiogenesis (PIHNA) model [119][115]. This model includes three different types of cell population, normoxic, hypoxic and necrotic, while vasculature and angiogenic factors (e.g. VEGF) have also been incorporated into the model.

The emerging system of equations for these three types of cells, endothelial cells (vasculature) and angiogenic factors are:

$$\frac{\partial c}{\partial t} = \nabla \cdot (D(1-T)\nabla c) + \rho c(1-T) + \gamma hV - \beta c(1-V) - a_n n c$$

$$\frac{\partial h}{\partial t} = \nabla \cdot (D(1-T)\nabla h) - \gamma hV + \beta c(1-V) - (a_h(1-V) + a_n n)h$$

$$\frac{\partial n}{\partial t} = a_n h(1-V) + a_n n(c+h+v) \quad 78$$

$$\frac{\partial v}{\partial t} = \nabla \cdot (D_v(1-T)\nabla v) + \mu \frac{\alpha}{K_m + \alpha} v(1-T) - a_n n v$$

$$\frac{\partial a}{\partial t} = \nabla \cdot (D_a \nabla a) + \delta_c c + \delta_h h - q \mu \frac{\alpha}{K_m + \alpha} v(1-T) - \omega a v - \lambda a$$

where $V = v/(c+h+v)$, $T = (c+h+v+n)/k$. In first equation $c(\mathbf{x}, t)$ is the concentration of normoxic cells at position \mathbf{x} at time t . The cells diffuse at a rate D , proliferate at a rate ρ , turn to hypoxic at a rate β or turn directly to necrotic (due to contact death) at a rate a_n .

Similarly, $h(\mathbf{x}, t)$ is the concentration of hypoxic cells, which diffuse at a rate D , turn back to normoxic at a rate γ or turn to necrotic at a rate a_h .

Continuing, $n(\mathbf{x}, t)$ is the concentration of necrotic cells, while $v(\mathbf{x}, t)$ and $a(\mathbf{x}, t)$ are the vasculature (endothelial cells linked to oxygenation) and concentration of angiogenic factors, respectively. Vasculature disperses at a rate D_v , increases at a rate $a_v = \mu \frac{a}{K_m + a}$ and turns to necrotic cells at rate a_n .

Lastly, angiogenic factors are produced by normoxic cells at rate δ_c and by hypoxic cells at rate δ_h , decay at a rate λ and are washed out by vessels at rate ω . In the last two equations, μ is the proliferation rate of endothelial cells, K_m is the Michaelis – Menten constant of response of endothelial cells to angiogenic factors and q is the consumption of angiogenic factors per endothelial cell proliferation.

10.2. *In vivo tumor growth*

What has been achieved so far is a noteworthy number of computational (in silico) attempts to study the various phases and scales of cancer describing different levels of biocomplexity. Most of the approaches in *in-silico* oncology have been targeted to the provision of insight into the tumor growth mechanisms (cancer biology modeling). Yet, a parallel need of crucial importance is to serve the above models with advanced anatomical and functional imaging methods able to localize and image the tumor, while being appropriate for in vivo staining, such as fluorescence molecular probes, and proteins.

Advances in biomedical imaging technologies brought about in recent years have revolutionized the way we approach a variety of medical and biological questions. Novel technological approaches have shed light into biological processes and function, with the field of *in vivo* molecular imaging recognized as one of the most influential for translational research [120][121]. By connecting gene activity with physiology the molecular basis of health and disease can be studied and understood. Important factors of disease and especially cancer, such as angiogenesis, hypoxia, metabolism and the pathways regulating the response to external stimuli can now be targeted and monitored at a very early stage and at a molecular level.

In the field of optical tomographic imaging, increasingly used for pre-clinical research, a wide variety of probes have been developed enabling the specific targeting of many different molecular functions. In addition the ability to use fluorescing proteins with animal cancer models makes monitoring the progress of disease straightforward. Optical tomographic techniques can provide 3D imaging of fluorescence light emitted from the probe or protein [120]. In the case studied and presented here a Fluorescence Molecular Tomography (FMT) system is used to image signal emitted from HeLa cancer cells expressing the red emitting protein Katushka injected subcutaneously in the hind limb flank of mice. Imaging performed longitudinally provides a direct monitoring of the growing tumor[122].

10.2.1. Animal preparation

For the studies presented here Rag1^{-/-} immunodeficient mice were used. Katushka expressing HeLa cancer cells were injected subcutaneously and grown as xenografts in the hind limb flanks. Initially 5×10^5 cells were injected and tumours were allowed to grow until 4-10mm in diameter. Animals were kept anaesthetized using isoflurane throughout the preparation and imaging procedures. A small tumour (typically <1mm diameter) was generally visible within 4-5 days following the injection, at which point imaging was initiated, while the mice were sacrificed 11-20 days after implantation, depending on tumour size.

10.2.2. Experimental Procedure

The experimental system used for *in vivo* imaging is depicted in Figure 73 - The experimental setup for *in vivo* tomographic imaging. It comprises a series of laser sources employed according to the fluorescence target. A diode laser (Soliton-GmbH, Germany) emitting at 592nm was used to excite Katushka as close to the absorption maximum as possible. A cooled 16-bit CCD (Andor BV-434, Belfast, Northern Ireland) camera was used for the detection of signals. Light collection was performed through a 50mm Macro f/2.8 objective (SIGMA Corporation, Tokyo, Japan) and different interference bandpass filters (Andover Corporation, USA) for isolating the fluorescence and excitation signals. In the case presented here, fluorescence was acquired using a 700/75nm filter, whereas no filter was used for the excitation. The system can be operated in both transmission and reflection geometry, however, in this study only reflection measurements were done since the targets were superficially located. An optical scanner was employed to scan the laser source into the desired points on the surface of the subject. In all experiments described here 49 illumination points were used in a 7x7 arrangement.

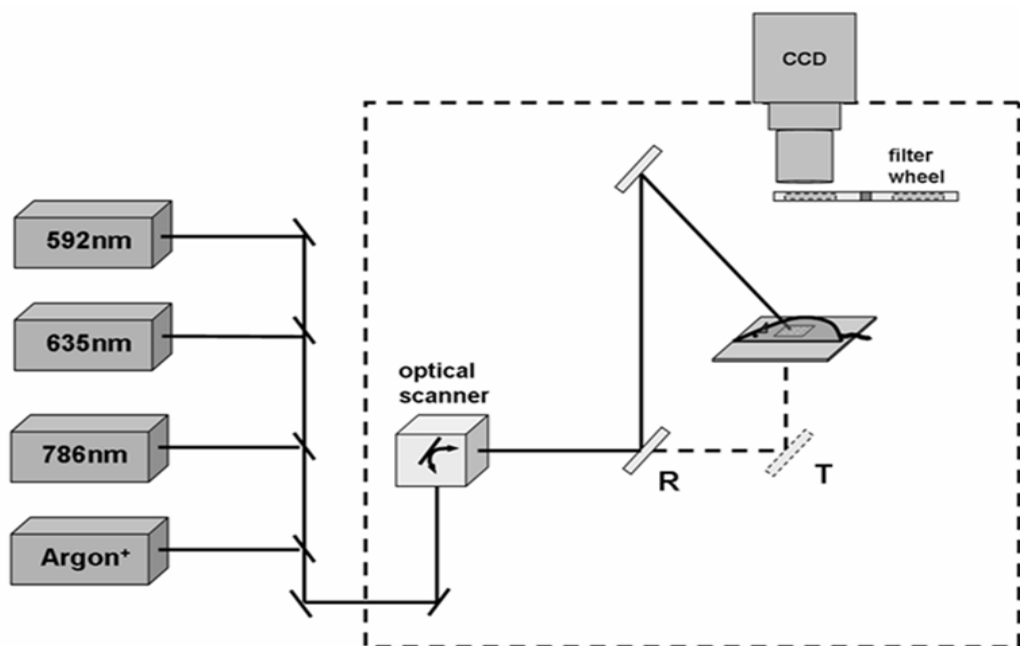


Figure 73 - The experimental setup for *in vivo* tomographic imaging

10.3. Tomographic Imaging

Tomographic imaging was performed by raster scanning the laser source into selected illumination points on the subject, taking care that the scanning area covers the targeted tumor. For each illumination point two measurements are recorded sequentially, by selecting the appropriate filters as described above: the excitation light diffusely reflected back to the camera and the fluorescence light emitted by the Katushka expressing cancer cells. The two measurements were then combined in the tomographic algorithm to produce the 3D reconstructions. Light propagation was modeled by Diffusion Theory, while a normalized calculation approach was used to combine the two acquired intensities [123]. Reconstructions were performed with an iterative method without solving directly for the fluorescence due to the size of the weight matrix [124]. The mesh used for the reconstructions was 26x26x6 voxels in size with an axial resolution of 0.5mm and a depth resolution of 0.8mm. The result is a 3D reconstruction of the fluorescence intensity that can be associated to the cancer tumor and when longitudinal studies are performed, monitor its growth over time.

10.4. Results

In this section the results from *in vivo* imaging and the *in silico* model applied to the requirements of the specific mouse model are presented.

10.4.1. *In vivo* tumor growth

As described above to monitor tumor growth *in vivo* animals were imaged for several days and fluorescence data were analyzed for each imaging session in order to obtain the growth curve of the tumor. Characteristic images of the excitation and fluorescence signals recorded during the study can be seen in Figure 74b and c. These excitation and fluorescence were obtained by summing up the raw images for all illumination points. Data in Figure 74 correspond to day 9 after the injection of the HeLa cells and a clear tumor can be observed with a size of *circa* 3-4mm.

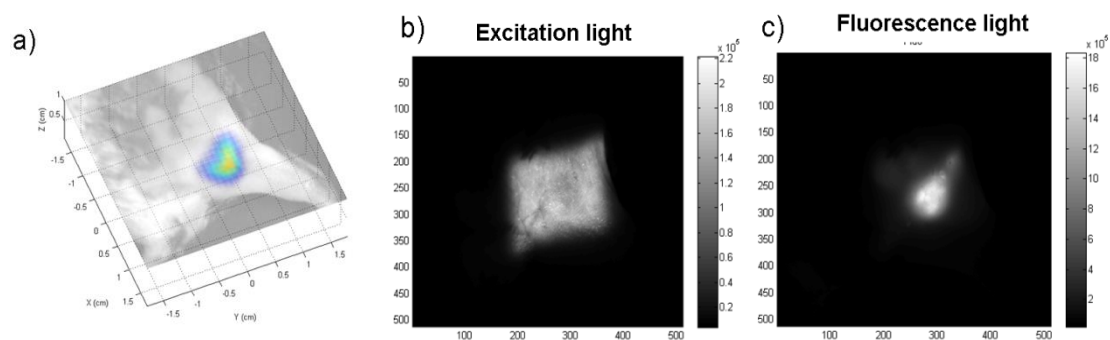


Figure 74 - 2D raw data obtained during *in vivo* imaging of tumor growth in a mouse model. a) 3D fluorescence reconstruction image showing the tumor in the flank of the mouse. b) image of the excitation light showing the scanning area and c) image of the fluorescence light emitted by the Katushka expressing HeLa cells.

Figure 74a presents the fluorescence reconstruction in 3D overlaid on the white light image of the animal. The data from the reconstructions from each day were then used to obtain the growth curve of the specific tumor. This was performed by calculating the mean

fluorescence intensity of the reconstruction and then plotting against time (days). Results are presented in Figure 75 (red-square-pointed line) where reconstructed fluorescence intensity is plotted as a function of time after injection. A fast onset of growth is observed for the first 3 days, which is then slowed down until a plateau is reached after the 7th day. This behavior can be explained by the increasing competition among cancer cells for space and nutrients as tumor grows and can be simulated by the *in silico* model presented in the following section.

10.4.2. *In silico* tumor growth

In order to simulate tumor growth, we used the mathematical model described in section III. The system of equations (1) were solved in a 100×100 grid spanning an overall area of $L \times L$ for $L = 2\text{cm}$ and the temporal resolution was set to $\tau = 8h$. The parameters used in the model are depicted in Table 13. The proliferation rate of HeLa cells is set according to [125]. To simplify modeling, in all simulations described here vasculature is assumed homogeneous.

Parameter	Value	Nondimensionalized	Parameter	Value	Nondimensionalized
T_c	$18.24 \left(\frac{\text{days}}{\text{cell}} \right)$	T_c	δ_c	$7.59 \cdot 10^{-16} \left(\frac{\text{mmol}}{\text{cell day}} \right)$	$\frac{\tau k}{a_{max}} \delta_c$
ρ	$\frac{\ln 2}{\tau} \left(\frac{1}{\text{day}} \right)$	$\tau \rho / T_c$	δ_h	$1.43 \cdot 10^{-12} \left(\frac{\text{mmol}}{\text{cell day}} \right)$	$\frac{\tau k}{a_{max}} \delta_h$
γ	$0.05 \left(\frac{1}{\text{day}} \right)$	$\tau \gamma$	β	$\frac{\rho}{10} \left(\frac{1}{\text{day}} \right)$	$\frac{\rho}{10}$
a_n	$0 \left(\frac{1}{\text{day}} \right)$	0	D, D_v	$10^{-11} \left(\frac{\text{cm}^2}{\text{s}} \right)$	$\frac{\tau}{L^2} D$
a_h	$\frac{\rho}{20} \left(\frac{1}{\text{day}} \right)$	$\frac{\rho}{20}$	χ_v	$9.36 \cdot 10^{-7} \left(\frac{1}{\text{day}} \right)$	$\frac{\tau}{L^2} \chi_v$
D_a	$2.9 \cdot 10^{-7} \left(\frac{\text{cm}^2}{\text{s}} \right)$	$\frac{\tau}{L^2} D_a$	λ	$\frac{\ln 2}{64} \left(\frac{1}{\text{min}} \right)$	$\tau \lambda$
K_m	$5.75 \cdot 10^{-7} \left(\frac{\text{mmol}}{\text{cm}^3} \right)$	$\frac{K_m}{a_{max}}$	ω	$2.17 \cdot 10^{-6} \left(\frac{1}{\text{cell day}} \right)$	$\tau k \omega$
μ	$\frac{\ln 2}{15} \left(\frac{1}{\text{day}} \right)$	$\tau \mu$			

Table 13 - The parameters for PIHNA model simulation and their nondimensionalized versions

As described in the previous section, the reconstructed tumor can provide information regarding the spatial concentration of the viable HeLa cell population at the time of measurement and produce the growth curve of the specific tumor. As shown in Figure 75a, we first initialized the spatial concentration of the normoxic cells according to the fluorescence information of a 2D-depth slice assuming that the concentration of the hypoxic cells can be neglected in the initial step. The fluorescence intensity was normalized in a way to force the peak of the concentration to reach 1. In addition to that, a multivariate normal distribution (Figure 75c) has also been used to approximate the initial spatial distribution of normoxic cells. The rest initial normalized populations were uniformly set at $h_0 = 0$, $n_0 = 0$, $a_0 = 0$ and $v_0 = 0.005$. Tumor growth has been simulated for 12 fictitious days.

Before feeding the model with parameters, they were nondimensionalized according the formulas shown in Table 13. The new positions \hat{x} are found according to $\hat{x} = \frac{x}{L}$ and the time is changed to $\hat{t} = \frac{t}{\tau}$. Lastly, the concentration c, h, n and v of normoxic, hypoxic, necrotic and endothelial cells, respectively, is nondimensionalized according to the capacity of cells $k = 2.39 \cdot 10^8 \frac{cells}{cm^3}$, thus $\hat{c} = \frac{c}{k}, \hat{h} = \frac{h}{k}, \hat{n} = \frac{n}{k}$ and $\hat{v} = \frac{v}{k}$. Similarly, the maximum value of angiogenesis is altered according to the formula $\hat{a} = \frac{a}{a_{max}}$, where $a_{max} = 5.75 \cdot 10^{-6} \frac{mmol}{cm^3}$.

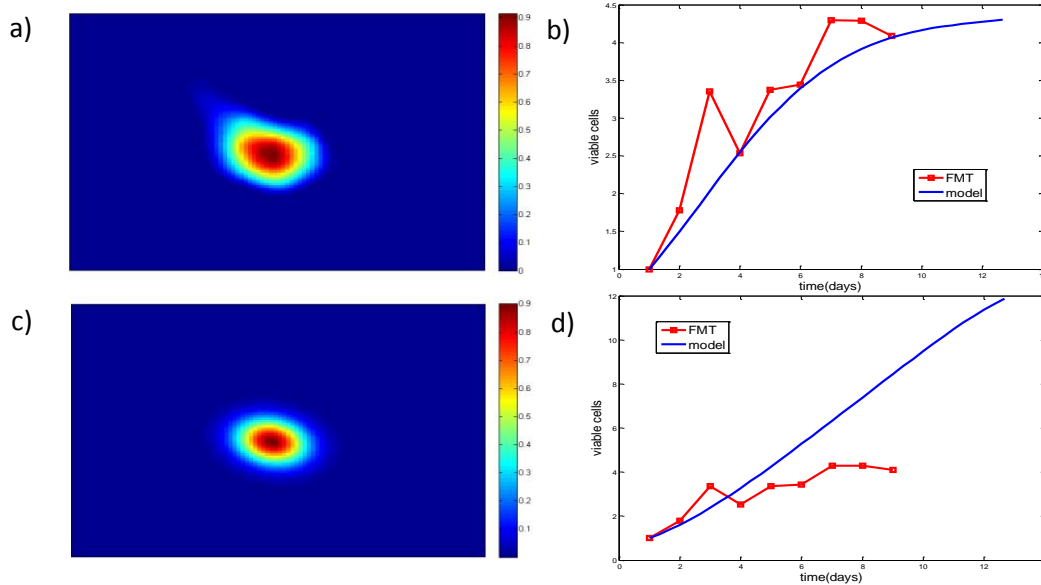


Figure 75 - a) The initial distribution of normoxic cells used in simulations as obtained from a depth slice of the 3D fluorescence reconstruction and **b)** the corresponding tumor growth over timeas predicted by the in silico model (blue line)and as measured from the in vivo data (red line). **c)** A multivariate normal distribution approximates the initial normoxic concentration and **d)** the corresponding in silico prediction of tumor growth (blue line) compared with the in vivo data (red line).

As can be seen in Figure 75, initializing the cancer cell population according to the in-vivo imaging data (Figure 75a), the viable cancer cell population is in line with the in-vivo observations and well approximates the fast growth of the first days and the following slowdown phase of tumor cells (Figure 75b). Interestingly, as can be seen in Figure 76b the size and shape predictions of the final tumor are very similar to the ex-vivo data (Figure 76a). Specifically, the diameter of the real tumor has grown from 0.4cm on day 9 (first day of measurements) to 0.7cm on day 17, while the simulated final tumor has a diameter of 0.68cm. On the contrary, as can be seen in Figure 75d the normal distribution (Figure 75c) is unable to approximate the slowdown phase of tumor growth that is observed in vivo under the same set of parameters neither can predict the size and shape of the real tumor (Figure 76c). ■

Summary

The simulations show the importance of proper initialization in predicting the evolution of tumor. It is observed that the shape of the initial cancer strongly affects the shape of the simulated tumor, thus it is very important to appropriately initialize normoxic populations

according to clinical data. In simulations, where normoxic population has been initialized according to real data, it is observed that the eventual shape is similar to real final tumor. Moreover, the model has succeeded in approaching the real final tumor diameter. More specifically, the real tumor diameter has increased 42.86%, while the simulated has increased 44.12%.

In order to evaluate the robustness and response behavior of the model, we also tested it against a variety of parameter values including the dispersal rate of HeLa cells, the rate at which normoxic cells convert to hypoxic under inadequate oxygen, the relative amount of vasculature supplying the tissue. This analysis has revealed that a low motility rate is important for the tumor growth to reach a plateau, an increased cellular proliferation rate leads to a faster onset of growth and that the level of vascularization must be significantly high to slow down the conversion of normoxic cells to hypoxic and eventually to necrotic. Furthermore, the simulations suggest that space competition is a key determinant for explaining the growth behavior of the tumor under study, although oxygen competition among cancer cells can also be important when different metabolic demands are considered.

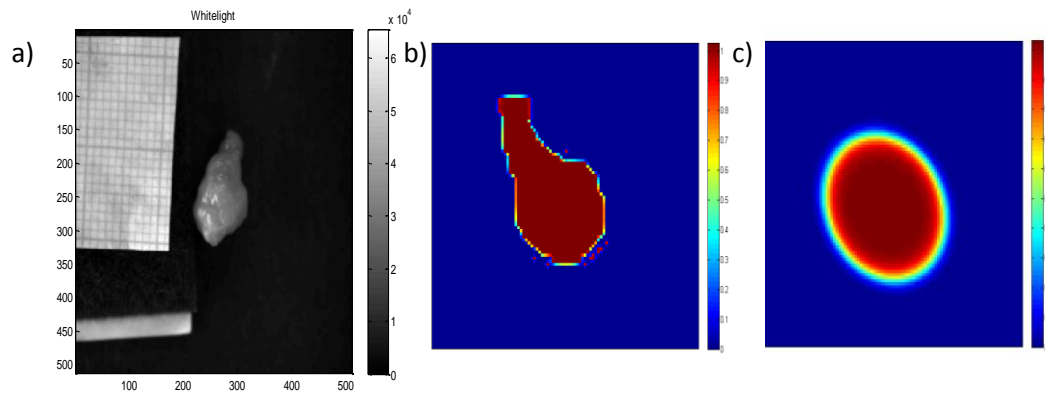


Figure 76 - a) white light image showing the tumor the day the mouse was sacrificed (day 17). The tumor is approximately 7mm in diameter. b) initialized with the distribution of Figure 75a, the *in silico* tumor approximates the *in vivo* tumor morphology and the predicted tumor size is approximately 6.8mm in diameter after 9 fictitious days contrary to c) the *in silico* tumor, which was initialized with the distribution of Figure 75c.

General Conclusions

Up to now, the various implementations of Diffusive models lack a firm mathematical background on the derivation of the system, with concrete assumptions on the approximation scheme. When designing a model, engineers should not ignore the computational limitations of the model. The processing power and storage capacity of the computers that are used in clinical practice should be seriously taken into account, since a resource-demanding model would turn out to be cumbersome when no access to supercomputers is possible.

The results of this thesis indicate that even if one method (e.g. Finite Elements) would initially seem as the most accurate, this work indicates specific tradeoffs (such as simulation time, storage and computational needs) that can cause computational problems on the main-stream computers of hospitals and may alter the preference to this method. This is something that should be studied more thoroughly with other techniques, such as Finite Volumes or some “smarter” modalities of Finite Elements.

The evaluation of the schemes used for solving the diffusion – reaction equation uses solid metrics and provides objective comparison (JC, DS, VS metrics). It is essential to study how these metrics fluctuate depending on the ground truth annotation; the ground truth is an imaging session delineated by the clinician. Especially for glioma, clinicians have to guess where the cancerous area is, as the tumor is invisible.

One aspect not thoroughly studied here, although introduced, is the effect of tumor growth to the mass deformation of the brain. This deformation is likely to affect the model, as the areas of white and gray matter, and the white fiber tracts have been moved.

Moreover, the reported cases in this work do not show mass effect, nor the characteristic diffusive fingers of glioblastoma, which should be further studied with larger and more aggressive gliomas.

The first approach of setting a non-zero diffusion coefficient to CSF, which has been followed here, has not yet been studied in depth for real cases where CSF invasion has been diagnosed by radiologists. For these cases it would be interesting to study if fluid dynamics could better approximate the migration of cells in CSF and simulate solid/fluid structure interaction.

The simulations for PIHNA model show the importance of proper initialization in predicting the evolution of tumor. It is observed that the shape of the initial cancer strongly affects the shape of the simulated tumor, thus it is very important to appropriately initialize normoxic populations according to clinical data. In simulations, where normoxic population has been initialized according to real data, it is observed that the eventual shape is similar to real final tumor. A very crucial space for study here is the interpretation (mapping) of MRIs to cancerous cell populations and their initialization.

In order to evaluate the robustness and response behavior of the PIHNA model, we also tested it against a variety of parameter values including the dispersal rate of HeLa cells, the rate at which normoxic cells convert to hypoxic under inadequate oxygen, the relative amount of vasculature supplying the tissue. This analysis has revealed that a low motility rate is important for the tumor growth to reach a plateau, an increased cellular proliferation rate leads to a faster onset of growth and that the level of vascularization must be significantly high to slow down the conversion of normoxic cells to hypoxic and eventually to necrotic. Furthermore, the simulations suggest that space competition is a key determinant for explaining the growth behavior of the tumor under study, although oxygen competition among cancer cells can also be important when different metabolic demands are considered. All these observations have to be studied and verified in more detail.

Bibliography

- [1] CancerHelp UK, "How many different types of cancer are there?," 2012.
- [2] P. Anand, A. B. Kunnumakara, C. Sundaram, K. B. Harikumar, S. T. Tharakan, O. S. Lai, B. Sung and B. B. Aggarwal, "Cancer is a Preventable Disease that Requires Major Lifestyle Changes," *Pharmaceutical Research*, vol. 25, no. 9, pp. 2097-2116, September 2008.
- [3] B. Vogelstein and K. W. Kinzler, "Introduction," in *The Genetic Basis of Human Cancer*, 2nd Edition ed., New York, McGraw Hill Professional, 2012, p. 5.
- [4] A. Montazeri, "Quality of life data as prognostic indicators of survival in cancer patients: an overview of the literature from 1982 to 2008," *Health Quality Life Outcomes* 7, December 2009.
- [5] A. Bishop, "Earth Times," 13 September 2012. [Online]. Available: <http://www.earthtimes.org/health/lung-cancer-tumours-smokers-10-times-genetic-mutations/2177/>. [Accessed 4 January 2013].
- [6] World Health Organization, "WHO," [Online]. Available: <http://www.who.int/mediacentre/factsheets/fs297>. [Accessed 5 February 2013].
- [7] P. Boyle and B. Levin, *World Cancer Report 2008*, IARC, 2008.
- [8] American Brain Association, "Brain Tumors," [Online]. Available: <http://www.abta.org>. [Accessed 2 11 2012].
- [9] Natioanl Cancer Institute, *What You Need To Know About™ Brain Tumors*, 09-1558 ed., NIH, 2009.
- [10] J. Leighton and R. Tcho, "The propagation of cancer, a process of tissue remodeling," *Cancer and Metastasis Reviews*, vol. 3, no. 2, pp. 81-97, 1984.
- [11] A. N. Mamelak and D. B. Jacoby, "Targeted delivery of antitumoral therapy to glioma and other malignancies with synthetic chlorotoxin (TM-601)," *Tachnology Evaluation*, vol. 4, no. 2, pp. 175-186, March 2007.
- [12] M. L. Goodenberrger and R. B. Jenkins, "Genetics of adult glioma," *Cancer Genetics*, vol. 205, no. 12, pp. 613-621, December 2012.
- [13] CBTRUS, "Statistical Report: Primary Brain Tumors in the United States, 1992-1997," Central Brain Tumor Registry of the United States, Chicago, 2000.
- [14] M. Manske, "Glioma," [Online]. Available: <http://www.wikipedia.org/wiki/Glioma>.

[Accessed 5 February 2013].

- [15] M. Tovi, "MR imaging in cerebral gliomas analysis of tumour tissue components," *Acta Radiologica*, vol. 384, pp. 1-24, 1993.
- [16] S. J. Price, N. G. Burnet, T. Donovan, H. A. L. Green, A. Peña, M. Antoun, J. D. Pickard, A. T. Carpenter and J. H. Gillard, "Diffusion tensor imaging of brain tumours at 3T: a potential tool for assessing white matter tract invasion?," *Clinical Radiology*, vol. 58, no. 6, pp. 455-462, 2003.
- [17] E. G. Van Meir, C. G. Hadjipanayis, A. D. Norden, H.-K. Shu, P. Y. Wen and J. J. Olson, "Exciting New Advances in Neuro-Oncology," *A Cancer Journal for Clinicians*, vol. 60, no. 3, pp. 166-193, May 2010.
- [18] P. Lissoni, S. Meregalli, L. Nosetto, S. Barni, G. Tancini, G. Fossati and G. Maestroni, "Increased Survival Time in Brain Glioblastomas by a Radioneuroendocrine Strategy with Radiotherapy plus Melatonin Compared to Radiotherapy Alone," *Oncology*, vol. 53, pp. 43-46, 1996.
- [19] D. Krex, B. Klink, C. Hartmann, A. Von Deimling, T. Pietsch, M. Simon, M. Sabel and J. P. Steinbach, "Long term survival with glioblastoma multiforme," *Brain*, vol. 130, no. 10, pp. 2596-2606, 2007.
- [20] Los Angeles Neuro-Oncology, "How our patients perform: Glioblastoma Multiforme [GBM]," [Online]. Available: neurooncology.ucla.edu. [Accessed 3 February 2013].
- [21] D. Silbergerld, E. Alvord and J. Murray, "The cause of death in patients with glioblastoma is multifactorial: Clinical factors and autopsy findings in 117 cases of suprantentorial glioblastoma in adults," *Neuro Oncology*, vol. 10, no. 1, pp. 179-185, 1991.
- [22] D. Krex, B. Klink, C. Hartmann, A. Von Deimling, T. Pietsch, M. Simon, M. Sabel, J. P. Steinbach, O. Heese, G. Reifenberger, M. Weller and G. Schackert, "Long-term survival with glioblastoma multiforme," *Brain*, vol. 130, no. 10, pp. 2596-2606, 4 September 2007.
- [23] "Glioblastoma Multiforme," [Online]. Available: http://en.wikipedia.org/wiki/Glioblastoma_multiforme. [Accessed 13 February 2013].
- [24] H. Ohgaki and P. Kleihues, "Population-based studies on incidence, survival rates, and genetic alterations in astrocytic and oligodendroglial gliomas," *Journal of neuropathology and experimental neurology*, vol. 64, no. 6, pp. 479-489, June 2005.
- [25] L. Baglietto, G. G. Giles, D. R. English, A. Karahalios, J. L. Hopper and G. Severi, "Alcohol consumption and risk of glioblastoma; evidence from the Melbourne collaborative cohort study," *International Journal of Cancer*, vol. 128, no. 8, pp. 1929-

1934, 15 April 2001.

- [26] R. A. Vilchez, C. A. Kozinetz, A. S. Arrington, C. R. Madden and J. S. Butel, "Simian virus 40 in human cancers," *The American Journal of Medicine*, vol. 114, no. 8, pp. 675-684, 1 June 2003.
- [27] D. Mitchell, "Target acquired," 29 May 2008. [Online]. Available: The Economist. [Accessed 23 January 2013].
- [28] E. Van Wijngaarden and M. Dosemeci, "Findings from the National Longitudinal Mortality Study, 1979–1989," *International Journal of Cancer*, vol. 119, no. 5, pp. 1136-1144, 2006.
- [29] J. G. Smirniotopoulos, F. M. Murphy, E. J. Rushing, J. H. Rees and J. W. Schroeder, "Patterns of Contrast Enhancement in the Brain and Meninges," *RadioGraphics*, vol. 27, no. 1, pp. 525-551, March 2007.
- [30] C. Daumas - Duport, B. W. Scheithauer and P. J. Kelly, "A Histologic and Cytologic Method for the Spatial Definition of Gliomas," in *Mayo Clinic Proceedings*, 1987.
- [31] P. Black and P. Wen, *Clinical imaging, and laboratory diagnosis of brain tumors*, New York: Churchill Livingstone, 1995.
- [32] M. Kounelakis, E. Blazadonakis, M. Zervakis and X. Kotsiakis, "The Impact of Bioinformatics in Clinical Practices on Human Cancer," in *Proceedings of the European Conference on Emergent Aspects in Clinical Data Analysis (EACDA 2005)*, Pisa, 2005.
- [33] NASA, "X-Rays," [Online]. Available: http://missionscience.nasa.gov/ems/11_xrays.html. [Accessed 6 February 2013].
- [34] G. T. Herman, *Fundamentals of computerized tomography: Image reconstruction from projection*, 2nd Edition ed., Springer, 2009.
- [35] Radiology Info, "Computed tomography (CT) Angiography," [Online]. Available: http://www.radiologyinfo.org/en/info.cfm?pg=angiact#part_one. [Accessed 6 February 2013].
- [36] MrTip, "MRI of the Skull Base," [Online]. Available: <http://www.mr-tip.com/serv1.php?type=slider&slide=MRI%20of%20the%20Skull%20Base>. [Accessed 6 February 2013].
- [37] R. A. Novelline and L. F. Squire, *Squire's Fundamentals of Radiology*, 6th ed., Harvard University Press, 2004.
- [38] G. Doherty, *Current diagnosis and treatment: surgery*, New York: The McGraw-Hill Companies, 2010.

- [39] R. R. Smith, "Brain stem tumors," *Seminars in Roentgenology*, vol. 25, no. 3, pp. 249-262, July 1990.
- [40] J. B. M. Wantjes, "Magnetic Resonance Imaging of the future will show brain structures automatically in PACS," 23 October 2009. [Online]. Available: <http://newsroom.sectra.com/2009/10/magnetic-resonance-imaging-of-the-future-will-show-brain-structures-automatically-in-pacs/>. [Accessed 7 February 2013].
- [41] R. Freeman, *Spin Choreography: Basic Steps in High Resolution NMR*, Oxford University Press, 1999.
- [42] B. De Coene, J. V. Hajnal, P. Gatehouse, D. B. Longmore, S. J. White, A. Oatridge, J. M. Pennock, I. R. Young and G. M. Bydder, "MR of the brain using fluid-attenuated inversion recovery (FLAIR) pulse sequences," *American Journal of neuroradiology*, vol. 13, no. 6, pp. 1555-1564, November 1992.
- [43] D. Le Bihan, E. Breton, D. Lallemand, P. Grenier, E. Cabanis and M. Laval - Jeantet, "MR imaging of intravoxel incoherent motions: Application to diffusion and perfusion in neurologic disorders," *Radiology*, vol. 161, no. 2, pp. 401-407, November 1986.
- [44] G. A. Filler, "The History, Development and Impact of Computed Imaging in Neurological Diagnosis and Neurosurgery: CT, MRI, and DTI," *Internet Journal of Neurosurgery*, May 2010.
- [45] Karczmar, Roman, Halpern and Pan, "Algorithm Development of Fast Spin Resonance Imaging," University of Chicago, [Online]. Available: <http://medicalphysics.uchicago.edu/research>. [Accessed 7 February 2013].
- [46] M. Van der Graaf, "In vivo magnetic resonance spectroscopy: basic methodology and clinical applications," *European Biophysics Journal*, vol. 39, no. 4, pp. 527-540, 13 August 2009.
- [47] J. R. Petrella and J. M. Provenzale, "MR Perfusion Imaging of the Brain: Techniques and Applications," *American Journal of Roentgenology*, vol. 175, no. 1, pp. 207-219, July 2000.
- [48] R. Hustinx and A. Alavi, "SPECT and PET imaging of brain tumors," *Neuroimaging clinics of North America*, vol. 9, no. 4, pp. 751-766, November 1999.
- [49] Wikipedia, "Positron emission tomography," [Online]. Available: http://en.wikipedia.org/wiki/Positron_emission_tomography. [Accessed 7 February 2013].
- [50] Lakeridge Health, "Interventional Radiology and Women's Health," [Online]. Available: www.lakeridgehealth.on.ca/patient_care/interventional_radiology/presentations/rad

iology.

- [51] K. R. Swanson, L. D. True and J. D. Murray, "On the Use of Quantitative Modeling to Help Understand Prostate-Specific Antigen Dynamics and Other Medical Problems," *American Journal of Clinical Pathology*, vol. 119, no. 1, pp. 14-17, January 2003.
- [52] P. Tracqui, "From passive diffusion to active cellular migration in mathematical models of tumour invasion," *Acta Bibliothetica*, vol. 43, no. 1, pp. 443-464, 1995.
- [53] A. Roniotis, K. Marias, V. Sakkalis and M. Zervakis, "Diffusive modeling of glioma evolution: a review," *Journal of Biomedical Science and Engineering*, vol. 3, no. 1, pp. 501-508, May 2010.
- [54] P. K. Burgess, P. M. Kulesa, J. D. Murray and E. J. C. Alvord, "The interaction of growth rates and diffusion coefficients in a three- dimensional mathematical model of gliomas," *Journal of Neuropathology and Experimental Neurology*, vol. 56, no. 6, pp. 704-713, June 1997.
- [55] J. A. Adam and S. A. Maggelakis, "Diffusion regulated growth characteristics of a spherical prevascular carcinoma," *Bulletin of Mathematical Biology*, vol. 52, no. 4, pp. 549-582, 1990.
- [56] T. E. Wheldon, "Mathematical models in experimental and clinical oncology," in *Mathematical Methods in Medicine*, Wiley & Sons, 1986, pp. 1-32.
- [57] R. Lefever, J. Hiemaux and P. Meyers, "Evolution of tumours attacked by immune cytotoxic cells: the immune response dilemma," in *Cell to cell Signaling: From experiments to Theoretical Models*, Academic Press, 1989, pp. 315-333.
- [58] J. A. Sheratt and M. A. Nowa, "Oncogenes, anti-oncogenes and the immune response to cancer a mathematical model," in *Proceedings. Biological Sciences, The Royal Society*, London, 1992.
- [59] D. Silbergeld, R. Rostomily and J. Alvord, "The cause of death in patients with glioblastoma is multifactorial: Clinical factors and autopsy findings in 117 cases of supratentorial glioblastoma in adults," *Journal of Neurology and Oncology*, vol. 10, no. 1, pp. 179-185, 1991.
- [60] A. Claes, A. Idema and P. Wesseling, "Diffusive glioma growth: a guerilla war," *Acta Neuropathology*, vol. 114, no. 5, pp. 443-458, 2007.
- [61] S. Toms, W. Lin, R. Weil, M. Johnson, E. Jansen and A. Mahadevan-Jansen, "Intraoperative optical spectroscopy identifies infiltrating glioma margins with high sensitivity," *Neurosurgery*, vol. 57, no. 4, pp. 382-391, 2005.
- [62] F. G. Blakenberg, R. L. Teplitz, W. Ellis, M. S. Salamat, B. H. Min and L. Hall, "The

- influence of volumetric tumor doubling time, DNA ploidy, and histologic grade on the survival of patients with interracial astrocytomas," *American Journal of Neuroradiology*, vol. 16, no. 16, pp. 1001-1012, 1995.
- [63] H. Frieboes, X. Zheng, C. H. Sun, B. Tromberg, R. Gatenby and V. Cristini, "An Integrated Computational/Experimental Model of Tumor Invasion," *Cancer Research*, vol. 66, p. 1597, 1 February 2006.
- [64] S. Sjöström, U. Andresson, Y. Liu, T. Brännström, H. Broholm, C. Johansen, H. collarz - Laier, R. Henriksson, M. Bondy and B. Melin, "Genetic variations in EGF and EGFR and glioblastoma outcome," *Neuro Oncology*, vol. 34, no. 2, pp. 815-821, 2010.
- [65] V. Cristini and J. Lowengrub, "Nonlinear simulation of tumor growth," *Journal of Mathematical Biology*, vol. 12, no. 8, pp. 114-224, 2003.
- [66] T. Deiboeck, M. Berens, A. Kansal, S. Torquato, A. Stemmer-Rachamimov and E. Chiocca, "Pattern of self-organization in tumour systems: complex growth dynamics in a novel brain tumour spheroid model," *Cell Proliferation*, vol. 34, no. 2, pp. 115-134, 2001.
- [67] D. Drasdo and S. Höhme, "A single-cell-based model of tumor growth in vitro: monolayers and spheroids," *Physical Biology*, vol. 2, no. 3, pp. 133-147, 12 July 2005.
- [68] D. Dionysiou, G. S. Stamatakos, N. K. Uzunoglu, K. S. Nikita and A. Marioli, "A four-dimensional simulation model of tumour response to radiotherapy in vivo: parametric validation considering radiosensitivity, genetic profile and fractionation," *Journal of Theoretical Biology*, vol. 230, no. 1, pp. 1-20, September 2004.
- [69] K. Swanson, E. Alvord and J. Murray, "A Quantitative Model for Differential Motility of Gliomas in Grey and White Matter," *Cell Proliferation*, vol. 33, no. 5, pp. 317-330, 2000.
- [70] S. Jbabdi, E. Mandonnet, H. Duffau, L. Capelle, K. R. Swanson, M. Pelegriani-Issac, R. Guillemin and H. Benali, "Simulation of anisotropic growth of low-grade gliomas using diffusion tensor imaging," *Magnetic Resonance in Medicine*, vol. 54, no. 3, pp. 616-624, September 2005.
- [71] G. S. Stamatakos, E. A. Kolokotroni, D. Dionysiou, E. Georgiadi and C. Desmedt, "An advanced discrete state - discrete event multiscale simulation model of the response of a solid tumor to chemotherapy: Mimicking a clinical study," *Journal of Theoretical Biology*, vol. 266, no. 1, pp. 124-139, September 2010.
- [72] O. Clatz, M. Sermesant, P.-Y. Bondiau, H. Delingette, S. K. Warfield, G. Malandain and N. Ayache, "Realistic simulation of the 3-D growth of brain tumours in MR images coupling diffusion with biomechanical deformation," *IEEE Transactions in Medical*

Imaging, vol. 24, no. 10, pp. 1334-1346, October 2005.

- [73] E. Konukoglu, O. Clatz, B. Menze, M. A. Weber, B. Stieltjes, E. Mandonnet, H. Delingette and N. Ayache, "Image Guided Personalization of Reaction Diffusion Type Tumor Growth Models using Modified Anisotropic Eikonal Equations," *IEEE Transactions on Medical Imaging*, vol. 29, no. 1, pp. 77-95, 2010.
- [74] C. Hogeia, C. Davatzikos and G. Biros, "Modeling glioma growth and mass effect in 3D MR images of the brain," in *Medical Image Computing and Computer Assisted Intervention*, 642-650, 2007.
- [75] A. R. Kansal, S. Torquatto, G. R. Harsh, E. Chiocca and T. Deisboeck, "Simulated brain tumor growth dynamics using a three-dimensional cellular automaton," *Journal of Theoretical Biology*, vol. 203, no. 4, pp. 367-382, April 2000.
- [76] A. Zizzari, *Methods on Tumor Recognition and Planning Target Prediction for the Radiotherapy of Cancer*, Thesis: University of Magdenburg, 2004.
- [77] M. Tabatabai, D. Williams and Z. Bursac, "Hyperbolic growth models: theory and application," *Theoretical Biology and Medical Modelling*, vol. 2, no. 1, p. 14, 2005.
- [78] J. D. Murray, *Mathematical Biology*, Heidelberg: Springer - Verlag, 1989.
- [79] M. Marusic, Z. Bajzer, J. P. Freyer and S. Vuk-Palovic, "Analysis of growth of multicellular tumour spheroids by mathematical models," *Cell Proliferation*, vol. 27, no. 2, pp. 73-94, February 1994.
- [80] H. L. Harpold, E. Alvord and K. R. Swanson, "Visualizing beyond the tip of the iceberg: The evolution of mathematical modeling of glioma growth and invasion," *Journal of Neuropathology and Experimental Neurology*, vol. 66, no. 1, pp. 1-9, 2007.
- [81] G. Powathil, M. Kohandel, A. Oza and M. Milosevic, "Mathematical modeling of brain tumours: effects of radiotherapy and chemotherapy," *Physics in Medicine and Biology*, vol. 52, no. 11, pp. 3291-3306, 2007.
- [82] J. Cook, D. E. Woodward, P. Tracqui and J. D. Murray, "Resection of gliomas and life expectancy," *Journal of Neuro-Oncology*, vol. 24, no. 1, pp. 131-146, 1995.
- [83] D. E. Woodward, J. Cook, P. Tracqui, G. C. Cruywagen, J. D. Murray and E. C. Alvord Jr, "A mathematical model of glioma growth: the effect of extent of surgical resection," *Cell Proliferation*, vol. 29, no. 6, pp. 269-288, June 1996.
- [84] J. D. Murray, *Mathematical biology I and II; interdisciplinary applied mathematics*, 3rd ed., Berlin: Springer, 2006.
- [85] R. Stupp, W. Mason, M. van den Bent, M. Weller, B. Fisher, M. Taphoon, K. Belanger, A. Brandes, C. Marosi, U. Bogdahn, J. Curschmann, R. Janzer, S. Ludwin, T. Gorlia, A.

- Allgeier, D. Lacombe, G. Cairncross, E. Eisenhauer and R. Minimanoff, "Radiotherapy plus concomitant and adjuvant Temozolomide for glioblastoma," *The New England Journal of Medicine*, vol. 352, no. 1, pp. 987-996, 10 March 2005.
- [86] M. Walker, T. Strike and G. Sheline, "An analysis of dose-effect relationship in the radiotherapy of malignant Gliomas," *International Journal of Radiation Oncology*Biophysics* Physics*, vol. 5, no. 10, pp. 1725-1731, October 1979.
- [87] M. Werner-Wasik, C. B. Scott, D. F. Nelson, L. E. Gaspar, K. J. Murray, J. A. Fischbach, J. S. Nelson, A. S. Weinstein and W. J. Curran Jr, "Final report of a phase I/II trial of hyperfractionated and accelerated hyperfractionated radiation therapy with carmustine for adults with supratentorial malignant gliomas. Radiation Therapy Oncology Group Study 83-02," *Cancer*, vol. 77, no. 8, pp. 1535-1543, April 1996.
- [88] E. Mandonnet, J. Y. Delattre, M. L. Tanguy, K. R. Swanson, A. F. Carpentier, H. Duffau, P. Cornu, R. Van Effenterre, E. C. Alvord and L. Capelle, "Continuous growth of mean tumour diameter in a subset of grade II gliomas," *Annals of Neurology*, vol. 53, no. 4, pp. 524-528, April 2003.
- [89] A. Giese and M. Westphal, "Glioma Invasion in the Central Nervous System," *Neurosurgery*, vol. 39, no. 2, pp. 250-252, August 1996.
- [90] A. Giese, R. Bjerkviq, M. E. Berens and M. Westphal, "Cost of Migration: Invasion of Malignant Gliomas and Implications for Treatment," *Journal of Clinical Oncology*, vol. 21, no. 8, pp. 1624-1636, 15 April 2003.
- [91] BrainWeb, "Simulated Brain Database," 1996. [Online]. Available: <http://brainweb.bic.mni.mcgill.ca/brainweb/>. [Accessed 12 February 2013].
- [92] C. A. Cocosco, V. Kollokian, R. K.-S. Kwan, G. B. Pike and A. C. Evans, "Brainweb: Online interface to a 3D simulated brain database," *NeuroImage*, vol. 5, p. 425, 1997.
- [93] T. Conturo, N. Lori, T. Cull, E. Akbudal, A. Snyder, J. Shimony, J. McKinstry, R. Burton and M. Raichle, "Tracking neuronal pathways in the living human brain," *Proceedings of the National Academy of Sciences of the United States of America*, vol. 96, no. 18, pp. 10422-10427, 31 August 1999.
- [94] A. Roniotis, "Glioma Growth Modeling," Heraklion, Crete, 2010.
- [95] K. Marias, D. Dionysiou, V. Sakkalis, N. Graf, R. M. Bohle, P. V. Coveney, S. Wan, A. Folarin, P. Buchler, M. Reyes, G. Clapworthy, E. Liu, J. Sabczynski, T. Bily, A. Roniotis, M. Tsiknakis, E. Kolokotroni, S. Giatili, C. Veith, E. Messe, H. Stenzhorn, Y.-J. Kim, S. Zasada, A. N. Haidar, C. May, S. Bauer, T. Wang, Y. Zhao, M. Karasek, R. Grewer, A. Franz and G. S. Stamatakis, "Clinically Oriented Translational Cancer Multilevel Modeling: The ContraCancrum project," in *World Congress of Medical Physics and*

Biomedical Engineering, Munich, 2011.

- [96] A. Fick, "Quantitative laws of Diffusion," *Philosophical Magazine*, 1855.
- [97] S. Puwal and B. J. Roth, "Forward Euler Stability of the Bidomain Model of Cardiac Tissue," *IEEE Transactions on Biomedical Engineering*, vol. 54, no. 5, pp. 951-953, May 2007.
- [98] W. H. Press, S. A. Teukolsky, W. T. Vetterling and B. P. Flannery, *Numerical Recipes in C++*, 2nd ed., Cambridge: Cambridge University Press, 2002.
- [99] A. Roniotis, K. Marias, V. Sakkalis, G. D. Tsididis and M. Zervakis, "A Complete Mathematical Study of a 3D Model of Heterogeneous and Anisotropic Glioma Evolution," in *Conference Proceedings: Annual Iternation Conference of the IEEE Engineering in Medicine and Biology Society*, Minneapolis, 2009.
- [100] J. Crank, *The Mathematics of Diffusion*, 2nd ed., New York: Oxford University Press, 1975.
- [101] Y. Saad, *Iterative methods for sparse linear systems*, 2nd ed., Philadelphia: S.I.A.M., 2003.
- [102] "The Whole Atlas Brain," [Online]. Available: <http://www.med.harvard.edu/AANLIB/home.html>. [Accessed 14 December 2008].
- [103] R. A. Bammer and M. E. Moseley, "In vivo MR tractography using diffusion imaging," *European Journal of Radiology*, vol. 45, no. 3, pp. 223-234, 2002.
- [104] T. Rohlfing, N. M. Zahr, E. V. Sullivan and A. Pfefferbaum, "The SRI24 multichannel atlas of normal adult human brain structure," *Human brain mapping*, vol. 31, no. 5, pp. 798-819, 2010.
- [105] R. Cardenes, M. Bach, Y. Chi, I. Marras, R. Luis, M. Andersson, P. Cashman and M. Bultelle, "Multimodal evaluation for medical image segmentation," in *CAIP*, 2007.
- [106] K. Onda, K. Tanaka, R. Takahashi, H. Takeda and N. Ikuta, "Symptomatic cerebrospinal fluid dissemination of cerebral glioblastoma. Computed tomographic findings in 11 cases," *Neuroradiology*, vol. 32, no. 2, pp. 146-150, 1990.
- [107] G. Dohrmann, J. Farwell and J. Flannery, "Glioblastoma multiforme in children," *Joiurnal of Neurosurgery*, vol. 44, pp. 442-448, 1976.
- [108] T. Rohlfing, "SRI atlas," [Online]. Available: <http://nitrc.org/projects/sri24>.
- [109] K. Saladin, "Anatomy & Physiology," in *The Unit of Form adn Function*, 5th ed., New York, McGraw-Hill, 2007, pp. 451-490.

- [110] "MIPAV," [Online]. Available: <http://mipav.cit.nih.gov>. [Accessed May 2012].
- [111] S. Smith, "Fast robust automated brain extraction," *Human Brain Mapping*, vol. 17, no. 3, pp. 143-155, November 2002.
- [112] Foundation for Research and Technology - Hellas, "FORTH - Biomodeling Group," FORTH, 2010. [Online]. Available: <http://biomodeling.ics.forth.gr>. [Accessed May 2012].
- [113] E. Skounakis, C. Farmaki, V. Sakkalis, A. Roniotis, K. Banitsas, N. Graf and K. Marias, "DoctorEye: A Clinically Driven Multifunctional Platform for Accurate Processing of Tumors in Medical Images," *The Open Medical Informatics Journal*, vol. 4, pp. 105-115, 2010.
- [114] R. Rockne, J. K. Rockhill, M. Mrugala, A. M. Spence, I. Kalet, K. Hendrickson, A. Lai, T. Cloughesy, E. C. Alvord and K. R. Swanson, "Predicting the efficacy of radiotherapy in individual glioblastoma patients in vivo: a mathematical modeling approach," *Physics in Medicine and Biology*, vol. 55, no. 12, pp. 3271-3285, June 2010.
- [115] G. Steel, *Basic Clinical Radiobiology*, 3rd ed., London: Arnold, 2002.
- [116] E. Hall, *Radiobiology for the Radiologist*, Philadelphia: J B Lippincott, 1994.
- [117] M. Partridge, M. Ramos, A. Sardaro and M. Brada, "Dose escalation for non-small cell lung cancer: analysis and modelling of published literature," *Radiotherapy and Oncology*, vol. 99, no. 1, pp. 6-11, 30 March 2011.
- [118] G. Kantor, H. Loiseau, A. Vital and J. J. Mazon, "Gross tumor volume (GTV) and clinical target volume (CTV) in adult gliomas," *Canver Radiotherapy*, vol. 5, no. 5, pp. 571-580, October 2001.
- [119] K. R. Swanson, R. C. Rockne, J. Claridge, M. Chaplain, E. C. Alvord Jr and A. Andersson, "Quantifying the role of angiogenesis in malignant progression of gliomas: In Silico modeling integrates imaging and histology," *Cancer Research*, vol. 71, no. 24, pp. 7366-7375, December 2011.
- [120] R. Weissleder and M. J. Pittet, "Imaging in the era of molecular imaging," *Nature*, vol. 452, no. 7187, pp. 580-589, April 2008.
- [121] T. F. Massoud and S. S. Gambhir, "Integrating noninvasive molecular imaging into molecular medicine: an evolving paradigm," *Trends in Molecular Medicine*, vol. 13, no. 5, pp. 183-191, 1 May 2007.
- [122] G. Zacharakis, H. Kambara, H. Shih, J. Ripoll, J. Grimm, Y. Saeki, R. Weissleder and V. Ntziachristos, "Volumetric tomography of fluorescent proteins through small animals in vivo," in *Proceedings of the National Academy of Sciences of United States of*

America, 2005.

- [123] G. Zacharakis, J. Ripoll, R. Weissleder and V. Ntziachristos, "Fluorescent Protein Tomography scanner for small animal imaging," *IEEE Transactions in Medical Imaging*, vol. 24, no. 7, pp. 878-885, July 2005.
- [124] C. Kak and M. Stanley, *Principles of Computerized Tomographic Imaging*, New York: IEEE, 1988.
- [125] P. Jaluria, M. Betenbaugh, K. Konstantopoulos and J. Shiloach, "Enhancement of cell proliferation in various mammalian cell lines by gene insertion of a cyclin-dependent kinase homolog," *BMC Biotechnology*, vol. 7, no. 71, 2007.
- [126] "Gray and white matter of the brain," ADAM, [Online]. Available: <http://www.umm.edu/imagepages/18117.htm>. [Accessed 14 February 2013].
- [127] S. Wahl, T. De Carli Foletto and G. Feldmann, "A Mathematical Model for the Estimation of Treatment Cost in Cancer Radiotherapy," in *Conference of Computer modeling (MCSUL)*, 2009.

Publications

The publications that have resulted from this thesis so far include:

Journal Articles

- [Pub. 1] **Roniotis, A.**, Marias, K., Sakkalis, V., Manikis, G. C., & Zervakis, M.E., (2012) Simulating radiotherapy effect in high grade glioma by using diffusive modeling and brain atlases, *Journal of Biomedicine and Biotechnology*, vol. 2012, Article ID 715812, 9 pages, doi:10.1155/2012/715812
- [Pub. 2] **Roniotis, A.**, Sakkalis, V., Karatzanis, I., Zervakis, M.E., & Marias, K. (2012). In-depth analysis and evaluation of diffusive glioma models, *IEEE Trans Inform. Tech. in Biomedicine 2012*, 16 (3), (299-307), doi: 10.1109/TITB.2012.2185704
- [Pub. 3] **Roniotis, A.**, Manikis, G., Sakkalis, V., Zervakis, M.E., Karatzanis, I., & Marias, K. (2012). High grade glioma diffusive modeling using statistical tissue information and diffusion tensors extracted from atlases, *IEEE Trans Inform. Tech. in Biomedicine 2012*, 16 (2), (255-263), doi: 10.1109/TITB.2011.2171190
- [Pub. 4] Marias, K., Dionysiou, D., Sakkalis, V., Graf, N., Bohle, R. M., Coveney, P. V., Wan, S., Folarin, A., Büchler, P., Reyes, M., Clapworthy, G., Liu, E., Sabczynski, J., Bily, T., **Roniotis A.**, Tsiknakis, M., Kolokotroni, E., Giatili, S., Veith, G., Messe, E., Stenzhorn, H., Yoo-Jin Kim, Zasada, S., Haidar, A. N., May, C., Bauer, S., Wang, T., Zhao, Y., Karasek, M., Grewer, R., Franz, A., & Stamatakis, G. (2011), Clinically driven design of multi-scale cancer models: the ContraCancrum project paradigm *Interface Focus*, 1 (3), pp. 450–461
- [Pub. 5] **Roniotis, A.**, Marias, K., Sakkalis, V., & Zervakis, M.E. (2010). Diffusive Modelling of Glioma Evolution: A review. *Journal of Biomedical Science and Engineering, Scientific Research*. 3 (5), (501-508)
- [Pub. 6] Skounakis, E., Farmaki, C., Sakkalis, V., **Roniotis, A.**, Banitsas, K., Graf, N., & Marias, K. (2010). DoctorEye: A clinically driven multifunctional platform, for accurate processing of tumors in medical images. *Intelligent signal and image processing in eHealth - The Open Medical Informatics Journal*. 4, (105-115)

Conference Proceedings

- [Pub. 7] Tzedakis, G., Tzamali, E., Sakkalis V., **Roniotis, A.**, Sakkalis, V., & Marias, K. (2012). Hybrid model for tumor spheroids with intratumoral oxygen supply heterogeneity, 5th International Advanced Research Workshop on In Silico Oncology and Cancer Investigation. October 22-23, Athens, Greece
- [Pub. 8] **Roniotis, A.**, Sakkalis, V., Tzamali, E., Tzedakis, G., Zervakis, M., & Marias, K. (2012). Solving the PIHNA model while accounting for radiotherapy 5th International Advanced Research Workshop on In Silico Oncology and Cancer Investigation. October 22-23, Athens, Greece
- [Pub. 9] **Roniotis, A.**, Marias, K., Sakkalis, V., & Stamatakis, G.S. (2010). Comparing Finite Element and Finite Difference Techniques as Applied to the Development

- of Diffusive Models of Glioblastoma Multiforme Growth. 32nd IEEE-EMBS, Engineering in Medicine and Biology Society (EMBC 2010). August 31-September 4, 2010, Buenos Aires, Argentina
- [Pub. 10] **Roniotis, A.**, Panourgias, K., Ekaterinaris, J., Marias, K., & Sakkalis, V. (2010). Approximating the diffusion – reaction equation for developing glioma models for the ContraCancrum Project: a showcase. 4th International Advanced Research Workshop on In Silico Oncology and Cancer Investigation. September 8-9, Athens, Greece
- [Pub. 11] Sakkalis, V., **Roniotis, A.**, Farmaki, C., Karatzanis, I., & Marias, K. (2010). Evaluation framework for the multilevel macroscopic models of solid tumor growth in the glioma case. 32nd IEEE-EMBS, Engineering in Medicine and Biology Society (EMBC 2010). August 31-September 4, 2010, Buenos Aires, Argentina
- [Pub. 12] **Roniotis, A.**, Sakkalis, V., Stamatakos, G.S., Zervakis, M.E., & Marias, K. (2010). Glioma diffusive modeling: Calculating diffusion coefficients from atlases with proportional tissue information. 4th International Advanced Research Workshop on In Silico Oncology and Cancer Investigation. September 8-9, Athens, Greece
- [Pub. 13] **Roniotis, A.**, Marias, K., Sakkalis, V., Skounakis, E., & Zervakis, M.E. (2010). Incorporating different proliferation rates in glioma modeling using vectorization operators. 4th International Advanced Research Workshop on In Silico Oncology and Cancer Investigation. September 8-9, Athens, Greece
- [Pub. 14] Stamatakos, G.S., Dionysiou, D.D., Giatili, S., Kolokotroni, E., Georgiadi, E., **Roniotis, A.**, Sakkalis, V., Coveney, P.V., Shunzhu, W., Steven, M., Zasada, St., Folarin, A., Büchler, P., Tibault, B., Bauer, St., Reyes, M., Bily, T., Bednar, V., Karasek, M., Graf, N., Bohle, R., Meese, E., Yoo-Jin, K., Stenzhorn, H., Clapworthy, G., & Liu, E. (2010). The ContraCancrum Oncosimulator: Integrating Biomechanisms Across Scales in the Clinical Context. 4th International Advanced Research Workshop on In Silico Oncology and Cancer Investigation. September 8-9, Athens, Greece
- [Pub. 15] Marias, K., Sakkalis, V., **Roniotis, A.**, Karatzanis, I., Stamatakos, G., Dionysiou, D., Giatili, S., Uzunoglou, N., Graf, N., Bohle, R., Meese, E., Stenzhorn, H., Kim, Y. J., Coveney, P., Zasada, S., Wan, S., Folarin, A., Büchler, P., Bardyn, T., Bauer, S., Reyes, M., Clapworthy, G., Liu, E., Bily, T., Bednar, V., Karasek, M., Franz, A., Grewer, R., & Sabczynski J. (2010). Clinically Oriented Translational Cancer Multilevel Modelling. 4th International Advanced Research Workshop on In Silico Oncology and Cancer Investigation. September 8-9, Athens, Greece
- [Pub. 16] **Roniotis, A.**, Marias, K., Sakkalis, V., Tsibidis, G.D., & Zervakis, M.E. (2009). A complete mathematical study of a 3D model of heterogeneous and anisotropic glioma evolution. In Proceedings of the Annual International Conference of the IEEE Engineering in Medicine and Biology Society. (pp. 2807-2810). United States
- [Pub. 17] Marias, K., Sakkalis, V., **Roniotis, A.**, Farmaki, C., Stamatakos, G.S., Dionysiou, D.D., Giatili, S., Uzunoglu, N.K., Graf, N., Bohle, R., Meese, E., Coveney, P.V.,

- Manos, S., Wan, S., Folarin, A., Nagl, S., Büchler, P., Bardyn, T., Reyes, M., Clapworthy, G., Mcfarlane, N., Liu, E., Bily, T., Balek, M., Karasek, M., Bednar, V., & Sabczynski, (2009). Clinically Oriented Translational Cancer Multilevel Modeling: The ContraCancrum Project. World Congress on Medical Physics and Biomedical Engineering. September 7-12, Munich, Germany. (pp. 2124-2127)
- [Pub. 18] **Roniotis, A.**, Marias, K., Sakkalis, V., Karatzanis, I., & Zervakis, M.E. (2009). The mathematical path to develop a heterogeneous, anisotropic and 3-dimensional glioma model using finite differences. Proceedings of the Information Technology Applications in Biomedicine (IEEE-ITAB 2009). November 5-7, Larnaca, Cyprus.
- [Pub. 19] Sakkalis, V., Marias, K., **Roniotis, A.**, & Skounakis, E. (2009). Translating cancer research into clinical practice: A framework for analyzing and modeling cancer from imaging data. 9th International Conference on Intelligent Systems Design and Applications, ISDA 2009. 30 November 2009 through 2 December 2009, Pisa. (pp. 347-350)

Other Articles and Reports

- [Pub. 20] **Roniotis, A.**, Marias, K., & Sakkalis, V. (2010). Modelling the Growth of a Malignant Brain Tumour. ERCIM News. 81, (21-22)